



**TOPOLOGY OPTIMIZATION OF AN  
AIRCRAFT WING**

THESIS

David L. Walker, Captain, USAF

AFIT-ENY-MS-15-J-044

**DEPARTMENT OF THE AIR FORCE  
AIR UNIVERSITY**

***AIR FORCE INSTITUTE OF TECHNOLOGY***

**Wright-Patterson Air Force Base, Ohio**

DISTRIBUTION STATEMENT A  
APPROVED FOR PUBLIC RELEASE; DISTRIBUTION UNLIMITED.

The views expressed in this document are those of the author and do not reflect the official policy or position of the United States Air Force, the United States Department of Defense or the United States Government. This material is declared a work of the U.S. Government and is not subject to copyright protection in the United States.



AFIT-ENY-MS-15-J-044

TOPOLOGY OPTIMIZATION OF AN AIRCRAFT WING

THESIS

Presented to the Faculty  
Department of Aeronautical Engineering  
Graduate School of Engineering and Management  
Air Force Institute of Technology  
Air University  
Air Education and Training Command  
in Partial Fulfillment of the Requirements for the  
Degree of Master of Science in Aeronautical Engineering

David L. Walker, B.S.M.E., M.A.S.

Captain, USAF

June 11, 2015

DISTRIBUTION STATEMENT A  
APPROVED FOR PUBLIC RELEASE; DISTRIBUTION UNLIMITED.

AFIT-ENY-MS-15-J-044

TOPOLOGY OPTIMIZATION OF AN AIRCRAFT WING

THESIS

David L. Walker, B.S.M.E., M.A.S.  
Captain, USAF

Committee Membership:

Maj. David Liu, PhD (Chairman)

Alan Jennings, PhD (Member)

Mark Reeder, PhD (Member)

## Abstract

A Topology Optimization (TO) was conducted on an aircraft wing in order to mathematically determine an ideal structural case for future aircraft. TO generally involves iteratively reducing individual elemental density until the desired mass or volume constraint is met. Optimizations were performed on a general aviation experimental aircraft wing subject to pressure loading simulating maximum rated structural conditions. Two different TO styles were approached: a global three-dimensional concept and a more traditional two-dimensional rib and spar optimization which more closely mimics the baseline model. The TO objective primarily consisted of minimizing compliance constrained to a desired volume fraction. All optimizations were compared against a baseline wing for von-Mises stress, displacement, and buckling. The objective of this research was to develop a design procedure maintaining the baseline structural integrity of the wing while reducing weight. As with many TO designs, Additive Manufacturing (AM) was studied as a means to produce the wing concerning both the feasibility of manufacture and as a logistical advantage compared to traditional means. Additionally, a fuel tank was integrated into the wing structure as a proof-of-concept for the potential benefits of AM. Finally, a 3D lattice structure was utilized as a conceptual method for improving current design methodology. A 2D TO of the ribs in the wing reduced each rib mass by 18.5 percent, or a reduction of 3.7 percent of the total wing mass. The most significant weight savings was seen in a two-dimensional topology and sizing optimization of the wing integrated with the fuel tank, spars, and skin. This resulted in a total wing mass reduction of 10.8 percent. Concurrently, the peak stress remained approximately the same while the total displacement was reduced by over 50 percent.

## Acknowledgements

I would like to thank Mr. Dennis Lindell at the Joint Aircraft Survivability Program Office for sponsoring this research. I would also like to thank my research adviser, Major David Liu, for his guidance throughout this effort. I would also like to thank my committee members, Dr. Alan Jennings and Dr. Mark Reeder, for their support as well. Most importantly, I would like to thank my wife for allowing me the flexibility to perform this research while she cared for our growing family virtually on her own. She is an excellent mother to both of our children. Without her support, much of this research would not have been possible.

David L. Walker

# Table of Contents

	Page
Abstract .....	iv
Acknowledgements .....	v
List of Figures .....	viii
List of Tables .....	xiii
List of Acronyms .....	xv
I. Introduction .....	1
1.1 Background .....	1
1.2 Motivation .....	3
1.3 Research Scope .....	4
1.4 Research Objectives .....	5
1.5 Limitations and Assumptions .....	6
II. Literature Review .....	7
2.1 Introduction .....	7
2.2 Topology Optimization .....	7
2.3 Altair Optistruct .....	13
2.4 Loading Conditions .....	17
2.5 Virtual Wind Tunnel .....	19
2.6 Previous Research .....	20
2.7 Related Optimization Research .....	23
2.8 Additive Manufacturing .....	25
III. Experimental Setup .....	28
3.1 Introduction .....	28
3.2 Software Analysis .....	28
3.3 Baseline Aircraft .....	30
3.4 Initial Design Loading Conditions .....	32
3.5 Initial Designs .....	34
3.6 Advanced Loading Conditions .....	36
3.7 Baseline Analysis .....	41
3.7.1 Setup .....	41
3.7.2 Results .....	43
3.7.3 Analysis for Baseline Wing with Tank .....	48
3.8 Local Optimizatation .....	52
3.9 Global Design .....	54

	Page
3.10 Component Integration .....	55
IV. Results and Analysis .....	57
4.1 Initial Designs .....	57
4.2 Local Optimization .....	59
4.2.1 Rib-Only Optimization .....	60
4.2.2 Interpreted Design vs. TO Displacement and Stress .....	74
4.2.3 Spar and Skin Optimization .....	75
4.2.4 Buckling Comparative Analysis .....	81
4.3 Global Optimization .....	87
4.4 Component Integration .....	92
4.4.1 Local Tank Integration .....	93
4.4.2 Global Tank Integration .....	105
4.5 Lattice Structures .....	107
4.6 Summary .....	111
V. Conclusions and Recommendations .....	116
5.1 Review of Research Objectives .....	116
5.2 Additive Manufacturing Design .....	117
5.3 Recommendations for Improvement .....	118
5.4 Future Work .....	119
Appendix A. Baseline Wing Schematic .....	121
Appendix B. Summary of Optimized Designs .....	124
Bibliography .....	126

## List of Figures

Figure		Page
1	Simple Cantilever Beam Solution Using Topology Optimization . . . . .	2
2	First Three Buckling Modes on Simple Column . . . . .	12
3	Hypermesh Interface for TO Problem Setup of Multiple Point Loading on Beam . . . . .	13
4	Hyperview Interface for TO Problem of Multiple Point Loading on Beam . . . . .	17
5	Model in Virtual Wind Tunnel CFD Analysis Interface . . . . .	20
6	Objet Eden500V 3D Printer . . . . .	27
7	Objet Eden500V Build Tray . . . . .	27
8	Cantilever Beam with Constraints and Point Force Problem Setup for TO . . . . .	29
9	99 Line Matlab TO Results vs. Optistruct TO Results for Similar Loading Conditions . . . . .	29
10	Van's RV-4 Experimental Aircraft Schematic . . . . .	30
11	NACA 23015 Airfoil $C_p$ Distribution for Zero $\alpha$ . . . . .	33
12	Initial 2D Design Space Problem Setup of Optistruct TO . . . . .	34
13	Initial 3D Design Space Problem Setup of Optistruct TO . . . . .	34
14	Force Load Conditions for Initial Optistruct TO Analysis . . . . .	35
15	Structural Constraints for Initial Optistruct TO Analysis . . . . .	35
16	Optistruct TO Result for 2D Design Space with Given Loading Conditions and Constraints . . . . .	36
17	NACA 23015 Airfoil $c_l$ vs $\alpha$ Chart . . . . .	37
18	Virtual Wind Tunnel Wing Pressure Load Model for CFD Analysis . . . . .	39

Figure		Page
19	VWT Model Pressure Contours for Each RV-4 Manuever Flight Profile .....	39
20	Pressure Load Conditions for +6G Flight Profile .....	40
21	Structural Constraints for All Advanced Loading Conditions .....	41
22	Baseline RV-4 Wing for Initital Performance Analysis .....	42
23	Wing Deflection Contours for Each Flight Profile of Baseline Wing .....	44
24	Wing Stress Contours for Each Flight Profile of Baseline Wing Skin .....	45
25	Wing Stress Contours for Each Flight Profile of Baseline Wing Internal Structure .....	46
26	Buckling Analysis for +6g, Rolling Right for Baseline Wing .....	47
27	Baseline RV-4 Wing Tank .....	48
28	Wing Deflection Contours for Each Flight Profile of Baseline Wing with Fuel Tank .....	50
29	Wing Stress Contours for Each Flight Profile of Baseline Wing with Fuel Tank .....	51
30	Buckling Analysis for +6g, Rolling Right for Baseline Wing with Fuel Tank .....	52
31	Local TO 2D Rib Problem Setup .....	53
32	3D Global Optimization Problem Setup .....	54
33	3D Global Optimization Problem With Tip Ribs and Rear Spar .....	55
34	Element Density for Initial Design Wing Segment TO for VF of 0.15 .....	57
35	Element Density for Section Views of TO Initial Design for VF of 0.15 .....	58



Figure		Page
36	Element Density for TO Interpreted Results of Initial Design with VF of 0.15 and Threshold of 0.40 .....	59
37	Initial Design Manufactured Part with VF of 0.15 and Threshold of 0.40 Using a Photopolymer AM Technique .....	59
38	Element Density for 2D Rib Optimization Without Pattern Repetition .....	62
39	Wing Deflection Contours for Each Flight Profile of Rib Optimized Wing without Pattern Repetition .....	63
40	Wing Stress Contours for Each Flight Profile of Rib Optimized Wing without Pattern Repetition .....	64
41	Element Density for 2D Rib Optimization With Pattern Repetition .....	66
42	Wing Deflection Contours for Each Flight Profile of Rib Optimized Wing with Pattern Repetition .....	67
43	Wing Stress Contours for Each Flight Profile of Rib Optimized Wing with Pattern Repetition .....	68
44	TO Design Rib from Local Optimization with Pattern Repetition .....	70
45	Shape Comparison Between Baseline Rib and TO Rib .....	72
46	Wing Deflection Contours for Each Flight Profile of Wing Integrated with TO Rib .....	72
47	Wing Stress Contours for Each Flight Profile of Wing Integrated with TO Rib .....	73
48	2D Spar and Skin Free Sizing Optimization Problem Setup .....	76
49	Local TO Results for Spar and Skin Free-Sizing Optimization of Local Wing Design .....	78
50	Wing Deflection Contours for Each Flight Profile of Wing with TO Ribs and Sizing Optimized Spars and Skin .....	78
51	Wing Stress Contours for Each Flight Profile of Wing with TO Ribs and Sizing Optimized Spars and Skin .....	79

Figure		Page
52	Buckling Analysis for +6g, Rolling Right Maneuver for Rib Optimized Wing without Pattern Repetition.....	81
53	Buckling Analysis for +6g, Rolling Right Maneuver for Rib Optimized Wing with Pattern Repetition .....	83
54	Buckling Analysis for +6g, Rolling Right Maneuver for Wing Integrated with TO Optimized Rib .....	84
55	Buckling Analysis for +6G, Rolling Right Maneuver for Wing with TO Ribs and Sizing Optimized Spars and Skin.....	85
56	Density Fraction Contour of Global Wing TO .....	88
57	Various View Orientations for Global TO with Density Fraction Threshold of 0.20 .....	89
58	Density Fraction Contour of Global Wing TO with Tip Ribs and Rear Spar .....	90
59	Various View Orientations for Global TO with Density Fraction Threshold of 0.20 .....	91
60	Fuel Tank Design for Local TO .....	93
61	Global Stress Contour Interpretation to Local TO Fuel Tank Design .....	94
62	Optistruct Local TO Tank Integration Model Problem Setup for Rib Design .....	94
63	Results for Fuel Tank TO with Rib Only Design Space .....	95
64	Local TO Results for Spar and Skin Free-Sizing Optimization of Local Wing Design with Integrated Tank .....	96
65	High Stress Region at Joint Between Spar and Fuel Tank in Integrated Fuel Tank Local TO .....	97
66	Free Sizing Optimization Wing Deflection Contours for Each Flight Profile of Wing Integrated with Fuel Tank.....	99
67	Free Sizing Optimization Wing Stress Contours for Each Flight Profile of Wing Integrated with Fuel Tank.....	100

Figure		Page
68	Plastic 3D Printed Model of Local TO Integrated With Fuel Tank with Top Skin Removed . . . . .	103
69	Aluminum AM Model of Local TO Integrated With Fuel Tank with Top Skin Removed . . . . .	104
70	Fuel Tank Design for Global TO . . . . .	105
71	Global Design with Integrated Fuel Tank Process to Determine Tip Rib Design and Generate TO . . . . .	106
72	Global Design with Integrated Fuel Tank TO Results with 0.20 Density Fraction Threshold . . . . .	107
73	Optistruct Process for Lattice Optimization of 3D Design Space . . . . .	108
74	Lattice Structure for Global Design Space with Integrated Fuel Tank at VF of 0.05 . . . . .	109
75	Mass with Stress and Displacement vs Design for TO Wings without Integrated Fuel Tank . . . . .	113
76	Mass with Stress and Displacement vs Design for TO Wings with Integrated Fuel Tank . . . . .	114
77	Van's RV-4 Wing Schematic . . . . .	121
78	Van's RV-4 Rib Schematic . . . . .	122
79	Van's RV-4 Tank Schematic . . . . .	123
80	Baseline Analysis Models . . . . .	124
81	Various TO Design Results . . . . .	125

## List of Tables

Table		Page
1	RV-4 Experimental Aircraft Wing Properties and Specifications .....	30
2	2024-T4 Aluminum Material Properties .....	32
3	Wing Angle of Attack for Given Load Factor of NACA 23015 Airfoil at RV-4 Manuever Speed .....	38
4	Baseline Wing Component Material Thickness for 2024-T4 Aluminum Sheet Metal .....	42
5	Baseline Wing Component Surface Area, Volume, and Mass .....	43
6	Displacement and Stress of Baseline Wing .....	46
7	Buckling Load Factor of Baseline Wing .....	47
8	Baseline Wing with Fuel Tank Component Surface Area, Volume and Mass .....	49
9	Displacement and Stress of Baseline Wing with Fuel Tank .....	51
10	Buckling Load Factor of Baseline Wing with Fuel Tank .....	52
11	Rib TO without Pattern Repetition Component Surface Area, Volume, and Mass Compared to Baseline Wing .....	62
12	Displacement and Stress of Rib Optimized Wing without Pattern Repetition Compared to Baseline Wing .....	65
13	Rib TO with Pattern Repetition Component Surface Area, Volume, and Mass Compared to Baseline Wing .....	66
14	Displacement and Stress of Rib Optimized Wing with Pattern Repetition Compared to Baseline Wing .....	69
15	Redesigned TO Rib Surface Area, Volume, and Mass Compared to Baseline Wing .....	71
16	Displacement and Stress of Wing with Integrated TO Rib Compared to Baseline Wing .....	74

Table		Page
17	Displacement and Stress Comparison from TO Output of Rib Optimized Wing without Pattern Repetition with Percent Change Relative to the Post-Processed Results .....	75
18	Displacement and Stress of Wing with TO Ribs and Sizing Optimized Spars and Skin Compared to the Baseline Wing .....	80
19	Buckling Load Factor of Rib Optimized Wing without Pattern Repetition Compared to Baseline Wing .....	82
20	Buckling Load Factor of Rib Optimized Wing without Pattern Repetition Compared to Baseline Wing .....	83
21	Buckling Load Factor of Wing Integrated with TO Rib Compared to Baseline Wing .....	84
22	Buckling Load Factor of Wing with TO Ribs and Sizing Optimized Spars and Skin Compared to Baseline Wing .....	85
23	Rib, Spar, and Skin TO with Integrated Fuel Tank Component Surface Area, Volume, and Mass Compared to Baseline Wing .....	97
24	Displacement and Stress of Free Sizing Optimized Wing with Integrated Fuel Tank Compared to Baseline Wing .....	101
25	Buckling Load Factor of Integrated Fuel Tank Wing with TO Ribs and Sizing Optimized Spars and Skin Compared to Baseline Wing .....	102
26	Displacement and Stress of Lattice Structure for Global Design Space with Integrated Fuel Tank Compared to Baseline Wing with Fuel Tank Compared to Baseline Wing .....	110
27	Buckling Load Factor of Lattice Structure for Global Design Space with Integrated Fuel Tank .....	110
28	Performance Summary for all TO Results .....	112

## List of Acronyms

**AM** Additive Manufacturing

**BLF** Buckling Load Factor

**CAD** Computer Aided Design

**CFD** Computational Fluid Dynamics

**CRM** Common Research Model

**DMLS** Direct Metal Laser Sintering

**DOF** Degrees of Freedom

**FEA** Finite Element Analysis

**GLS** Galerkin/Least-Squares

**KIAS** Knots-Indicated Air Speed

**NACA** National Advisory Committee for Aeronautics

**POH** Pilot Operating Handbook

**SIMP** Simple Isotropic Material with Penalization

**STL** STereoLithography

**SLS** Selective Laser Sintering

**TO** Topology Optimization

**UAV** Unmanned Aerial Vehicle

**UDF** User-Defined Function

**VF** Volume Fraction

**VWT** Virtual Wind Tunnel

# TOPOLOGY OPTIMIZATION OF AN AIRCRAFT WING

## I. Introduction

### 1.1 Background

Current aircraft wing design, which relies on internal struts and spars for aerodynamic load bearing, is limited primarily by traditional manufacturing techniques. If manufacturing constraints are removed, the design focus shifts towards providing an improved distribution of loads throughout the structure, subsequently eliminating unnecessary material. To design an optimized component, an increasingly more common method in structural design is the implementation of Topology Optimization (TO). TO is considered a mathematical approach to finding an optimized material distribution over a given design space [1]. In other words, only material vital to the support structure is used. The process entails iteratively determining load bearing elements in a discretized domain within the structure and eliminating nonessential material [2]. For the purposes of this research, the overall objective is to reduce mass, or subsequently material volume, while at least retaining structural stiffness and stress levels for all applied loads.

An excellent example of TO is an open-source MATLAB code which was developed by Sigmund. The code is a relatively simple 99-line algorithm and is publically available to any MATLAB user. The code performs TO in a two-dimensional user-defined rectangular design space. Loads and constraints are set and the code iteratively produces an optimal image by removing material until a user-defined Volume Fraction (VF) is met [2]. An example of a simple cantilever beam solution with a



single load constrained on a wall is shown in Figure 1. As seen, the design space is in pink and with the vertical constraints along the left-hand side and a singular horizontal point constraint at the lower right-hand corner. The result is the relatively intuitive truss-like structure. As problems get more complex, the results become more revealing.

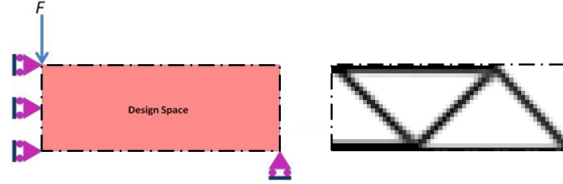


**Figure 1. Simple Cantilever Beam Design Space and Solution Using Topology Optimization Solver[2]**

TO is not a new theory and is frequently used within the Aerospace Industry. Airbus Aeronautical Company applied both Altair Inc. and in-house developed software in order to optimize the design of individual spars and wing-box structures for large commercial aircraft. They considered a hybrid global/local approach in a semi two-dimensional manner to modify the existing spars and ribs. A considerable material savings was noticed in their updated designs. However, fatigue testing and machine trials were ongoing at the time of the publication, so no exact weight savings are published [3]. Another similar approach was conducted by Locatelli, Mulani, and Kapania by using curvilinear spars and ribs as opposed to a traditional parallel and perpendicular internal structure. Even though this is not TO, the methodology is a unique way to improve wing design. Overall, a savings of 19 percent when performing the analysis on a generic fighter wing was estimated compared to the baseline [4].

Currently, examples of TO used in the aerospace industry are generally limited to two-dimensional designs and the results are used as guidance towards a more reasonable design through interpretation. Three-dimensional designs created by TO are often very complex and historically not feasible to manufacture through traditional

means. However, advances in Additive Manufacturing (AM) have made this concept a seemingly more viable approach. AM consists of building a product by applying thin layers of material to generate a shape. Therefore, an optimized design produced through AM techniques is less limited in shape compared to traditional manufacturing constraints, allowing for a design which truly enhances the performance of the component with minimal regard for manufacturing constraints. For the purpose of this research, Selective Laser Sintering (SLS) was examined as a potential means to manufacture topology optimized designs. Laser sintering utilizes a substrate in which a powder material is welded on in very thin layers. Even though the technology is not fully matured, this research will investigate future capabilities and potential benefits of using SLS. Polymer AM models were also manufactured for conceptual purposes.

## **1.2 Motivation**

For this research, the overall internal structure of a wing was examined. An effective topology optimization provides the obvious advantage of reducing weight in an aircraft by eliminating unnecessary material. An optimized approach has the potential to streamline the design process by allowing a computer algorithm to develop the internal structure while allowing the engineer to concentrate almost solely on the aerodynamic properties. In addition, since current designs are very limited by manufacturing, TO designs manufactured using AM can veer closer to an optimal shape. The wing is then lighter and at least as structurally sound as current aircraft designs, further enhancing aircraft performance. Similarly, a reduction in weight is regarded as a means to increase a given payload on an aircraft.

In respect to the Department of Defense, an optimized wing manufactured through AM has the potential to significantly enhance the logistical timeline to repair equipment in the field. The AM of aircraft components has potentially created the capa-

bility to produce structures without the infrastructure required to ship and store a multitude of parts. Rather, a handful of machines, along with the respective stock material, can produce whichever component is needed in a relatively short period of time. In this scenario, Computer Aided Design (CAD) files are modified and transmitted virtually anywhere in the world in order to produce the most up to date part available. Doing so has the potential to significantly streamline the process of aircraft maintenance and repair. However, it is also important to consider the limitations of SLS, such as size and geometrical constraints.

Finally, since AM reduces many of the manufacturing constraints considered during wing development, it is possible to integrate individual components into a single part. Components, such as fuel tanks or electronics are traditionally not used as load bearing parts. However, complete application into a singular design can change this paradigm. Doing so has the potential to reduce both weight and complexity.

### **1.3 Research Scope**

The purpose of this research is to develop a Topology Optimized wing and manufacture it through AM techniques. The research is focused on processes and determining the far-term feasibility of generating such a wing, regardless of aircraft type. Therefore, a single aircraft was selected as a baseline for gauging effectiveness. Previous research has utilized TO as means for enhancing current designs, and that ideology is considered in this context as well. Loading conditions were applied for a series of the most severe flight conditions in which failure may occur. A complete structural analysis, which is often associated with aircraft development, is beyond the scope of this research. Therefore, only the wing was optimized and analyzed under the specified flight profiles.

## 1.4 Research Objectives

For this research, the overall objective was to optimize the entire structure of a wing in a manner which is then manufactured through AM. To provide an assessment of the effectiveness of the design, several supporting objectives were set:

1. Determine pressure loading on the wing for critical phases of flight and apply the values towards the analysis and optimization processes.
2. Perform a computational analysis on the baseline aircraft wing to determine localized stress and displacement values.
3. Generate a computational analysis on the optimized designs used for comparative purposes.
4. Integrate a traditionally independent component into the optimized wing as a dual-purpose structure.
5. Interpret full-scale design to meet AM constraints and produce the model.

Initial wing designs and baseline products were built in Solidworks prior to the optimization process. Loading on the wing was applied for multiple aerodynamic profiles generating the greatest stresses on the wing. This was done by finding loads on the wing model in a virtual wind tunnel. Altair Hypermesh software with the Optistruct toolkit was used exclusively for the optimization process. The baseline wing is from a home-built, experimental aircraft. This original design was used for comparative purposes. The Optistruct software output topology optimized designs based on bounding conditions. However, engineering judgment was extensively used to ensure a realistic and printable part which met all loading requirements. The final output designs from Optistruct were interpolated to a feasible design, as well as analyzed with Finite Element Analysis (FEA), prior to manufacturing.

The final output objective was to build a three-dimensional printed optimized wing which was adequately analyzed through FEA for the given loading conditions. Even though manufacture of a full-size aircraft wing is not yet possible with current AM process technology, this provides a step towards proof of concept. A feasible wing design has stress and deflection levels similar to or better than the baseline wing design. In addition to optimizing a baseline wing to the given loading conditions, it was also desired to integrate a fuel tank of equal size to the baseline into an optimized additive manufactured wing.

## **1.5 Limitations and Assumptions**

This research is focused on local and global optimization of a single aircraft wing. Optimization constraints were limited to material stress and displacement, with some buckling analysis. In a complete study, flutter and fatigue considerations are required to ensure compliance with operating conditions. Complete wind-tunnel and/or flight testing are also generally used for final verification. However, timing and resource limitation limited this research in those realms. Therefore, optimizations were constrained by VF with objectives of minimizing compliance. FEA was used to determine stress and displacement conditions of the wing. The material properties were taken entirely from aluminum alloy 2024-T4 to correspond with the baseline aircraft material [5].

## II. Literature Review

### 2.1 Introduction

Topology optimization in the aerospace industry has remained a topic of great interest and is discussed in several scholarly articles. Several aircraft manufacturers are at the forefront of technology advancements as a means of developing a more efficient aircraft design. Several other academic and commercial institutions also have a vested interest in enhancing structural designs within their respective industries. Additionally, the advances in AM have created a greater relevance toward TO feasibility, even though the technology is not yet mature. The following material is used as a baseline for the methods of research discussed in this paper in the hopes to further grow the knowledge base for this subject matter.

### 2.2 Topology Optimization

O. Sigmund has published several articles in regards to topology optimization. Notably, “A 99 line topology optimization code written in Matlab” discusses several core attributes regarding TO. The power-law approach, or Simple Isotropic Material with Penalization (SIMP) is a commonly used practice. With this process, all material properties of a model are considered constant whereas density is variable within a discretized design space. The material properties of each element is the density raised to some power multiplied by the properties of the fully dense material [2]. Also known as the ‘artificial power law’ method, it is thought of as defining the density factor of the material,  $\rho$ , at each point within the domain of the solution. The density factor varies consistently between 0 and 1, with 0 being no material and 1 characterizing the true material. Doing so gives a physical interpretation of the design in terms of sub-optimal, isotropic micro-structures [6]. The applied penalization power on the

density factor steers low density values towards zero while having less effect on high density elements [2]. This process was proved by Bendsoe and Sigmund as permissible as long as the penalization power is  $\geq 3$  for a Poisson's ratio of  $\frac{1}{3}$  [7]. Since variable density is not physically possible for design interpretation, a density threshold is often selected as a barrier between material presence and a void. Once again, the threshold value is between 0 and 1, with 0 considering material of all density values and 1 considering material only fully dense [2]. Any value above the selected threshold value is considered material and any density that is less is a void. This approach is effective, as long as additional FEA testing is accomplished to verify performance [1]

Mathematically the power-law for a minimum compliance (maximize stiffness) problem approach is shown in Equation 1.

$$\begin{aligned}
min : \quad & c(x) = U^T K U = \sum x_e^p U_e^T k_0 u_e \\
Subject \ to : \quad & \frac{V(x)}{V_0} = f \\
& : \quad K U = F \\
& : \quad 0 < x_{min} \leq x \leq 1
\end{aligned} \tag{1}$$

where  $\mathbf{x}$  is the design variable vector,  $\mathbf{U}$  is the global displacement vector,  $\mathbf{F}$  is the force vector, and  $\mathbf{K}$  is the global stiffness matrix. The displacement vector is  $\mathbf{u}_e$  and  $\mathbf{k}_e$  is the stiffness matrix. The minimum relative density vector and the total number of elements are  $\mathbf{x}_{min}$  and  $\mathbf{N}$ , respectively. Finally  $\mathbf{f}$  is the volume fraction [2].

Even though SIMP is the most common methodology, there are other material interpolation schemes which can be used. However, SIMP is the only method used in this research. In particular, the Voigt and Hashin-Shtikman methods provide a means to generate a physical interpretation. The Voigt bound considers a variable thickness sheet problem, allowing for a linear interpolation of stiffness throughout the sheet [8]. Mathematically, Voigt bound for purely planar and three dimensional

problems is described in Equation 2.

$$C_{ijkl} = \rho C_{ijkl}^0, \quad 0 \leq \rho(x) \leq 1, \quad Vol = \int_{\Omega} \rho(x) d\Omega \quad (2)$$

In this case, the maximum sheet thickness is set to 1 where  $\Omega$  is the volume space for three dimensions and  $C_{ijkl}$  is the stress tensor for the material. The thickness varies throughout the optimal design, where 0 thickness areas are potentially present. Similar to other methods, some penalization of gray areas is also required [8].

The Hashin-Shtrikman bound utilizes similar methodology of penalizing intermediate densities similar to SIMP which uses a penalty to steer density. In this case, Young's modulus and Poisson's ratio are a function of density and the respective baseline condition. Mathematically, this is seen in Equation 3, where  $E$  is Young's modulus and  $\nu$  is Poisson's ratio [8].

$$\begin{aligned} E(\rho) &= \frac{\rho E_0}{3 - 2\rho} \\ \nu(\rho) &= \frac{1 - \rho(1 - \nu^0)}{3 - 2\rho} \end{aligned} \quad (3)$$

Along with a penalization technique, filtering is used as a means to reduce "checkering" in a TO design. Checkering is a result of significant density variances in adjacent elements which create a checkerboard pattern. This provides an unfeasible final output. Filtering techniques result in a blending of density on elements in order to smooth density transition. Filtering is commonly applied along with SIMP in topology optimization to eliminate checkering and provide a more clear solution [1]. Bourdin discusses filtering techniques which apply additional constraints on the optimization, such as permissible density levels. Specifically, he discusses three separate techniques for doing so. Each involves replacing the elastic-property density dependence with a filtered variation. By doing so, rapid variations of properties do



not occur. Using the Lipschitz bounded domain, the filtering characteristic involves replacing each density with a weighted average of its values [6].

Numerical implementation of the filtered minimum compliance densing problem is accomplished using three different methods. The first method is shown in Figure 4, where  $\Omega$  is the design space,  $e$  is the center of the element, and  $V(e)$  is the set of elements. This particular method has a smoothing effect near the domain boundary since  $\rho$  cannot equal 1 at a boundary [6].

$$(f * \Omega\rho)_e := \sum_{i \in V(e)} (\rho_i \int_i F(x - c_e) dx) \quad (4)$$

The next method, Equation 5, renormalizes Equation 4. This somewhat forces the density to take high values near the edge [6].

$$(f * \Omega\rho)_e := \frac{\sum_{i \in V(e)} (\rho_i \int_i F(x - c_e) dx)}{\sum_{i \in V(e)} (\int_i F(x - c_e) dx)} \quad (5)$$

Finally, the preferred method by Bourdin is to use translations and symmetries to extend the density to the edge of the domain space, as shown in Equation 6 [6].

$$(f * \Omega\rho)_e := \sum_{i \in V(e)} (\int_i F(x - c_e) dx) \quad (6)$$

Using this filtering method, a simple example was accomplished with a center load on a symmetrical beam. The same optimization was completed; once with no filter, and once with a filter for a multitude of element sizes. At low resolution, there was minimal noticeable benefit using the filter. However, once the resolution became finer than the filter support, the benefits of the effective density are apparent. The results concluded a refined density without the “checkerboard” appearance of an unfiltered result was possible, and is the primary benefit of using the technique [6].

Topology optimization responses are objectives or constraint on the final design

[9]. For this research, responses were limited to compliance (inverse of stiffness), VF, mass fraction, stress, and buckling. Volume and mass fraction are simply the fraction of volume or mass to the respective design space. This is often used as a optimization constraint as an upper-limit of how much material is desired. Likewise, a global stress constraint limits the maximum stress on an individual element [9].

In general, TO methodology is a minimum compliance problem [1]. The overall objective to minimize compliance is used frequently in TO due to the simplicity of establishing the problem [2]. In this research, all optimization problems were generated with a minimum compliance objective, which will be discussed in Chapter 3. Minimizing compliance is a global stiffness problem in which the stiffness matrix,  $K$ , is a function of a variable stiffness tensor throughout the domain [1]. Compliance,  $C$ , is shown in Equation 7 if  $u$  and  $f$  are displacement and load vectors, respectively, whereas  $K$  is the global stiffness matrix [9, 1].

$$C = \frac{1}{2}U^T f, \text{ where } KU = f \quad (7)$$

Buckling is the final consideration of the optimization problems for this research. Buckling is of a concern to aircraft design since the buckling stress is often near the yield stress of the material [10]. Buckling occurs suddenly when the buckling stress level is reached and does not necessarily return to the original shape when the force is relaxed [11]. The Buckling Load Factor (BLF) is the ratio of the applied load,  $L$ , over the load in which the structure would buckle,  $L_b$ . Mathematically, this is seen in Equation 8 [10].

$$BLF = \frac{L}{L_b} \quad (8)$$

The optimization problem for buckling is to minimize the critical failure load,

$P_{crit}$  [1]. Buckling does not occur with a truly compressive load condition, rather only with an arbitrary lateral load [10]. It is also important to note buckling will occur suddenly at the discrete load of  $P_{crit}$ , which is a function of material stiffness. If considering a critical load on a pin-ended column,  $P_{crit}$  is describe in Equation 9 if  $n$  is the buckling mode,  $E$  is the modulus of elasticity,  $I$  is the moment of inertia, and  $l$  is the length of the member [11].

$$P_{crit} = \frac{n^2 \pi^2 EI}{l^2} \quad (9)$$

The first three buckling modes are seen in Figure 2. From Equation 9, the column will buckle at discrete values of axial load and  $P_{crit}$  is dependent on the mode. These discrete values are the eigenvalues of the problem [10]. Note that  $P_{crit}$  quickly increases relative to the square of  $n$ , and therefore only lower buckling modes are considered [1].

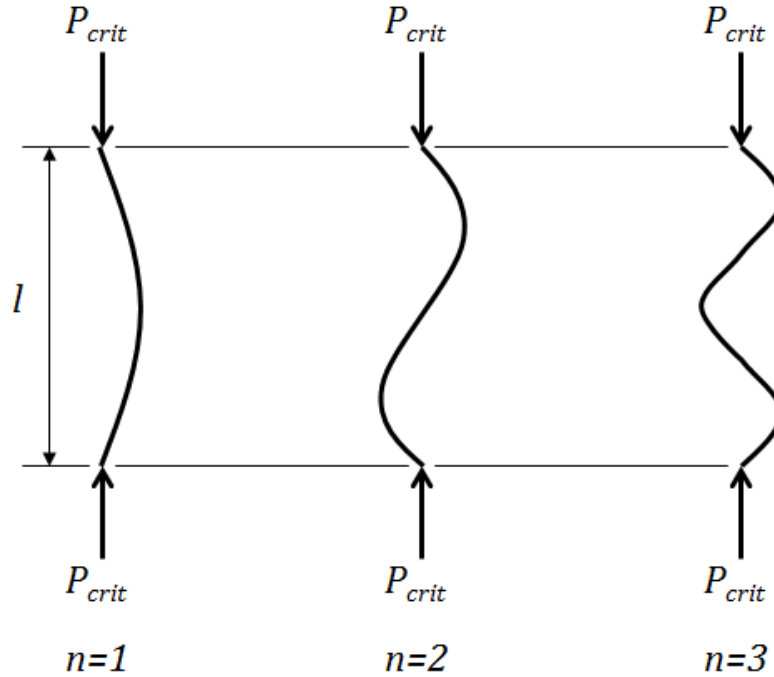
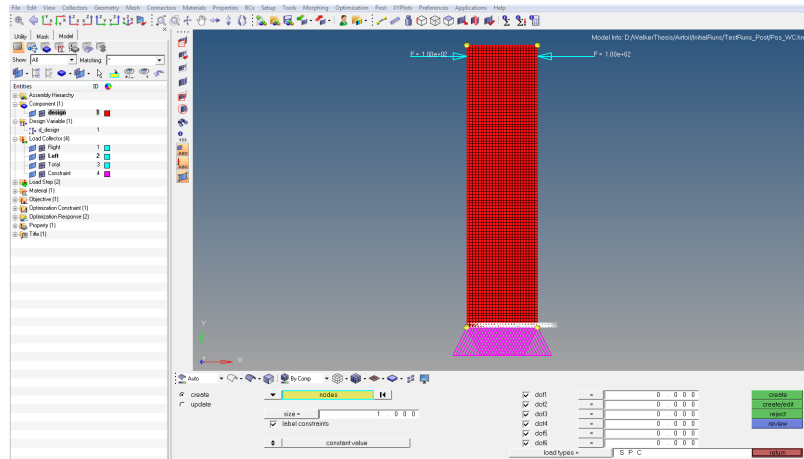


Figure 2. First Three Buckling Modes on Simple Column

## 2.3 Altair Optistruct

The software used for this research analysis was entirely developed by Altair Engineering of Troy, MI. Altair was founded in the early 1980's and is one of the few companies focusing on topology optimization [12]. The Hyperworks software suite of programs used included Hypermesh, Optistruct, and Virtual Wind Tunnel. Primarily, Optistruct was used as the optimization software. Optistruct has capabilities to perform various optimization processes with a multitude of response conditions. FEA analysis is also easily accomplished on both an initial and optimized design using Optistruct [9].

Hypermesh is the pre- and post-processing tool for optimized designs. The primary purpose of Hypermesh is the capability to setup a model for optimization. Computer Aided Design (CAD) models are appropriately meshed in both two and three dimensions. Loading and constraint conditions are also applied in Hypermesh in preparation for Optistruct analysis, as well setting up response conditions [13]. Figure 3 is an example of a simple model setup in the Hypermesh interface. In this case, the model is a 2D rectangular design with both constraints and forces applied.



**Figure 3. Hypermesh Interface for TO Problem Setup of Multiple Point Loading on Beam**

Topology optimized Optistruct models are analyzed as either 2D shell or 3D solid elements, or a combination of both. A specified design space shape is discretized into elements in which properties are applied to individual components. The TO software iteratively evaluates the optimized solution for given constraints and objectives by determining the material properties of each element. Many optimization constraints and objectives are available within the software; however, compliance, volume/mass fraction, buckling, and displacement were the focus of this research. Specifically, the VF constraint with a minimizing function of compliance was primarily used. In addition to these responses, the manufacturing constraint of minimum and maximum member size is optionally applied. The user also has the option to set a upper stress limit. However, with variable density TO, very low density elements can experience high stress levels and can cause poor results [9].

Optistruct is able to constrain responses as desired for the optimization process. If desired, both mass and VF limitations are set as the respective mass or volume over the total design space. Therefore, these values range from 0 to 1. Displacement is constrained as either a local point or total global displacement. A buckling analysis is accomplished with set modes and BLF ranges. A BLF limit, usually a lower-limit of one, is usually set as constraints for a TO [9].

Considering the objective function,  $f(\mathbf{x})$ , and constraint function,  $g(\mathbf{x})$ ,  $\mathbf{x}$  design variable, and upper and lower limitation  $U$  and  $L$ , respectively, Optistruct solves the optimization problem seen in Equation 10 [9].

$$\begin{aligned}
\min f(x) &= f(x_1, x_2, \dots, x_n) \\
\text{Subject to : } g_j(x) &\leq 0 \quad j = 1, \dots, m \\
x_i^L &\leq K_i \leq x_i^U \quad i = 1, \dots, n
\end{aligned} \tag{10}$$

In a similar manner to Sigmund’s “99 lines” research, Optistruct utilizes the SIMP,

or power-law, method of variable density. Each element is assigned a density value between 0 and 1, where 0 represents a void and 1 represents a fully dense material. All other values between represent a fictitious material in which stiffness is linearly dependent on the respective density factor. Along with designated material properties, the density determines the structural characteristics of the given element. The power law representation of elastic properties as the penalization technique is used for both 2D and 3D elements. In general, the penalization power,  $p$ , is a value between 2.0 and 4.0. However, the default value is 1.0 for 2D shell elements and 2.0 for 3D solid elements. When a minimum member size is applied, the default penalty is increased to 3.0 after the first iteration in order to achieve a distinct solution. This is seen mathematically in Equation 11 where  $\bar{K}$  is the penalized stiffness and  $K$  is the real stiffness matrix of a given element. The density factor and penalization are represented by  $\rho$  and  $p$ , respectively [9].

$$\bar{K}(\rho) = \rho^p K \quad (11)$$

Both force and pressure loading are applied to models within Optistruct. Forces are applied to nodes connecting the mesh and are set as individual vectors. Pressure loading is applied to an element. A force vector is applied to the element as a function of the element surface area. When pressure is applied, it is assigned as either a singular pressure load for analysis or as a factor in a multiple loading condition. In the latter case, conditions are respectively weighted as desired. The software analyses weighted load conditions mathematically in Equation 12 [9].

$$\vec{P} = S \sum_i S_i \vec{P}_i \quad (12)$$

where  $\vec{P}$  is the applied load to an element,  $S$  is the global weighting,  $S_i$  is the indi-

vidual weight factor, and  $L_i$  is the respective partial load. Since loads applied in this situation are summed, this does not apply to multiple conditions optimized independently, but rather as a total loading condition; all respective loads are applied within a single loadstep. A loadstep is an independent condition relating a given loading condition and structural constraints. If all loading conditions are applied as a single loadstep, the optimizer can perceive enhanced loading on an element or result in a complete disregard on bending with opposing forces [9].

If multiple loadsteps are applied, the optimizer views each condition independently during each iteration. The most convenient way for this to be applied is to set the objective response as a weighted condition. For the case of this research, this is applied as weighted compliance. The response is the weighted global sum of the compliances multiplied by a weighting factor. Mathematically, this is shown in Equation 13 where  $C_w$  is the global compliance,  $w_i$  is the weight factor, and  $C_i$  is the incremental compliance. In this case compliance is defined as the elemental displacement matrix,  $u_i^T$ , multiplied by the applied elemental force,  $f_i$  [9].

$$C_w = \sum w_i C_i = \frac{1}{2} \sum w_i u_i^T f_i \quad (13)$$

Optimized designs are viewed in Hyperview. Hyperview is a visualization environment for Finite Element Analysis (FEA) and Optistruct models [9]. Figure 4 is a topology optimized design from the model setup in Figure 3.

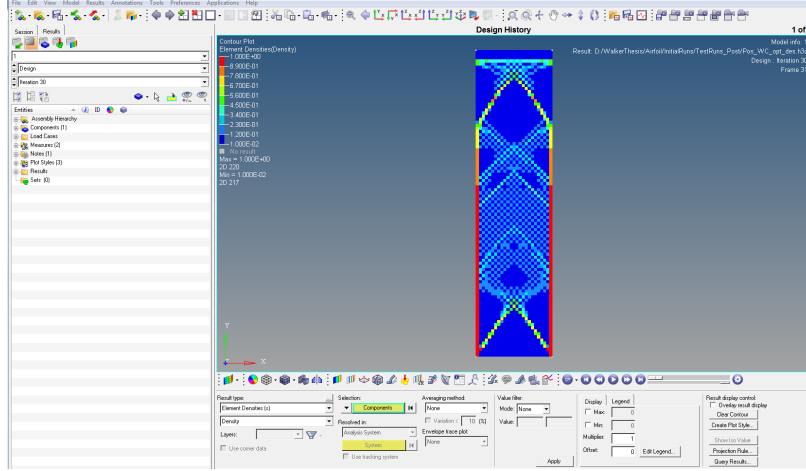


**Figure 4. Hyperview Interface for TO Problem of Multiple Point Loading on Beam**

The problem setup in Figure 3 utilized Equation 13 for an objective to minimize weighted compliance. The results shown in Figure 4 prove the validity of independently optimizing for the given loadsteps. The stiff exterior box which surrounds the design space prevents bending for each load condition. If the loading was summed, per Equation 12, there would be a significant amount of material preventing compression between the forces and very little to prevent bending.

## 2.4 Loading Conditions

An important consideration in quality topology optimization is in applying proper loading conditions. Kroger, Tucker, and Rollema discuss topology and sizing optimizations on the main box wing and leading edge droop-nose ribs on the Airbus A380 commercial aircraft. During their research, it was determined constraints applied locally and constraints applied globally provided significantly different results. This was primarily a result of ill-defined constraints since most aircraft structures rely heavily on external components for load bearing purposes. As a result, simplifying assumptions were made and point constraints were applied at appropriate locations on the design. Doing so significantly simplified the problem set [3].



Aircraft are not the only aerospace component in which topology optimization is studied. In the research completed by Luo, Yang, and Chen, a missile body was topology optimized under both static and dynamic loading conditions. Under static conditions, the optimization objective was to minimize compliance under multiple loading forces. Subsequent testing also considered dynamic loading applied for fatigue testing under free vibrations. However, this is beyond the scope of this research. When considering all the static loads which are applied to a missile body during flight, each load condition will have a respectively different optimal design. A multiple stiffness problem is one in which multiple load cases are weighted respectively during the optimization simultaneously, a capability which is easily accomplished in the Optistruct software discussed in Section 2.3 [9]. The significant problem with this methodology is there is no guarantee all loading conditions are ideally satisfied since it is very difficult to determine proper weighting. Mathematically, the multi-objective optimization problem is defined in Equation 14 where  $x$  is the design variable,  $m$  is the number of loads,  $n$  is the number of finite elements,  $C(x)$  is the objective, and  $q$  is a penalty exponent [14].

$$\begin{aligned}
\min : C(X) &= \sum_{k=1}^m w_k^q \left( \frac{C_k(X) - C_k^{\min}}{C_k^{\max} - C_k^{\min}} \right) \\
\text{Subject to : } &\sum_{k=1}^m \left( \sum_{j=1}^n V_j x_j^k \right) - \bar{V} \leq 0, \\
&0 < x_{\min} \leq x_j < 1, \\
&j = 1, 2, \dots, n; k = 1, 2, \dots, m
\end{aligned} \tag{14}$$

It is also important to consider how complicated the loading on a flying body is in flight. In regards to the missile, the loading is significantly different during each phase of flight. Therefore, only the most severe loading conditions were considered [14].

In the case of aircraft design, maximum forces on the wing occur at maximum and minimum aircraft wing loading conditions. Without consideration of uncoordinated flight, this occurs when the aircraft is at the limits of structural performance [15]. The load factor,  $n$ , is the ratio of lift to weight for an aircraft, seen in Equation 15 [16, 15].

$$n = L/W \tag{15}$$

Here,  $L$  is the lift generated and  $W$  is the weight of the aircraft. The load factor is commonly referred to in  $g$ 's, a weight multiplier times gravity [17]. For a general aviation aerobatic aircraft, the load factor range is  $-3 \leq n \leq 6$ . The load factors imposed by maximum aileron deflection at the maximum load factor are also considered critical for structural analysis on the wing. An aileron deflection of 25 degrees can have an impact of approximately  $\pm 1.0$  on the lift coefficient [15].

## 2.5 Virtual Wind Tunnel

Loading conditions were determined using Altair's Virtual Wind Tunnel (VWT) software. VWT is an easy to use interface for the AcuSolve Computational Fluid Dynamics (CFD) software. VWT models are appropriately meshed in external software and imported as a .nas Nastran solver file. The wind tunnel is sized as desired and conditions for both transient or steady state are defined. Resulting surface pressure conditions are then exported in the format of location (x,y,z) and magnitude [18]. The VWT interface can be seen in Figure 5.

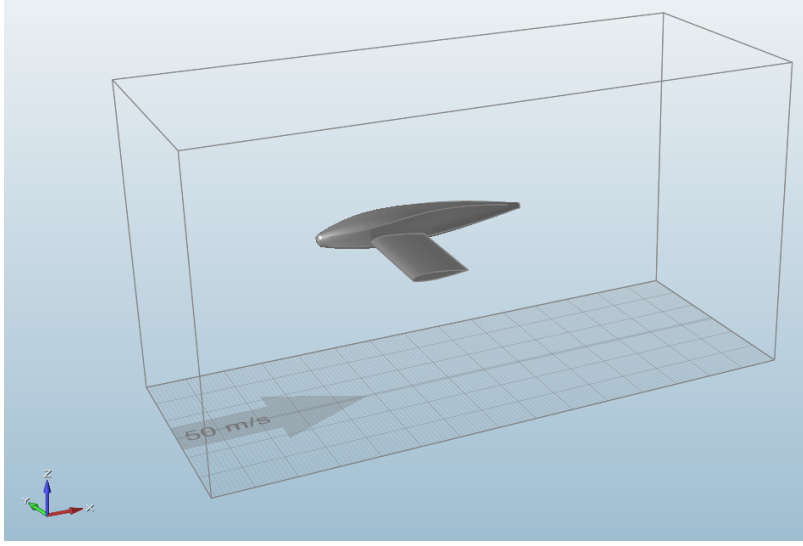


**Figure 5. Model in Virtual Wind Tunnel CFD Analysis Interface**

Virtual wind tunnel uses the AcuSolve CFD solver for analysis [18]. AcuSolve is capable of incompressible flow problems and is based on the Galerkin/Least-Squares (GLS) finite-element method [19]. The GLS method is used to solve Navier-Stokes equations on an unstructured mesh constrained by designated boundary conditions. In general, GLS yields are highly accurate while not requiring high mesh quality [20]. A series of User-Defined Function (UDF) establish operating conditions in the environment [19].

## **2.6 Previous Research**

In general, the aerospace industry optimizes components with an objective of minimum global compliance. This is the case in the research conducted by Kroger, Tucker, and Rollema which examines two very different wing ribs. The first design considered the Airbus main wing box ribs. The current wing box ribs relies primarily on “grid stiffeners” to provide support against buckling while maintaining load support. In this case, an optimized design would suggest a thick exterior edge of isotropic material with a less dense interior of anisotropic material to properly dis-

tribute loading. However, manufacturing such a design is not feasible. Rather, as with most topology optimized designs, a penalization is applied to force a truss-like structure through interpretation of the optimization results [3].

The design is then post-processed to develop a feasible part for manufacture. In the case of the wing box rib, two topology optimized designs were developed with respectively different design areas. During the initial design, only the interior of the rib was optimized, maintaining the surrounding stiff upper and lower channel sections which were used for connections. In this case, only the small interior section was used as a design space for the TO, rather than extending the design space to the edge of the structure. The next design allowed for a complete design area in the rib, only ignoring the flange area as a non design space. The latter most likely provided a more optimized result in its true form, but is not applicable to implementation in the aircraft. However, the results are then easily interpreted into a working design. The most significant problem realized when interpreting TO results is in concerns to buckling, which are often not considered during the optimization process. This solution is often found using rigorous sizing and shape analysis. For the case of the wing box rib, the TO results were used as an initial design for sizing and shape analysis [3].

A more complete analysis, including the complete manufacture of, was accomplished on a leading edge droop nose rib of the A380. In a similar manner to the wing box ribs, the droop nose ribs were optimized to compliance. Due to difficulties in constraining the global structure, constraints in the degrees of freedom planar to the ribs were applied to simulate rib attachments. Rather than directly applying the topology optimization results, the optimal load paths were interpreted into void regions of the component. A sizing optimization was then conducted on the design and out-of-plane vertical stiffeners were applied. Doing so incorporated stress and

buckling constraints in the design. Even though it was determined the topology optimization was beneficial in the design of the rib, no structural performance values were published [3].

A follow-on study was also accomplished in coordination between Airbus and Altair engineers. In “Topology Optimization of Aircraft Wing Box Ribs”, the wingbox of the A380 was examined. This posed new problems which were not seen in previous topology optimized designs at Airbus. Earlier designs, such as fuselage door interstals and leading edge ribs, provided well defined loading conditions [21]. However, a wing box is part of a redundant structure. This can result in the optimization deeming the part at least partially unnecessary. Additionally, the wing box presented an additional challenge where the rib loading changes rather significantly during the optimization process. It was concluded that a weighted-sum of multiple load paths would allow the internal load paths to update during the optimization and likewise ensuring the output was optimized to stiffness [22].

During the optimization of the missile body, the *inertial release analysis method* was used to consider balancing the forces using a set of rotational and translational accelerations which were summed to zero. It is also important to note only the missile body was considered in defining boundary conditions due to variances in scale magnitudes of the compliance [14].

Topology optimization of the missile body reduced weight by 37 percent and compliance by 85 percent. Reconstruction of the model was completed using a conversion from the topology optimization into a geometrical model. The authors used UG CAD software to reduce fragmentary and irregular faces which were generated. The production missile was manufactured with additional constraints in mind and therefore differs from the suggested CAD model. However, it is all based on initial topology optimization [14].

Another aircraft topology optimization was conducted on the cargo structural area of a cargo transport aircraft, the EADS A400M. Constraints on the fuselage consist of outer aerodynamic limitations and inner space consistent with current requirements. Additionally, other constraints such as hinges or required equipment restrain the design. The skin elements also had to retain a minimum thickness in order to ensure proper load distribution. Therefore, the design space for the optimization was similar to current aircraft structure [23].

Initially, single loads were applied in order to study load paths. All the loads were also applied simultaneously. Results show increased material near critical locations. Ideally, this provides increased torsional stiffness while still minimizing weight. A two-dimensional shell optimization was also completed for a more detailed analysis of how the material was weighted for individual sections of the fuselage. Sizing optimization was also completed to study strength, fatigue, and buckling constraints. This study was completed using the in-house LAGRANGE procedure. At the time of publication, the process for the LAGRANGE optimization was ongoing [23].

## **2.7 Related Optimization Research**

Other research relating to aircraft wing optimization are seen with the advent of curvilinear spars and ribs, or SpaRibs. Particularly, two articles from Virginia Polytechnic University have discussed this topic: “Wing-Box Optimization Using Curvilinear Spars and Ribs” by Mulani, Kapnia, and Liu [4] and “Global/Local Multidisciplinary Design Optimization of Subsonic Wing” [24] by Mulani and Kapania and Locatelli.

The initial report discusses the overall practicality of using SpaRibs for aircraft design by investigating characteristics in both a standard rectangular wing and a tapered generic fighter wing. The current design philosophy trend for aircraft is to

move towards *unitized structures* which are characterized by the integration of stiffening members for the rest of the structure. By doing so, manufacturing is streamlined, weight is saved, there is a greater resistance to fatigue/corrosion, enhanced manufacturing automation, and the potential for improved ergonomics. Similar to topology optimization, much of this is or will be, possible because of new additive manufacturing techniques being developed. Generally, optimization will lead to more curvature like designs. SpaRibs can combine the advantages of a variable stiffness design without the use of actuators. Curved beams, which couple torsion and bending, counteract torsional deflection, control natural frequency, exploit coupling of bending and torsion to control flutter, reduce thickness to chord ratios due to increased stiffness, and reduce overall weight [4].

This particular optimization problem considered structural parameters that define general performance of the structure: wing weight, buckling, Kriesselmeyer-Steinhauser stress coefficient, and the von-Mises stress. All of these parameters were considered as either optimization objectives or constraints. Skin thickness and spar location were considered sizing and topology variables, respectively. One significant finding during this research was that buckling was often the limiting factor. Therefore, an increase of the number of SpaRibs was inevitably advantageous. Overall, the process found significant weight savings between 22 and 40 percent of the baseline rectangular wing [4]. It is notable that the baseline wing used for these studies consisted of significantly more ribs than commonly seen in small aircraft, especially the wing used in this research.

The more recent article on SpaRibs by Liu, Mulani, and Kapania evolved the previous research focused on reducing weight within the structure while constraining aerodynamic and aeroelastic effects. A one-step optimization process was used for simplicity of process, where all variables and constraints are included in a single

optimization process. A problem with the one-step approach is too many constraints can cause over complication of the optimization [24].

Another study examined the NASA TO Common Research Model (CRM) wing, which was used and constrained for static aeroelastic, flutter, and buckling loads. During buckling analysis, a global load was applied and an analysis was then conducted at a local level. The problem was divided into a global optimization and a local optimization. When examining global optimization, the topology of the SpaRibs and the thickness of the wing components were optimized considering constraints such as von-Mises stress, maximum displacement, flutter speed, and buckling eigenvalues. The wing internal structure was optimized using SpaRibs and the skin of the wing was optimized through skin thickness in select panels. All together, the optimized wing using SpaRibs and nonlinear skin thickness provided a weight savings of approximately 30 percent [24].

## **2.8 Additive Manufacturing**

Additive manufacturing is the process of adding material in layers as thin cross sections of the desired part [25]. The technology evolved from rapid prototyping techniques developed in the 1990's. The most significant difference between the two is while rapid prototyping develops a visual model, AM seeks to build a functional component [26]. The process entails applying a CAD file as the design of the part and the cross sections are taken as a interpolated slice of the design [25].

A primary goal of AM is to reduce the amount of material used for the production of a part, while reducing cost and/or time to manufacture. Because of this, AM is of great interest regarding high-cost complex aerospace components [26]. Overall, most aerospace industries specialize in low-volume, high-standard parts [27]. More importantly, AM allows for complexities in design which are not seen with traditional



manufacturing methods. In fact, complexity has little impact on the cost to additive manufacturing [28]. For this reason, AM is a significant technology enabler for topology optimization. Designers are therefore granted significantly more design freedom when using the technology [29].

It is still important to note there are significant difficulties in applying AM for topology optimization. Notably, the mesh resolution must satisfy the design. Since a truly topology optimized design using SIMP requires variable density, the material elements must be interpreted appropriately. As a general rule, a member must be at least 3 elements across to ensure an accurate calculation of stiffness. Manufacturing constraints are also apparent in AM, though much less significant than by traditional means. Overhangs in the design can cause for failure during the manufacturing process [30]. For polymer designs, support material is often applied, which is eventually removed, to prevent this from happening. However, metallic designs using laser sintering do not have this capability, at least not as easily [29].

For the purposes of this research, two different additive manufacturing processes were used: UV-cured liquid polymer and Direct Metal Laser Sintering (DMLS). Initial designs were built on an in-house Objet Eden500V. The Eden500V has a build volume of 500 x 400 x 200 mm (19.7 x 15.7 x 7.9 in) and is capable of several different materials, depending on the need. For this research, models were made using Vero family rigid opaque material with photopolymer support. The layer thickness of the machine is 16-microns (0.0006 in) [31]. All models were converted into STereoLithography (STL) format for compliance with the Eden500V printer. STL files are comprised of a series of triangles used to describe the face of the solid [32]. Figure 6 is an image of the Eden500V and Figure 7 is the buildtray.



**Figure 6. Objet Eden500V 3D Printer**

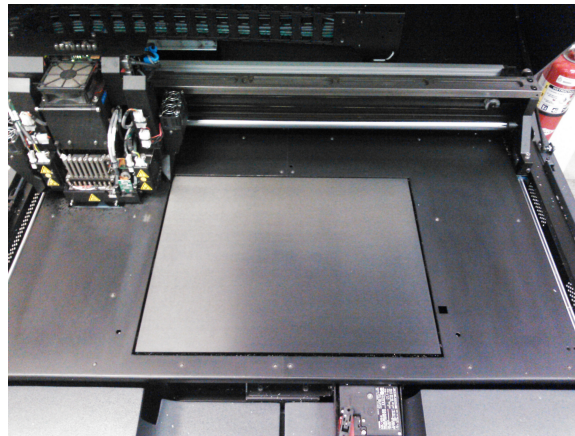


**Figure 7. Objet Eden500V Build Tray**

DMLS is a process which entails applying layers of metallic powder which are thermally fused to a feedstock substrate. DMLS processes can use a variety of metallic powders, including steel, aluminum, and titanium. The powder is melting through the use of a laser energy source [33]. For this research, the DMLS contractor used a EOS M280 DMLS machine. The M280 has a build volume of 250 x 250 x 325 mm (9.85 x 9.85 x 12.8 in) and a 400 Watt laser. The build layer for the machine ranges from 20 to 40 microns (0.0008 to 0.0016 in) [34].

## III. Experimental Setup

### 3.1 Introduction

In order to achieve the objectives of this research, a quality problem setup was required. This includes a review of the software, development of loading conditions, baseline wing analysis, and setup of the optimization problem. All pressure loading conditions were obtained through CFD for given flight profiles. The baseline wing analysis was accomplished through application of these conditions. Additionally, all optimizations were loaded and analyzed under the same pressure loading conditions.

### 3.2 Software Analysis

For methodology verification, a simple optimization was conducted in both Sigmund’s “99 Lines” TO code and compared to two-dimensional Optistruct models. This was done as a means to ensure the Optistruct optimization process is understood. The first test considered a simple cantilever beam constrained in the x-direction on one side and a single point vertical constraint in the y-direction. On the left-hand side, a single vertical force is applied to the top of the design space. The problem setup is seen in Figure 8. The pink is the overall design space and the constraints are colored magenta.

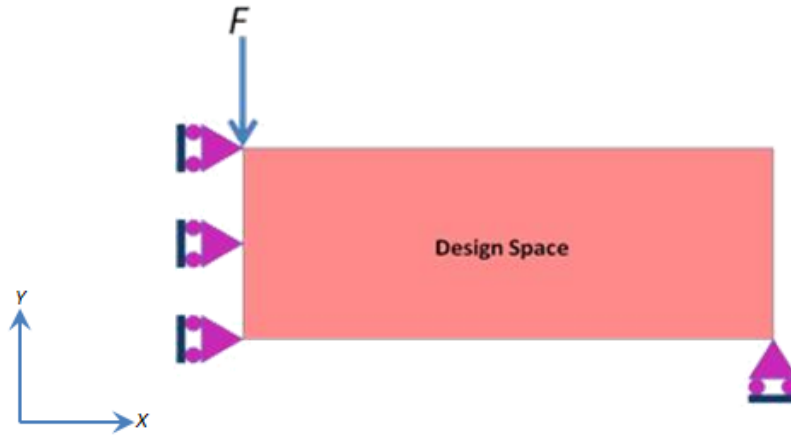


**Figure 8. Cantilever Beam with Constraints and Point Force Problem Setup for TO**

Figure 9a and 9b are the resulting solutions for the 99 lines and Optstruct solvers, respectively. As seen, the solutions are very similar. In both cases, the VF was set to 25 percent of the design space with a discretized area of 60 by 20 elements. A threshold of 50 percent is displayed in the Figure 9b. The most notable difference is the smoothness of boundaries, with the 99 Lines example appearing more pixelated. This is most likely a result of the filtering methodology used with the respective processes.

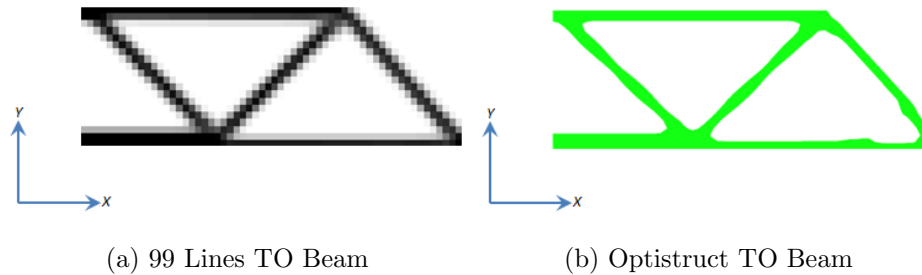


**Figure 9. 99 Line Matlab TO Results vs. Optistruct TO Results for Similar Loading Conditions**

### 3.3 Baseline Aircraft

This research was initially intended for topology optimization of the wing on a small Unmanned Aerial Vehicle (UAV). However, the proprietary nature of most military UAV's made it difficult to obtain quality schematics for a baseline. In order to have access to detailed plans, a homebuilt experimental general-aviation aircraft was chosen. The Van's RV-4 is a relatively acrobatic light single-seat airplane which is popular among enthusiasts. Figure 10 is an engineering drawing of the complete RV-4 [5]. Additionally, aircraft structural specifications are provided in Table 1.

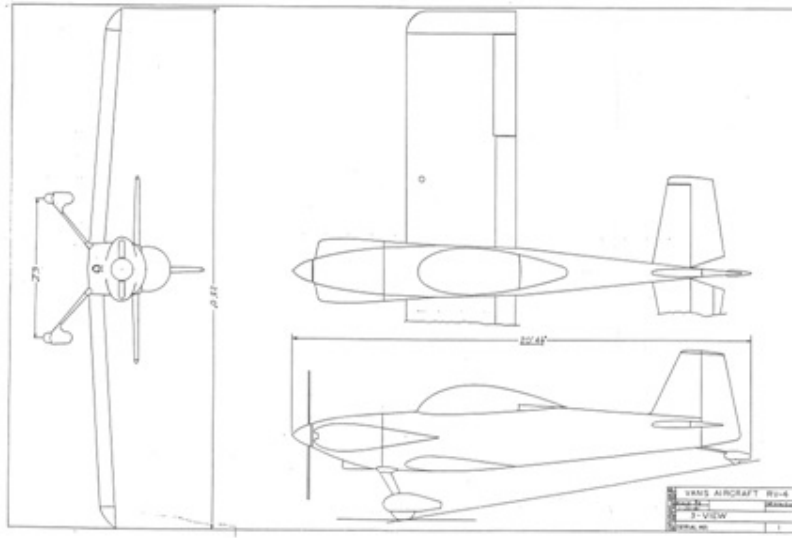


Figure 10. Van's RV-4 Experimental Aircraft Schematic [5]

Table 1. RV-4 Experimental Aircraft Wing Properties and Specifications

Aspect Ratio, $AR$	4.77
Wing Planform Area, $S$	$10.31 \text{ m}^2$ (111.0 $ft$ )
Efficiency factor, $\tau$	0.40 (rectangular wing)
Wingspan	$7.01 \text{ m}$ (23 $ft$ )
Wing Length, ea. (no caps)	$2.8194 \text{ m}$ (9.25 $ft$ )

A primary reason for selecting this particular aircraft is it is relatively high-performance, with a cruising speed of over 200 miles per hour and a climb rate of nearly 200 feet per minute [35]. The wing on the RV-4 is a National Advisory Committee for Aeronautics (NACA) 23015 standard airfoil. Since the RV-4 is not a commercially produced aircraft, the manufacturer does not publish a Pilot Operating Handbook (POH) or information manual. Therefore, an information manual from a comparable production aircraft was used for specific performance specifications. The aerobatic Extra-200 was chosen due to its relatively similar performance characteristics and aircraft design. The only significant performance specifications taken from the Extra-200 information manual was the maneuvering speed of 138 Knots-Indicated Air Speed (KIAS) (71 m/s) and load factor limitations [36]. It is important to note the exact aircraft performance specifications are not overly important since the same values were applied to baseline testing. As long as there is consistency, the optimized design process is viable.

The wing on the Van's RV-4 consists of 14 ribs and 2 spars built from 2024-T4 Aluminum sheet metal which is formed into channels for structural support. The wing is also wrapped in 2024-T4 acting as the skin to retain the aerodynamic shape [5]. Metal thickness ranges from 0.025 to 0.040 inches, depending on its specific function. Table 2 lists the material properties used for analysis [37]. Figure 77, found in Appendix A, is a schematic for the baseline Van's RV-4 wing. Appendix A also contains schematics for the ribs and fuel tank, Figure 78 and Figure 79, respectively.

**Table 2. 2024-T4 Aluminum Material Properties**

Modulus of Elasticity, $E$	7.31e10 Pa
Density, $\rho$	2780 $kg/m^3$
Poisson's Ratio, $\nu$	0.33
Tensile Strength, yield	275 $MPa$
Tensile Strength, ultimate	469 $MPa$
Bearing Strength, yield	441 $MPa$
Bearing Strength, ultimate	814 $MPa$

In Figure 77, the wing tip and flaps/ailerons are grayed out since they were not considered for analysis, other than for initial designs. Additional text over the original schematic notation was also included for clarification purposes. The fuel tank, highlighted in green, was also disregarded for the initial baseline analysis. However, it was considered for comparison to the tank integration optimization.

### 3.4 Initial Design Loading Conditions

During initial 2D and 3D wing segment optimizations, Xfoil Subsonic Airfoil Development System software [38] was used to determine loading conditions on the wing. Since Xfoil outputs pressure coefficient values ( $C_p$ ) for a 2D airfoil, the pressure on early 3D models was uniform laterally along the length of the wing. This is unrealistic since there are significant pressure changes along the wing moving from the root to tip. Likewise, 2D models were set with maximum pressure which is theoretically seen at the root of the wing. The airfoil was also set at an zero angle of attack ( $\alpha$ ). This does not correspond to a specific flight condition. The RV-4 maximum cruising velocity of 95 m/s [35] was chosen to convert  $C_p$  to actual pressure on the wing skin. Maximum cruising speed does not relate to maximum loading conditions on the wing

and the chosen  $\alpha$  does not necessarily relate to a specific flight profile. Rather, these conditions were set as a baseline to establish the initial optimization process. The Xfoil output for the NACA 23015 2D airfoil section at zero  $\alpha$  is seen in Figure 11.

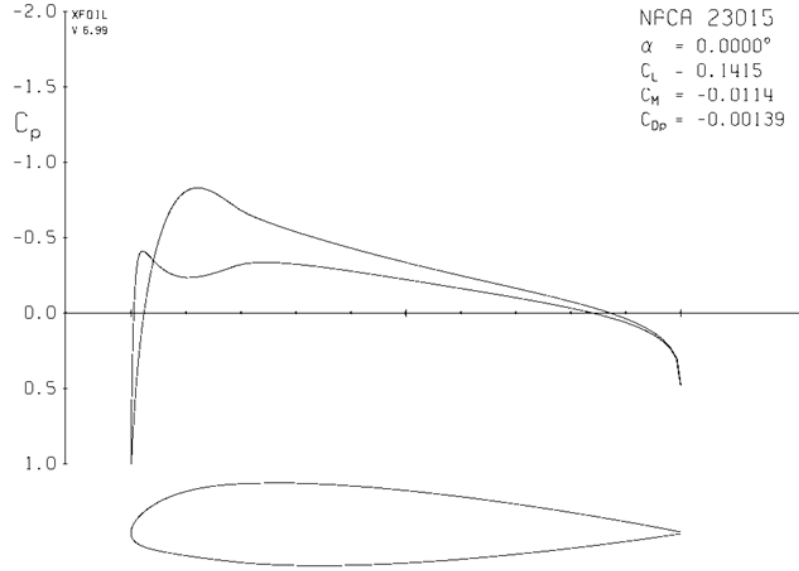


**Figure 11. NACA 23015 Airfoil  $C_p$  Distribution for Zero  $\alpha$**

The values from Xfoil were output as x and y locations, along with a pressure magnitude in pascals (Pa). Since applying normal forces to 2D elements in Hypermesh is tedious, pressure was applied only as horizontal and vertical vectors applied to the surface. This provided a process verification, but the results were not ideal. Forces for a 3D body were applied as pressure values. The result is a force vector normal to its respective element. Since pressure is  $\frac{Force}{Area}$ , the vector magnitude is a function of element size. The pressure magnitudes are also relative to the ambient total pressure. Therefore, pressure magnitudes less than the total pressure appear negative. This causes a normal outward force on the surface in which the pressure is applied.



### 3.5 Initial Designs

Early wing renditions consisted of a complete NACA 23015 airfoil in both two and three dimensions. This wing section has a width of 0.5 meters. In order to retain the shape, a thin skin, non-design space surrounded the interior design space. Loading was only applied as force vectors to the skin surface. Two circular supports were set on the interior of the wing as points in which to structurally constrain the design. An image of the two-dimensional design setup is seen in Figure 12 and the three-dimensional setup in Figure 13. In both of these examples, the design space is blue, the non-design skin is red, and the structural constraints are magenta. Loading and constraint conditions are shown in Figure 14 and Figure 15, respectively. In this case, both spars are constrained throughout their length.

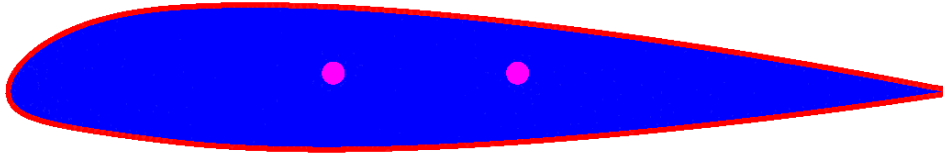


Figure 12. Initial 2D Design Space Problem Setup of Optistruct TO

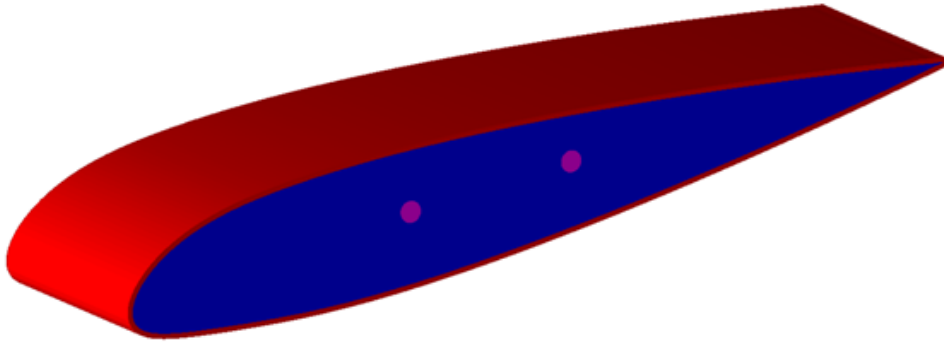
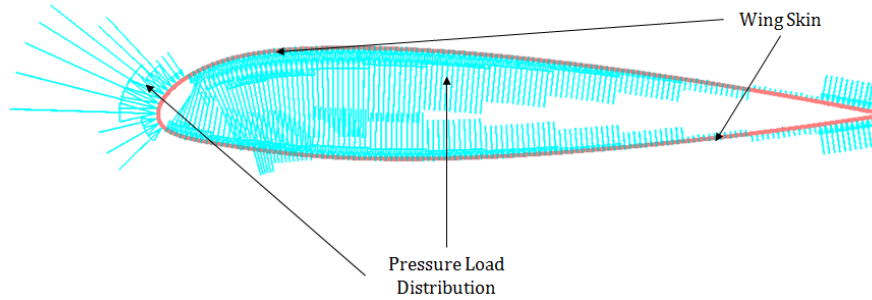
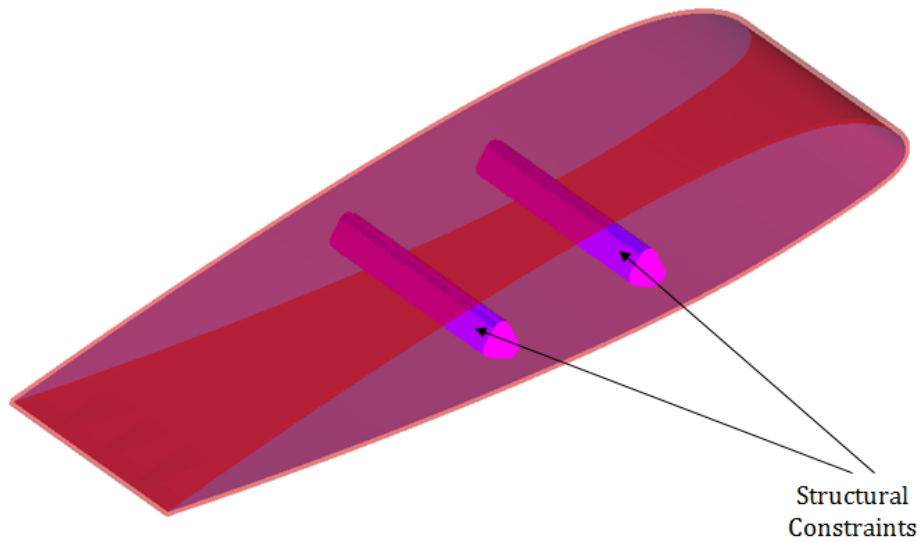


Figure 13. Initial 3D Design Space Problem Setup of Optistruct TO



**Figure 14. Force Load Conditions for Initial Optistruct TO Analysis**



**Figure 15. Structural Constraints for Initial Optistruct TO Analysis**

All initial designs were optimized with an objective of minimizing compliance while constrained to a VF. The exact value in which to constrain the VF to is an iterative process requiring an interpretive analysis of the results. An attribute of variable density TO is a change in VF will not necessarily result in a significantly different shape. Rather, the density fraction for each element is function of the optimization VF. Example results for an initial 2D design from Figure 12 are shown in Figure 16. In this case, the design was constrained to a 30 percent VF with an objective of minimum compliance. The disconnected members near the rear of the airfoil are a result of the partial density found in the TO results; at these locations, the density

of the member is very near 38 percent causing some elements to be void [39].



**Figure 16. Optistruct TO Result for 2D Design Space with Given Loading Conditions and Constraints**

### 3.6 Advanced Loading Conditions

In order to create higher levels of fidelity, a Computation Fluid Dynamics (CFD) analysis on the wing body was performed. This study provided pressure loading conditions for various flight conditions. As discussed in Section 2.4, the most significant loads result from the most extreme flight profiles. Specifically, at the maximum and minimum load factor [15]. For an aerobatic aircraft, this is at positive  $6g$ 's and negative  $3g$ 's [15]. This simulates maximum structural support for a full stick-back or stick-forward maneuver. The Extra 200 information manual confirms this information [36]. Additionally, full aileron deflection is considered at maximum positive loading, which is a result of a stick-back, rolling maneuver [15].

Since all data for this research considers only static loading conditions, flight profiles were determined in which the wing generated enough lift to create the desired load factor, per Equation 15. An aircraft gross weight of  $1,500\text{ lb}$  ( $680\text{ kg}$ ) was used [35, 36]. This means for a positive  $6g$  condition, the wing would need to produce  $9,000\text{ lb}_f$  of lift. To do so, the wing is at an increased angle of attack. The  $\alpha$  was determined using a interpolation technique of a section lift coefficient,  $c_l$ , chart as a function of  $\alpha$ . Figure 17 is an adaptation of a  $c_l$  vs  $\alpha$  chart for a NACA 23015 airfoil [40].

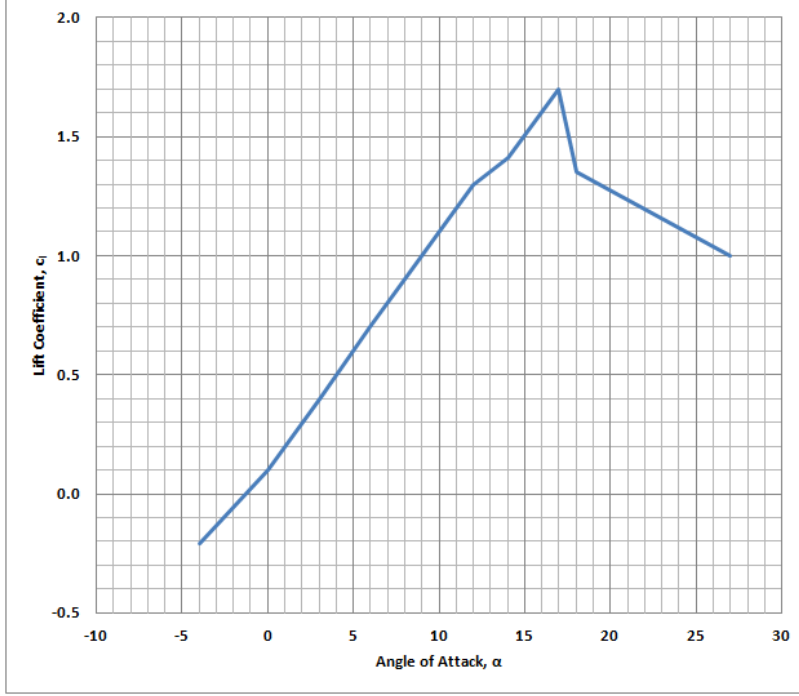


**Figure 17. NACA 23015 Airfoil  $c_l$  vs  $\alpha$  Chart [40]**

This data is for a two-dimensional airfoil, which does not experience pressure loss laterally along the wing. Therefore, it was necessary to calculate the total wing lift coefficient  $C_L$ . The wing lift slope angle,  $a$ , was calculated using Equation 16 and the section lift slope angle,  $a_0$  [16]. This is a best guess estimation for lift slope base on heuristics and wind-tunnel testing. Aspect Ratio ( $AR$ ) and  $\tau$  and were obtained from Table 1. Even though the -3g flight condition  $\alpha$  is beyond the chart limits of Figure 17, it is a linear interpolation of the data. Additionally, the negative  $\alpha$  is much less susceptible to stalling and is likewise a reasonable value.

$$a = \frac{a_0}{1 + \frac{a_0}{\pi AR}(1 + \tau)} \quad (16)$$

The lift slope was calculated as  $4.091/rad$  ( $0.715/deg$ ). This resulted in the lift shown in equation specific to this wing, shown in Equation 17.

$$C_L = 0.0715\alpha + 0.143 \quad (17)$$

Finally, the total lift,  $L$ , required was calculated using Equation 18. Atmospheric density,  $\rho$ , is standard sea level atmospheric at  $1.2250 \text{ kg/m}^3$  ( $2.3769e^{-3} \text{ slugs/ft}^3$ ). Velocity,  $V$ , is the aircraft velocity. For this case, the RV-4 maneuver speed of  $71 \text{ m/s}$  ( $159 \text{ mph}$ ). Wing planform area,  $S$ , was obtained from Table 1. The results are seen in Table 3.

$$C_L = \frac{L}{\frac{1}{2}\rho V^2 S} \quad (18)$$

**Table 3. Wing Angle of Attack for Given Load Factor of NACA 23015 Airfoil at RV-4 Maneuver Speed**

Load Factor, $n$	Angle of Attack, $\alpha$
+6g	$15.58^\circ$
-3g	$-10.8^\circ$

A CFD model was then built to run in Virtual Wind Tunnel (VWT). The model consists of the RV-4 wing and a generic fuselage shape, to account for lateral pressure loss. The model was oriented for both the positive and negative load factor  $\alpha$ 's. Additional, a VWT model with aileron deflection for both a right and left roll was applied at positive load factor position. A maximum aileron deflection of 25 degrees in each direction was used. The model for level flight and the model for right roll are seen in Figure 18a and 18b, respectively. Input conditions consisted of the aircraft maneuvering speed of  $71 \text{ m/s}$ .

VWT output consists of surface pressure on the test body. Figure 19 illustrate the wing surface pressure for the various models in pascals (Pa). The associated color

scale is attached to each figure.

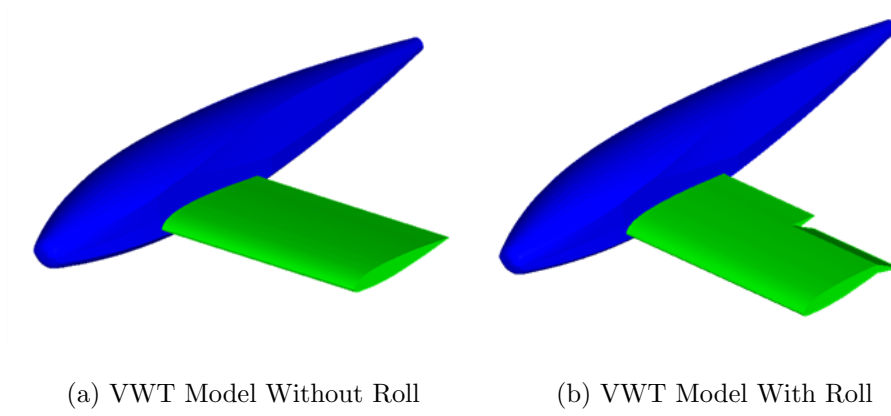


**Figure 18. Virtual Wind Tunnel Wing Pressure Load Model for CFD Analysis**

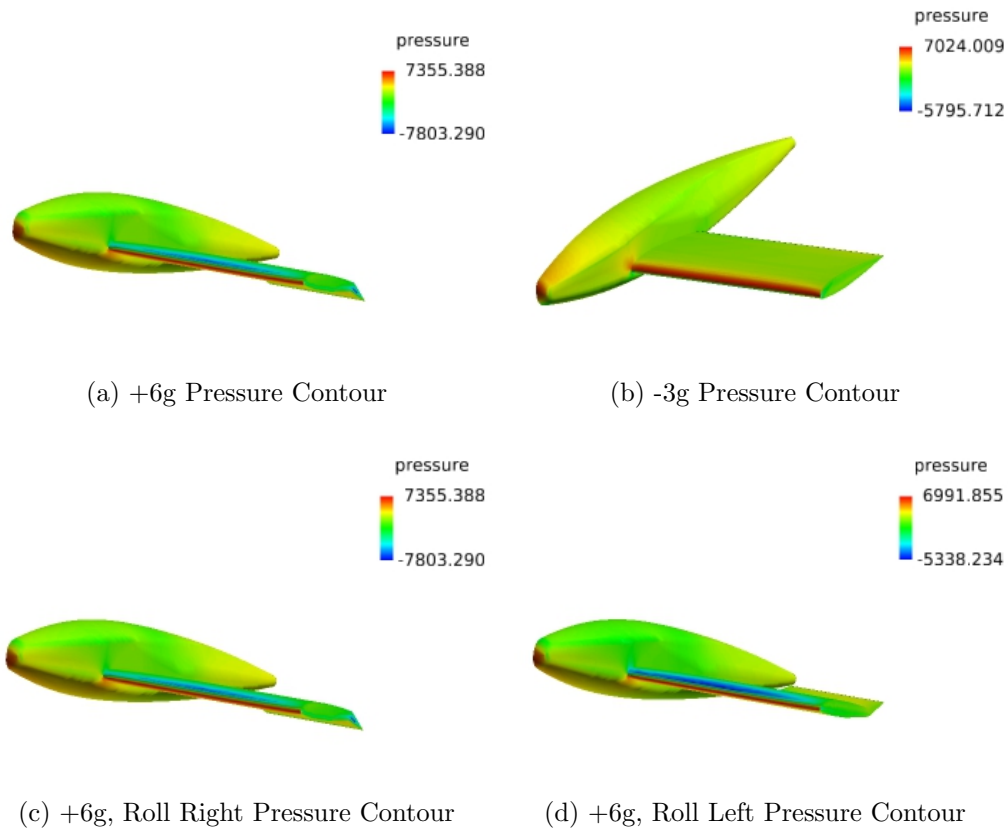


**Figure 19. VWT Model Pressure Contours for Each RV-4 Manuever Flight Profile**

The resulting pressure values were then applied to the wing as an individual load

step. This was done through a built in Optistruct function which linearly interpolates pressure values to a discretized domain and applies the appropriate pressure on each element. In this research, this was done on the wing skin. The +6g flight profile example for pressure loading applied to the wing skin is seen in Figure 20. All models were also structurally constrained for all axial directional and rotational Degrees of Freedom (DOF). Constraints were applied on the spars only at the root and along the edge of the skin at the root. Figure 21 shows the constraints illustrated on the discretized non-design domain. In this figure, the constraints are magenta. As shown, the constraints are applied to both spars, and nodes along the entire root edge of the skin.

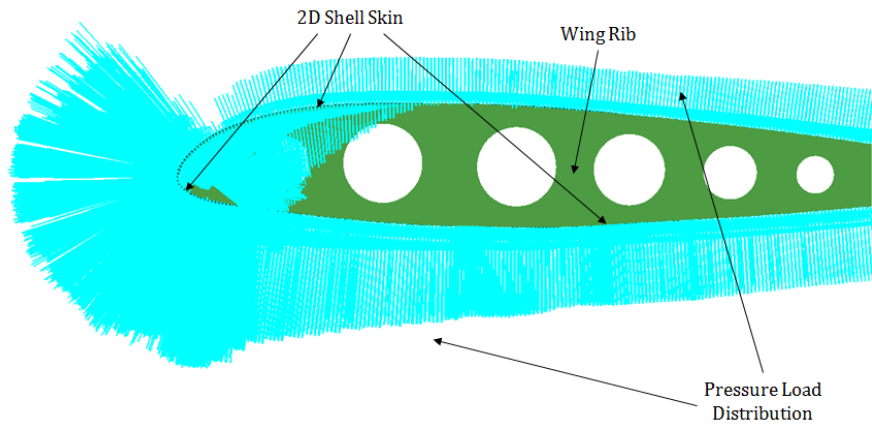


**Figure 20. Pressure Load Conditions for +6G Flight Profile**

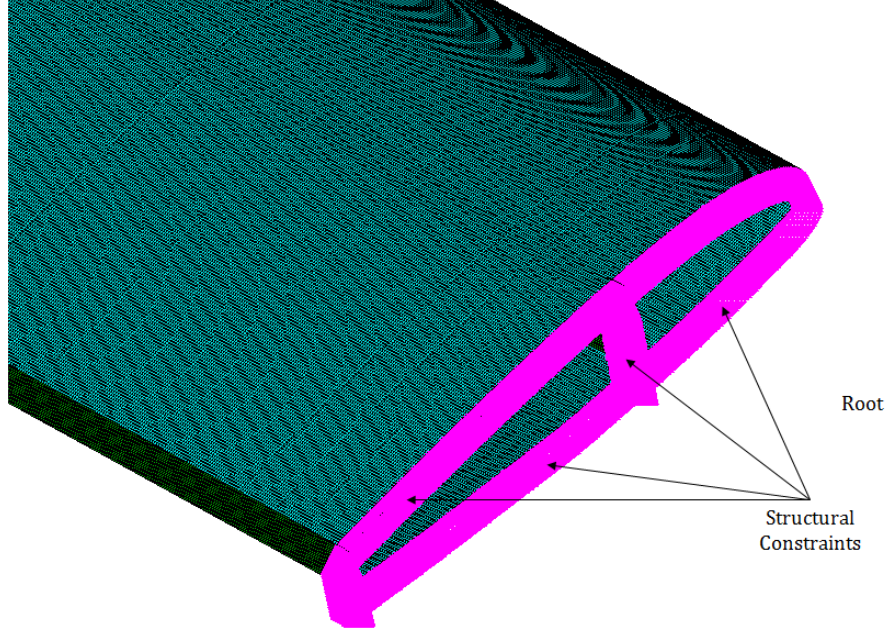


Figure 21. Structural Constraints for All Advanced Loading Conditions

### 3.7 Baseline Analysis

#### 3.7.1 Setup.

For comparative purposes, an analysis on the baseline wing was conducted. The wing design was adapted from the Van's RV-4 plans [5], as shown in Appendix A. Most of the TO in this research was conducted without consideration of a fuel tank. Therefore, the respective baseline wing was also analyzed without a tank. The wing was broken down into three components: spars, ribs, and skin. There are two lateral spars for wing stiffness, and 14 ribs which support the aerodynamic shape. All components were built as 2D shell structures with assigned thickness values for the metal. Figure 22 is an image of the baseline wing. Table 4 is the respective material thickness. Pressure loading was applied as discussed in Section 3.6.



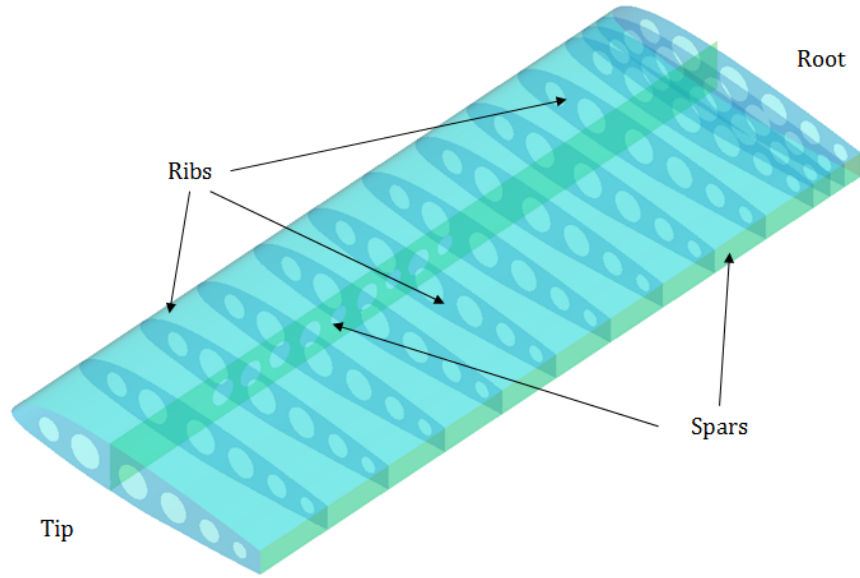


**Figure 22. Baseline RV-4 Wing for Initial Performance Analysis**

**Table 4. Baseline Wing Component Material Thickness for 2024-T4 Aluminum Sheet Metal**

Component	Material Thickness
Skin	0.813 <i>mm</i> (0.025 <i>in</i> )
Spars	1.016 <i>mm</i> (0.032 <i>in</i> )
Ribs	0.813 <i>mm</i> (0.025 <i>in</i> )

In addition to the individual skin thickness, the individual component surface areas and volumes were calculated. This was also accomplished for each TO design for comparative purposes of mass savings of the optimized design. These values are outline in Table 5.

**Table 5. Baseline Wing Component Surface Area, Volume, and Mass**

	Each Rib	Total Rib	Front Spar	Rear Spar	Skin	Total
Surf Area ( $m^2$ )	0.128	1.795	0.506	0.284	6.479	9.064
Volume ( $m^3$ )	$0.10 \times 10^{-3}$	$1.46 \times 10^{-3}$	$0.51 \times 10^{-3}$	$0.29 \times 10^{-3}$	$5.23 \times 10^{-3}$	$7.49 \times 10^{-3}$
Mass ( $kg$ )	0.289	4.059	1.429	0.803	14.539	20.831

### 3.7.2 Results.

Analysis was conducted for stress, displacement and buckling. Stress is analyzed using the von-Mises stress criterion and displacement is simply the distance an element is displaced from the zero-load condition. Buckling is measured as the buckling load factor, per Equation 8. BLF is considered the fraction of the current load in which buckling will occur. Once buckling does occur, the load required to maintain buckling is usually less than the buckling load. Regardless, buckling does not necessarily result in failure, as long as it does not reach a critical point.

The first baseline wing analysis was a complete displacement analysis for the various loading conditions. This is a measurement of nodal displacement from the initial condition once steady-state conditions are reached. Inherently, virtually all wings have some amount of deflection. For the low aspect ratio wing used in this research, the deflection is relatively small. Excessive wingtip deflection can cause higher stress loading and cyclical fatigue failure. Additionally, deflection results in a change of pressure and drag profiles for the wing. An optimized wing would therefore maintain or decrease the baseline deflection. Figure 23 shows the wing displacement for the respective load in meters. The maximum displacement seen is 0.0492 meters (1.93 inches) for the +6g, roll-right load case. However, it is a case of skin deflection between ribs at extreme conditions. Rather, the tip deflection experienced is slightly

less at approximately 0.0390 meters (1.54 in).

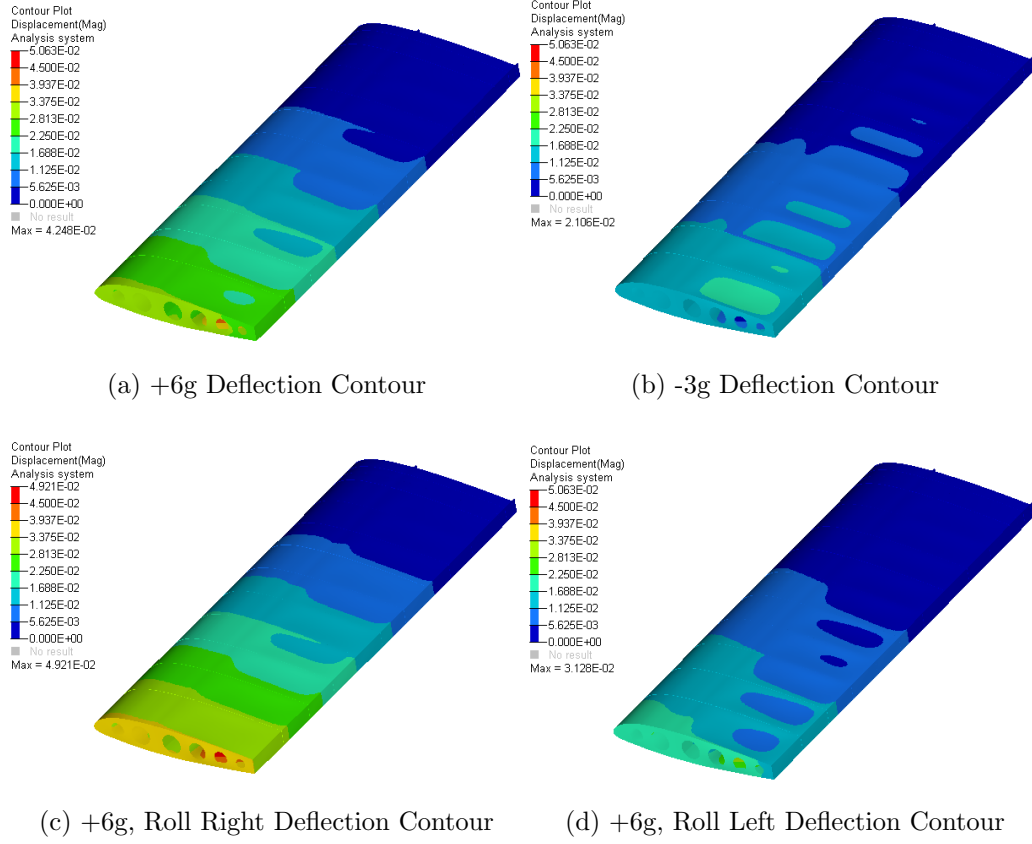


**Figure 23. Wing Deflection Contours for Each Flight Profile of Baseline Wing**

Localized stress on the wing is an important consideration when determining the likelihood of structural failure under given loading conditions. Material strengths are listed in Table 2. The local maximum stress on a truly optimized design should not exceed the maximum stress on the baseline. Von-Mises stress on the wing are seen in Figure 24 and Figure 25. This is the same wing shown with and without the skin, respectively. For the baseline wing, peak stress generally occurs on the internal spar. However, this is not necessarily the case for the optimized designs. Stress contour values are in Pascals. Maximum stresses generally occur at the root of the front spar at the upper and lower corners. Maximum von-Mises stress obtained was at the +6g, roll-right load case at 207.9 MPa. Displacement and stress results are seen in Table

6.

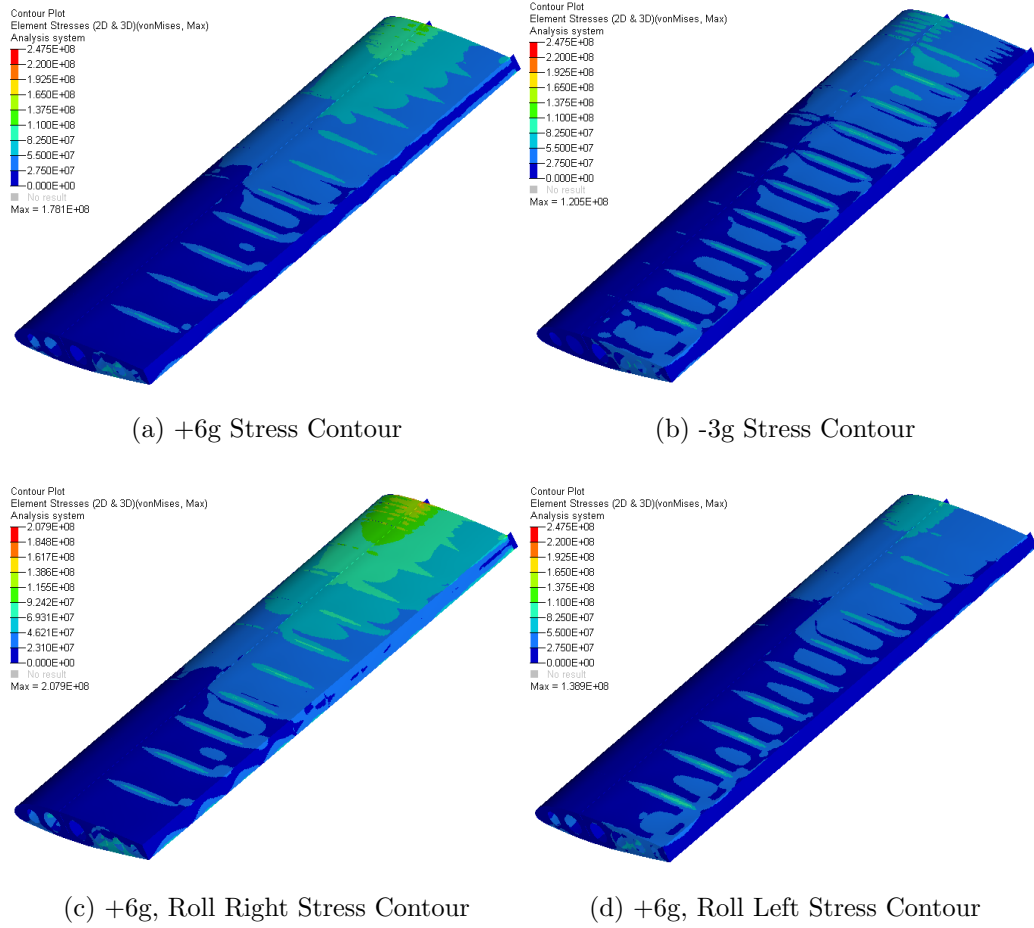


**Figure 24. Wing Stress Contours for Each Flight Profile of Baseline Wing Skin**

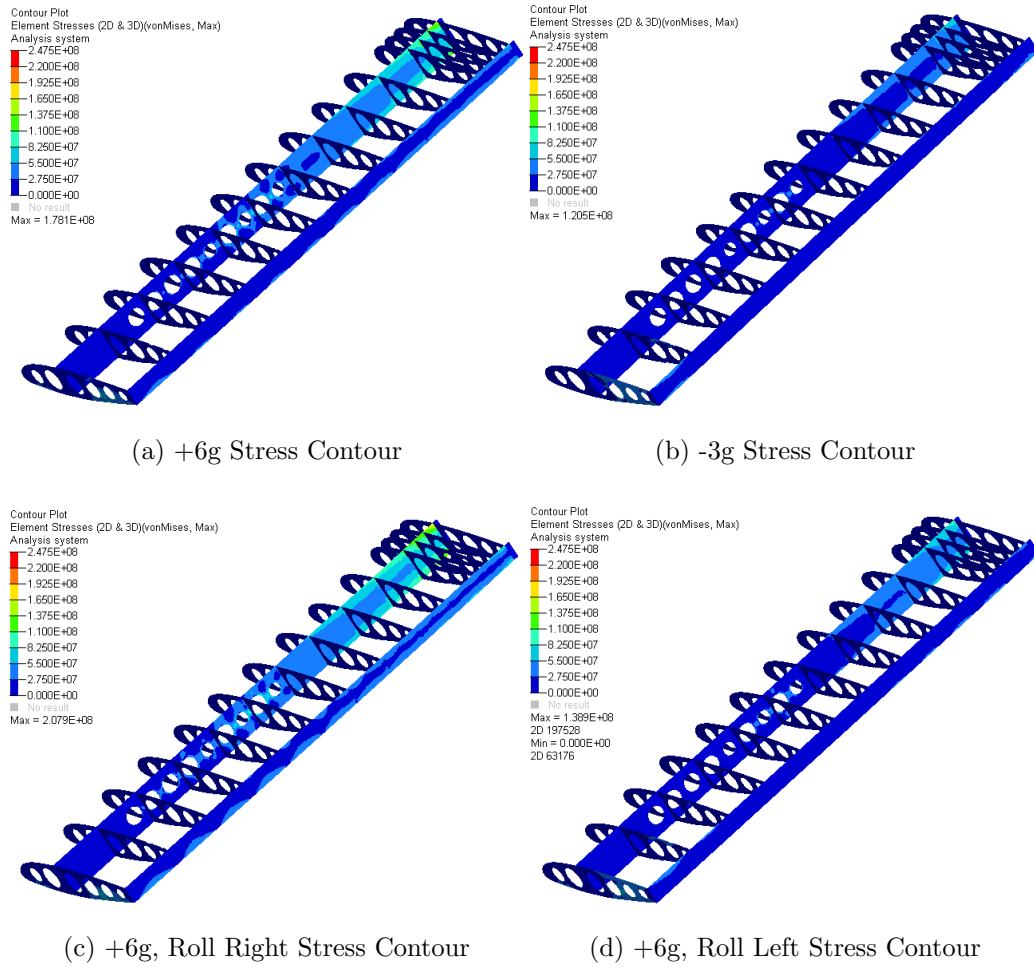


**Figure 25. Wing Stress Contours for Each Flight Profile of Baseline Wing Internal Structure**

**Table 6. Displacement and Stress of Baseline Wing**

Condition	Total Displacement	Tip Displacement	von-Mises Stress
+6g	0.0425 m (1.67 in)	0.0338 m (1.33 in)	187.1 MPa
-3g	0.0211 m (0.83 in)	0.0167 m (0.66 in)	120.5 MPa
+6g, Roll Right	0.0492 m (1.93 in)	0.0390 m (1.54 in)	207.9 MPa
+6g, Roll Left	0.0313 m (1.23 in)	0.0225 m (0.89 in)	138.9 MPa

Finally, a buckling analysis was performed. Many aircraft structures consist of

long slender components which are susceptible to buckling. Elastic buckling is acceptable and can safely occur. However, failure occurs with inelastic buckling, which results from a stress which exceeds a proportionality limit. The BLF, as discussed in Section 2.2, of an optimized wing should not exceed this limit. Intuitively, the most severe buckling occurred during the +6g, roll right maneuver at the root of the wing. Therefore, the buckling contour for the first three modes is shown in Figure 26 for the given load condition. The BLF for each conditions is shown in Table 7.

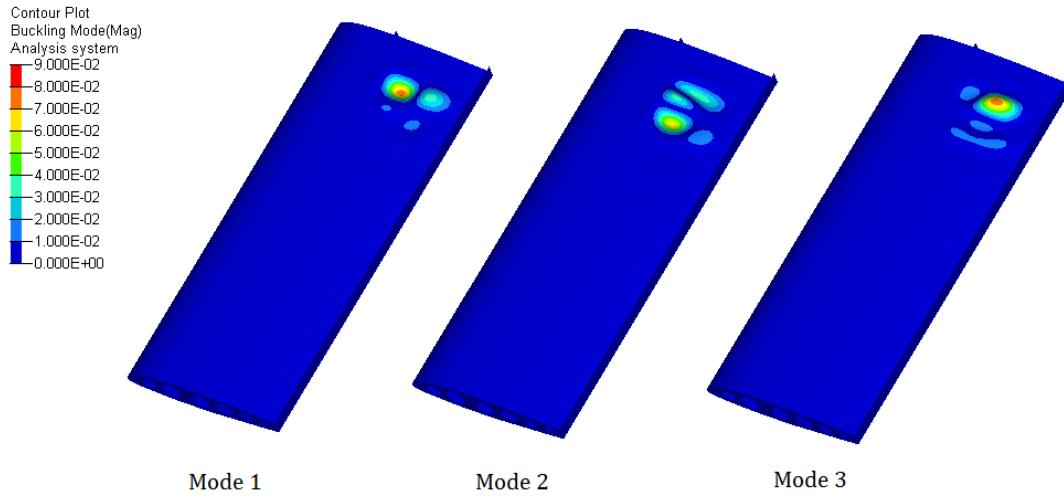


**Figure 26. Buckling Analysis for +6g, Rolling Right for Baseline Wing**

**Table 7. Buckling Load Factor of Baseline Wing**

Condition	Buckling Load Factor		
	Mode 1	Mode 2	Mode 3
+6g	0.095	0.102	0.106
-3g	0.104	0.129	0.153
+6g, Roll Right	0.081	0.086	0.089
+6g, Roll Left	0.143	0.155	0.165

### 3.7.3 Analysis for Baseline Wing with Tank.

In a similar fashion to the wing studied in Subsection 3.7.1, the RV-4 fuel tank was integrated into the model. As seen in Figure 77 and Figure 79 in Appendix A, the tank is located on the leading edge and root of the wing. The tank is independently constructed and consists of a series of leading-edge ribs and an additional rear spar. Even though the internal tank components are easily separated from the rest of the wing, the aluminum skin of the wing encloses the tank structure. All joints and rivets are sealed post-assembly [5]. For the FEA model, the tank ribs were appropriately placed along the spar. Rather than constructing an independent rear spar for the tank, the main spar thickness was increased to the combined spar thickness value for the respective length. Component thickness is consistent with Table 4. Figure 27 is a view of the model wing tank. A summary of the volume and mass of this model is outline in Table 8.

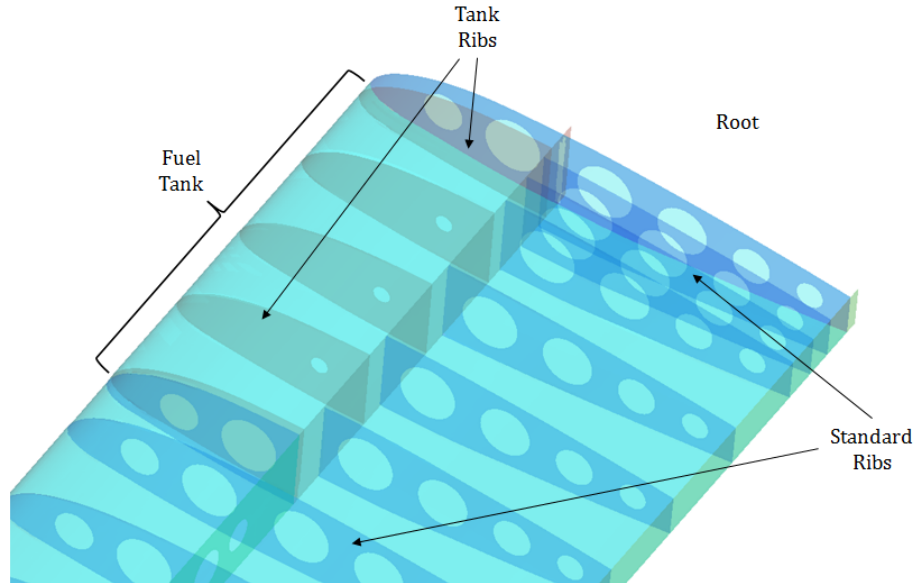


**Figure 27. Baseline RV-4 Wing Tank**

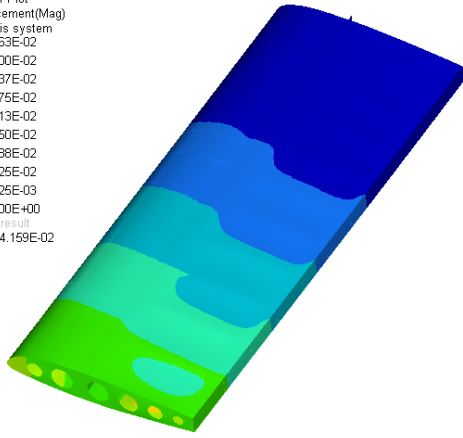
**Table 8. Baseline Wing with Fuel Tank Component Surface Area, Volume and Mass**

	Total Rib	Spars	Fuel Tank	Skin	Total
Surf Area ( $m^2$ )	1.545	0.792	0.624	6.479	9.440
Volume ( $m^3$ )	$1.21 \times 10^{-3}$	$0.80 \times 10^{-3}$	$0.56 \times 10^{-3}$	$5.23 \times 10^{-3}$	$7.85 \times 10^{-3}$
Mass ( $kg$ )	3.482	2.236	1.565	14.539	21.822

The baseline wing with a tank was subjected to the same loading conditions as the wing without the tank. Displacement, stress, and buckling factors were considered for all flight profiles. The analysis was used for the integrated tank optimization discussion in Section 4.4.1. Baseline wing tank results for displacement and stress are shown in Figure 28 and Figure 29, respectively. For this case, the peak stress occurs on the wing skin. Therefore, the stress contours are shown with the skin on, opposed to the layout of the Figure 25 images. The maximum deflection and stress values for each flight profile are outlined in Table 9.

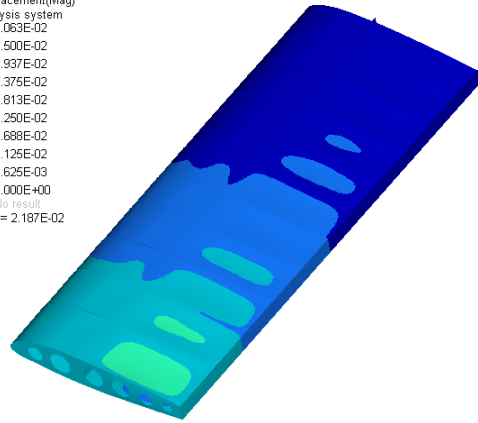


Contour Plot  
Displacement(Mag)  
Analysis system  
5.063E-02  
4.500E-02  
3.937E-02  
3.375E-02  
2.813E-02  
2.250E-02  
1.688E-02  
1.125E-02  
5.625E-03  
0.000E+00  
No result  
Max = 4.159E-02



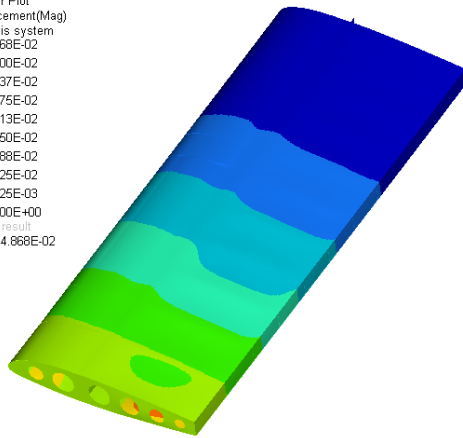
(a) +6g Deflection Contour

Contour Plot  
Displacement(Mag)  
Analysis system  
5.063E-02  
4.500E-02  
3.937E-02  
3.375E-02  
2.813E-02  
2.250E-02  
1.688E-02  
1.125E-02  
5.625E-03  
0.000E+00  
No result  
Max = 2.187E-02



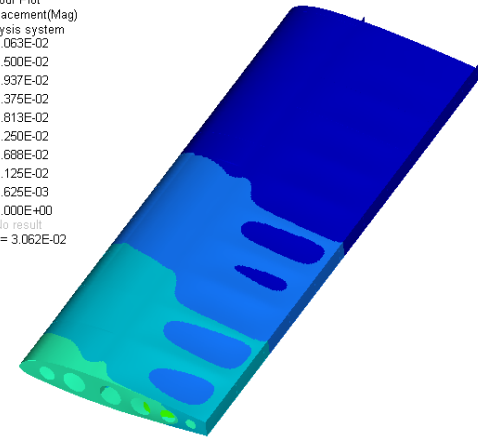
(b) -3g Deflection Contour

Contour Plot  
Displacement(Mag)  
Analysis system  
4.868E-02  
4.500E-02  
3.937E-02  
3.375E-02  
2.813E-02  
2.250E-02  
1.688E-02  
1.125E-02  
5.625E-03  
0.000E+00  
No result  
Max = 4.868E-02



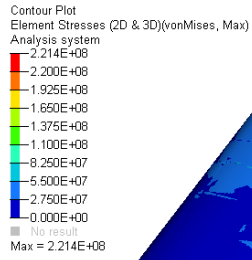
(c) +6g, Roll Right Deflection Contour

Contour Plot  
Displacement(Mag)  
Analysis system  
5.063E-02  
4.500E-02  
3.937E-02  
3.375E-02  
2.813E-02  
2.250E-02  
1.688E-02  
1.125E-02  
5.625E-03  
0.000E+00  
No result  
Max = 3.062E-02

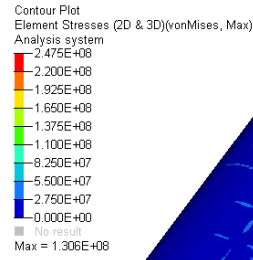


(d) +6g, Roll Left Deflection Contour

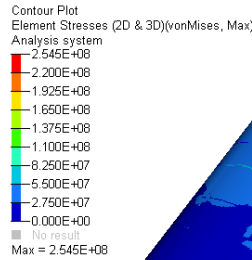
**Figure 28. Wing Deflection Contours for Each Flight Profile of Baseline Wing with Fuel Tank**



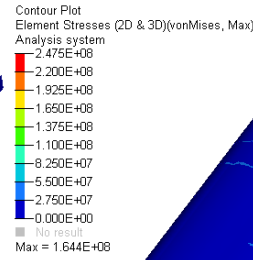
(a) +6g Stress Contour



(b) -3g Stress Contour



(c) +6g, Roll Right Stress Contour



(d) +6g, Roll Left Stress Contour

**Figure 29. Wing Stress Contours for Each Flight Profile of Baseline Wing with Fuel Tank**

**Table 9. Displacement and Stress of Baseline Wing with Fuel Tank**

Condition	Total Displacement	Tip Displacement	von-Mises Stress
+6g	0.0416 m (1.64 in)	0.0323 m (1.27 in)	221.4 MPa
-3g	0.0201 m (0.79 in)	0.0156 m (0.61 in)	130.6 MPa
+6g, Roll Right	0.0487 m (1.92 in)	0.0379 m (1.49 in)	254.5 MPa
+6g, Roll Left	0.0306 m (1.20 in)	0.0204 m (0.80 in)	164.4 MPa

Additionally, the buckling analysis is shown in Figure 30 for the first three modes of buckling. Table 10 outlines the BLF for the respective modes and load conditions. Once again, these BLF values were used for comparison to the optimized wing with an integrated fuel tank.

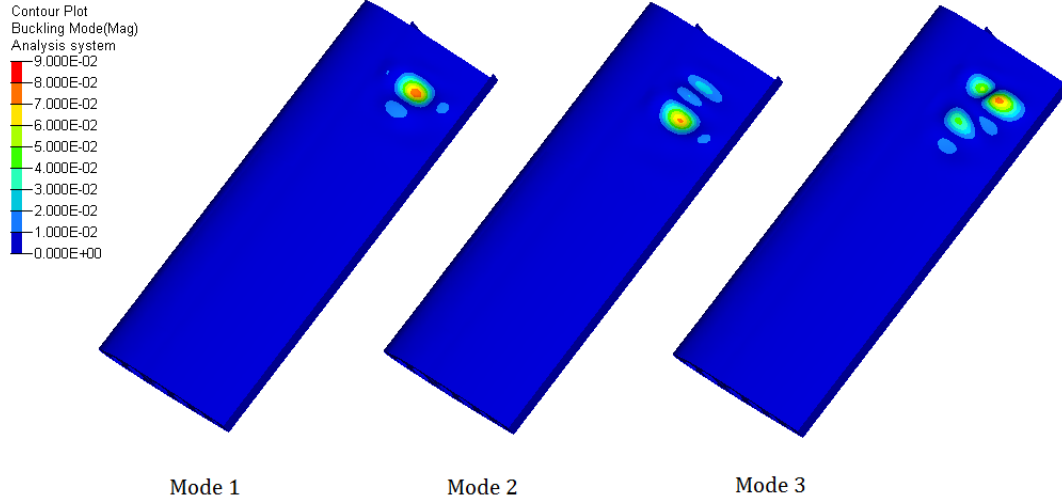


Figure 30. Buckling Analysis for +6g, Rolling Right for Baseline Wing with Fuel Tank

Table 10. Buckling Load Factor of Baseline Wing with Fuel Tank

Condition	Buckling Load Factor		
	Mode 1	Mode 2	Mode 3
+6g	0.094	0.102	0.111
-3g	0.109	0.134	0.157
+6g, Roll Right	0.079	0.086	0.093
+6g, Roll Left	0.142	0.153	0.167

### 3.8 Local Optimizatation

A 2D optimization on the existing ribs was conducted as an alternative method of TO compared to a 3D global optimization. In this case, the ribs and spars were

placed in the same spanwise location as the baseline, but with each rib area consisting entirely of a design space; all holes in the ribs were removed. The element thickness also remained the same as the baseline optimization, per Table 4. Loads were applied in a manner discussed in Section 3.6. The design space setup is seen in figure 31. The design space is colored blue.

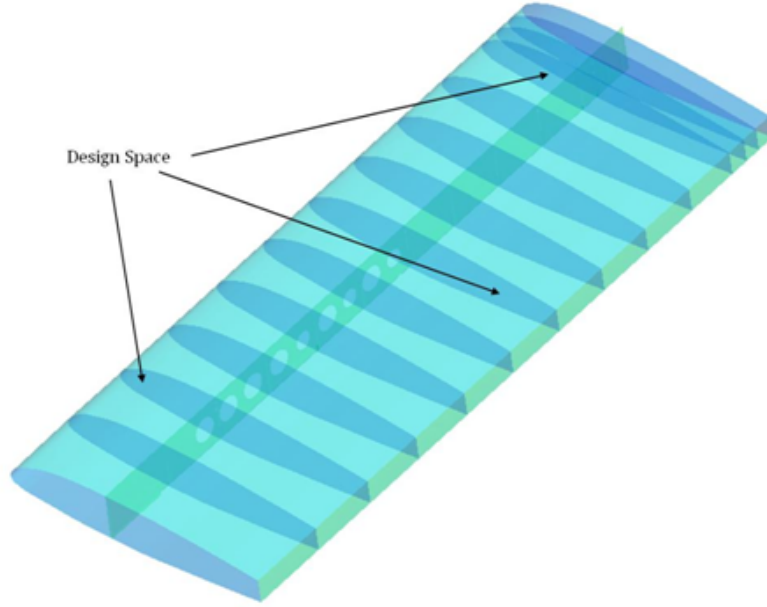


**Figure 31. Local TO 2D Rib Problem Setup**

In the first case, only the ribs were topology optimized while the baseline skin and rib thickness was maintained. The optimization was performed with and without pattern repetition. With pattern repetition, the optimization performs the analysis on all the ribs simultaneously, resulting in a single rib design which should theoretically satisfy the loading conditions for each rib. Further optimization included a free-sizing optimization in which the skin and spar thickness were optimized independently of the ribs. In this case, the skin and each spar were optimized simultaneously with respective volume fraction constraints and the same objective of minimizing weighted compliance.

### 3.9 Global Design

Ideally, a global three-dimensional optimization problem would provide the simplest carryover to a printable object. The global setup utilized the loading techniques discussed in Section 3.6. The design setup for global optimization is seen in Figure 32. The green volume is the design space and the shell skin is teal. Since there is not necessarily a need for spars to run laterally along the entire length of the wing, mounts (shown in red) were built at the mounting location seen on the baseline wing. In a similar manner, only the mounts and the edge of the skin were structurally constrained.

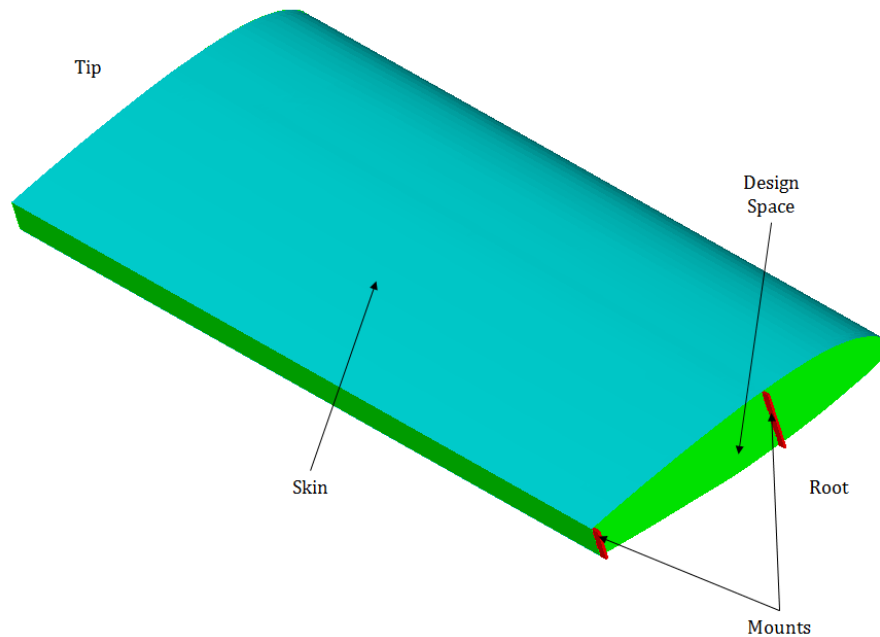


**Figure 32. 3D Global Optimization Problem Setup**

All global optimization models were built with an objective to minimize weighted compliance. This allowed for consideration of multiple loadsteps simultaneously. Generally, the design space was constrained to a set VF between 3 and 25 percent. In addition, a few of the models were constrained to total displacement and buckling. The specifics of the response constraints are discussed in Chapter 4 with experimental

results.

Along with the design shown in Figure 32, a problem setup with nondesign space ribs at the tip and the root were modeled. The ribs, along with a rear spar running the lateral length of the wing, were positioned to maintain the complete aerodynamic shape of the wing. As with the other 3D designs, there is not a main spar in the wing. Without these components, a TO design does not necessarily retain the shape. Low density elements below the chosen density threshold will not appear as structure. For simplicity, the ribs used for this analysis where adapted from the 2D optimized rib seen in Figure 44 and discussed in Section 3.8. This problem setup is seen in Figure 33.

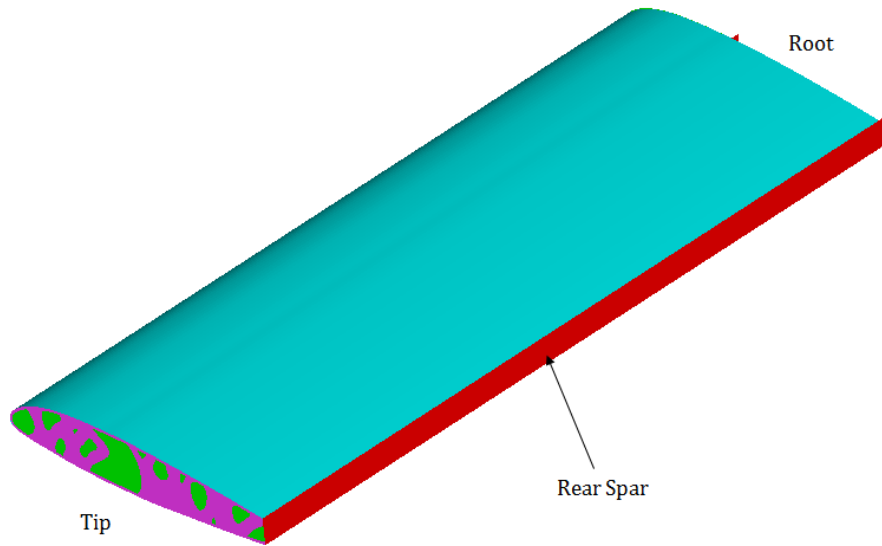


**Figure 33. 3D Global Optimization Problem With Tip Ribs and Rear Spar**

### 3.10 Component Integration

A key advantage to the additive manufacturing process, as discussed in Section 2.8, is the ability to integrate traditional independent components into a single part. For this research, the fuel tank of the aircraft was used as a subject for this test. In the baseline research, the fuel tank was disregarded for simplicity purposes. However,

a large component such as a fuel tank may have a significant impact on the structure. In Figure 77, the fuel tank is supported by additional spars and ribs along the leading edge of the wing [5]. The placement of the tank is most likely a factor of manufacturability, along with the desire to locate the weight as close to the center of gravity as possible. Once again, manufacturability is not a significant concern for an additive manufactured part. Therefore, redesign and placement of the fuel tank was desired.

A simple model of the baseline tank was built in Solidworks to estimate the total volume. Overall the wing tank had a volume of  $0.07 \text{ m}^3$  (18.5 *gallons*). Tank placement was desired as a location allowing it to support the structure in the best way possible without increasing the overall weight. Therefore, the results from Section 3.9 were the guideline for tank placement. Once placed, a complete analysis on the wing was setup in a similar manner to the baseline analysis in Section 3.7. A complete discussion of these results and associated tank placement is discussed in Chapter 4.

## IV. Results and Analysis

### 4.1 Initial Designs

As discussed in Section 3.5, the early optimizations consisted of a wing segment of the entire NACA 23015 airfoil. In all of the initial designs, loading was applied uniformly across the skin surface. Doing so disregarded any bending or torsional effects caused by displacement of the wing, and was thus not considered. Therefore, the initial design analysis does not truly represent actual loading conditions on the wing segment and a quality comparison to a baseline is subsequently difficult. However, these TO results provide insight into the 3D optimization and were an integral early step for this research. All of these early design models were built with an objective of minimizing compliance constrained by a set VF. The output from Optistruct for each TO consists of an image of the model with contoured density fractions for each element. Figure 34 is the output for a VF of 0.15.

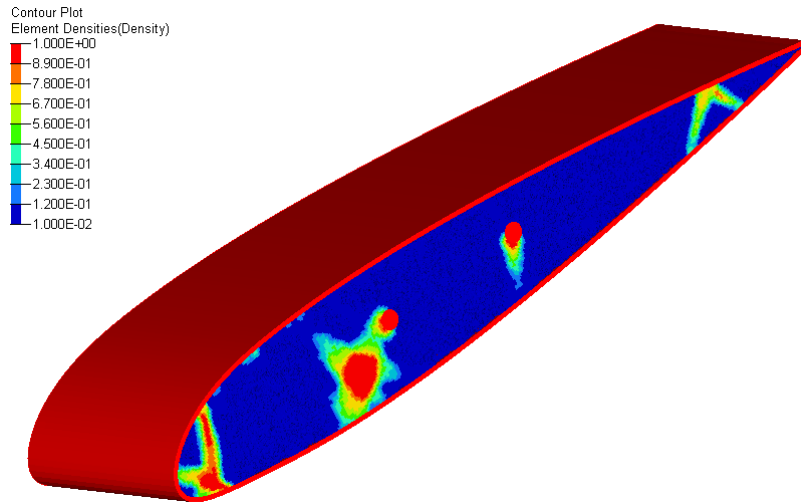


**Figure 34. Element Density for Initial Design Wing Segment TO for VF of 0.15**

In Figure 34, the blue elements have a density fraction of less than 0.12. The stiffness of the elements is linearly related to the density fraction, and therefore provides



relatively little structural support. Conversely, the red in each of these figures has a density fraction approaching 1.0. In the latter case, these elements are essential to structural support. A clearer image of the optimized results are shown in Figure 35, which are half-section views of Figure 34 along both the x-axis and y-axis.

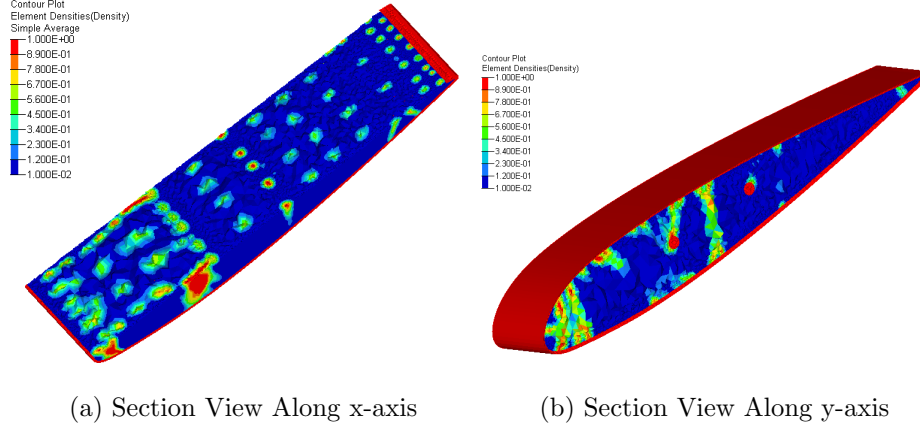


**Figure 35. Element Density for Section Views of TO Initial Design for VF of 0.15**

Since it is very difficult to manufacture a metallic variable density part, a threshold value was selected to remove low density material and drive higher density elements towards a density fraction of 1.0. For this case, a threshold of 0.40 was selected. This value was chosen through visual interpretation of the results as a value which provided full structural members without forfeiting excessive material volume. The post-processing toolkit OSSmooth was also used to create a usable CAD file. The Optistruct results with a set threshold value are seen in Figure 36a and the OSSmooth interpretation is seen in Figure 36b. In addition to steering the density fraction towards either 0 or 1, OSSmooth generates connections between incomplete members.

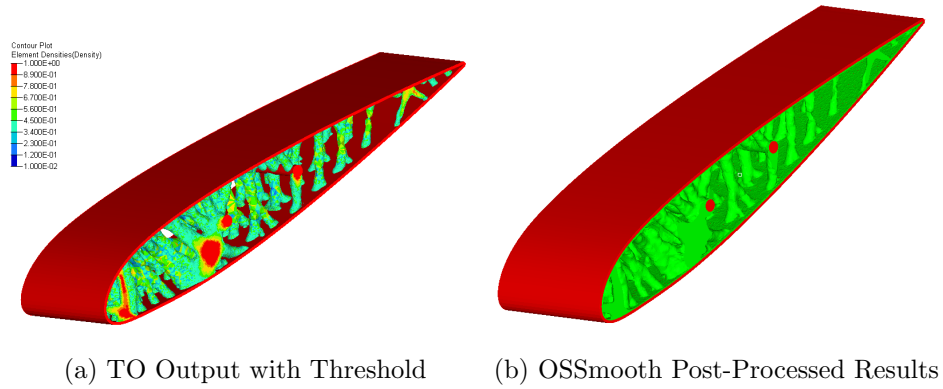


**Figure 36. Element Density for TO Interpreted Results of Initial Design with VF of 0.15 and Threshold of 0.40**

Overall, this TO results in significantly more material volume than the baseline wing. Though it is not aerodynamically and structurally competitive with the original design, it does show the capabilities of the TO process. Additional, a demonstration of the capabilities of AM are shown in Figure 37 with the manufacturing of this part. The development of this wing is also a growing process. A much improved methodology is discussed in the sections ahead.

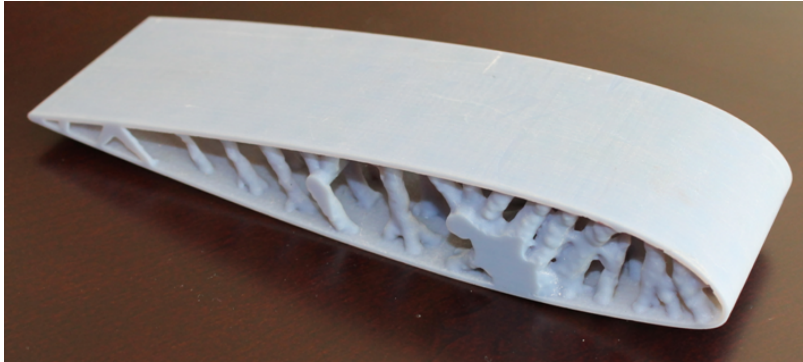


**Figure 37. Initial Design Manufactured Part with VF of 0.15 and Threshold of 0.40 Using a Photopolymer AM Technique**

## 4.2 Local Optimization

The local optimizations discussed in this chapter were built as a means to reduce the weight of a wing without significant deviation from traditional practices. Initially,

the TO focused solely on redesigning the baseline ribs. Wing ribs from modern day aircraft are somewhat optimized heuristically, though not mathematically. Rather, historical practices and tedious flight testing are used to reduce weight as much as possible. The examples discussed in this section explore various methodology to improve on current wing design theory and simplify the overall process of optimization. Further analysis on optimization considers material thickness distribution, primarily with the wing skin and spars. Manufacturing such parts with current fabrication processes is both expensive and difficult. However, the reduced manufacturing limitations from AM make this more reasonable. The designs covered in this section are not necessarily ideal for AM, but AM does streamline the manufacturing process. These designs also provide an excellent segue into enhanced aircraft designs which are truly optimized for ideal performance.

#### **4.2.1 Rib-Only Optimization.**

The rib only optimizations were conducted with a variety of conditions. In all scenarios, the ribs were laterally placed in the same location as the baseline wing. An optimization was performed once with each rib as an independent design space, and once with pattern repetition. Pattern repetition forces the optimizer to develop a single design during each iteration which is acceptable to support the constraints at each location. Following each optimization, an FEA provided displacement and stress for comparison to the baseline wing. Additionally, buckling is discussed in Section 4.2.4.

Overall, the local 2D shell optimizations provided feasible results. The outcomes were generally lighter with performance qualities as good as or better than the baseline design. The optimizations without and with pattern repetition are seen in Figures 38 and 41, respectively. Contours in these images are a function of element density,

from 0 to 1. The constraining VF for these models was selected through an iterative process by performing several optimizations and analyses to find an ideal value. When considering variable density problems, the ability to interpret the solution into a feasible design is an important consideration. This is the case with all 2D TO conducted in this research. Selecting the density ratio threshold creates a highly iterative process in selecting optimization values.

Intuitively, the rib designs are different when using pattern repetition. This is most notably the case at the rib closest to the root. At this location, the skin surrounding the rib is structurally constrained. In a mathematical sense, support at this location is not required under the established conditions. After post-processing, both of these models were reanalyzed for stress, displacement and buckling. Stress and displacement are shown below while buckling is discussed in Section 4.2.4. To generate an applicable FEA model, a density fraction threshold was set for each model. The threshold value was iteratively chosen through analysis and reevaluation to ensure a stress level less than the baseline maximum stress, if possible.

#### **4.2.1.1 TO Without Pattern Repetition.**

For the first model, the rib optimization without pattern repetition seen in Figure 38, a VF of 0.15 was selected. This value was iteratively chosen to obtain a feasible result. Lower values create less clear results which are more difficult to reanalyze through FEA. A higher VF created a design with excessive material. The same process was applied to other optimizations in this research. A mass and volume summary is located in Table 11. For comparison, the values of the baseline mass are listed at the end of the table.

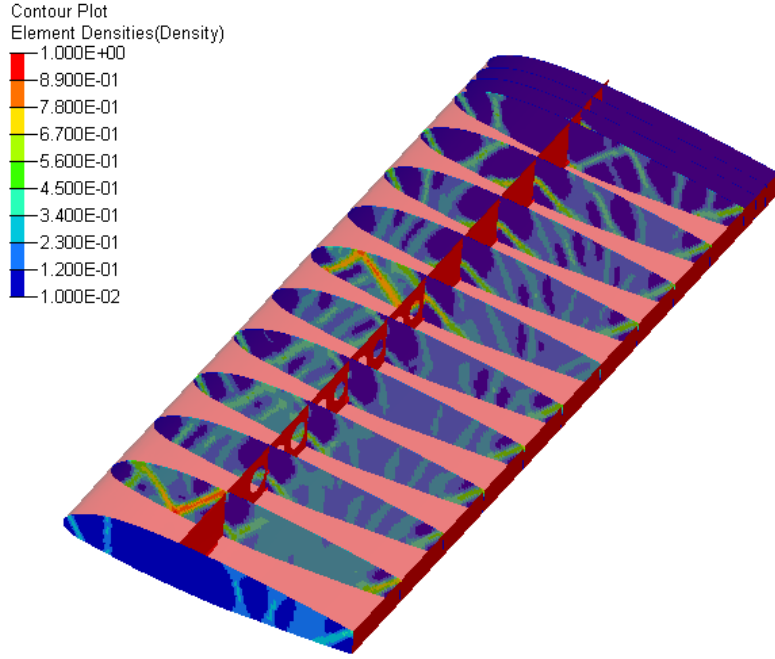


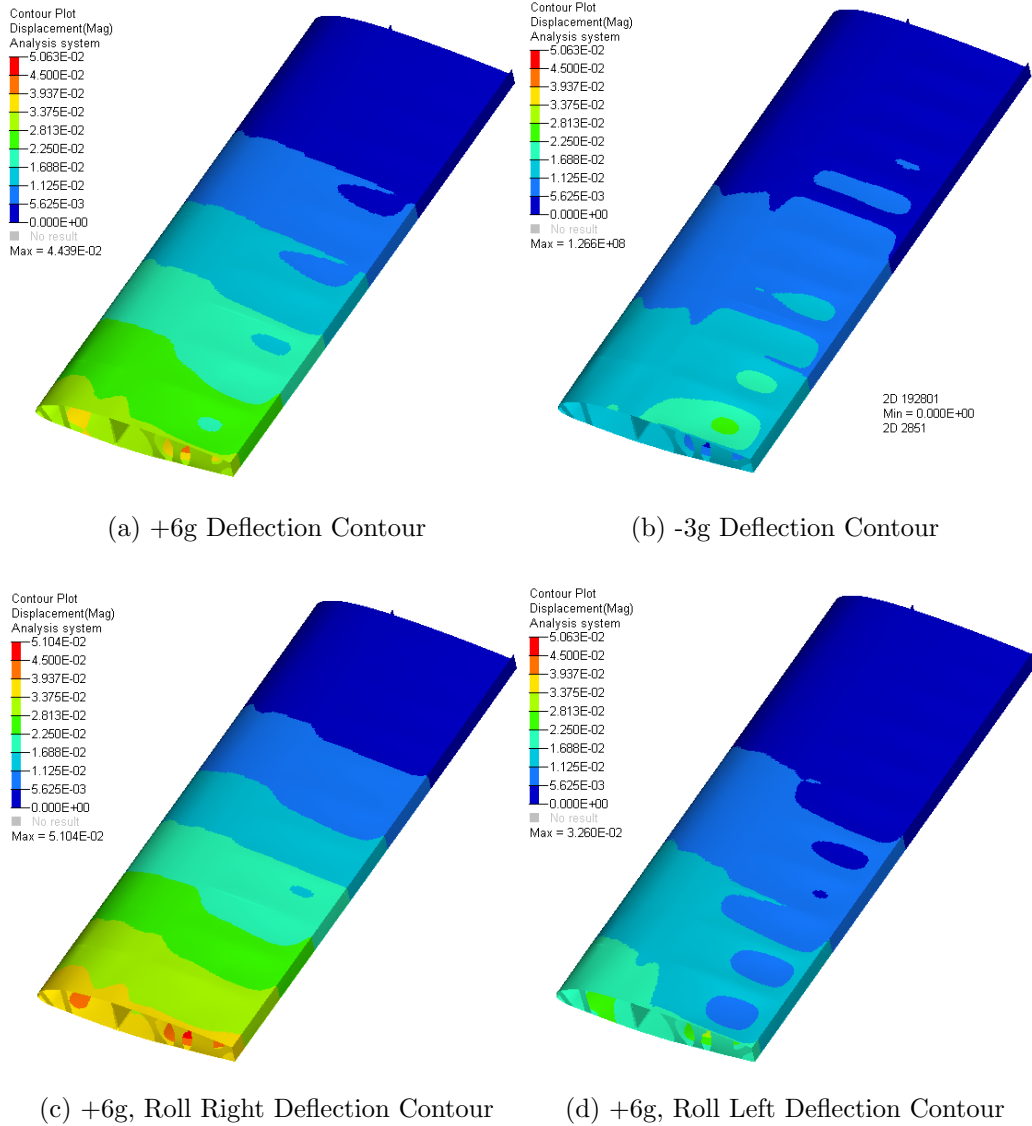
Figure 38. Element Density for 2D Rib Optimization Without Pattern Repetition

Table 11. Rib TO without Pattern Repetition Component Surface Area, Volume, and Mass Compared to Baseline Wing

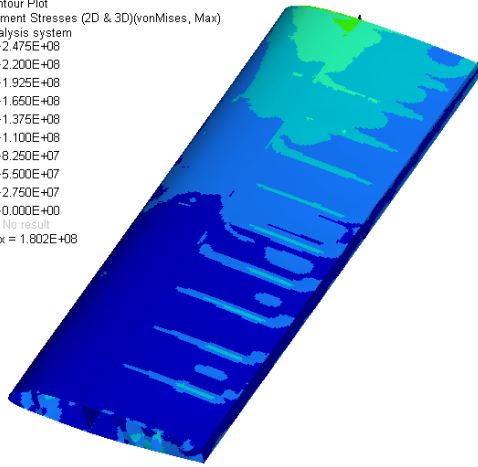
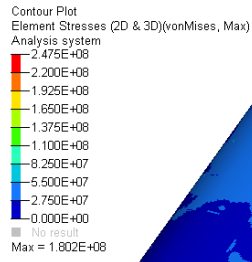
	Total Rib	Spars	Skin	Total
Surf Area ( $m^2$ )	1.379	0.790	6.479	8.648
Volume ( $m^3$ )	$1.10 \times 10^{-3}$	$0.80 \times 10^{-3}$	$5.23 \times 10^{-3}$	$7.13 \times 10^{-3}$
Mass ( $kg$ )	3.306	2.231	14.539	20.076
<i>Baseline Wing Mass (<math>kg</math>)</i>	<i>4.059</i>	<i>2.231</i>	<i>14.539</i>	<i>20.831</i>
<i>Savings From Baseline (%)</i>	<i>18.5</i>	<i>0</i>	<i>0</i>	<i>3.7</i>

The FEA results for this model are shown in Figure 39 and Figure 40 for displacement and stress, respectively. The results are further summarized in Table 12 with a comparison to the baseline wing. Since the ribs were the only design space for this optimization, changes in mass are only associated with the change in the individual rib. Overall, each rib was reduced on average in volume and mass by 18.5

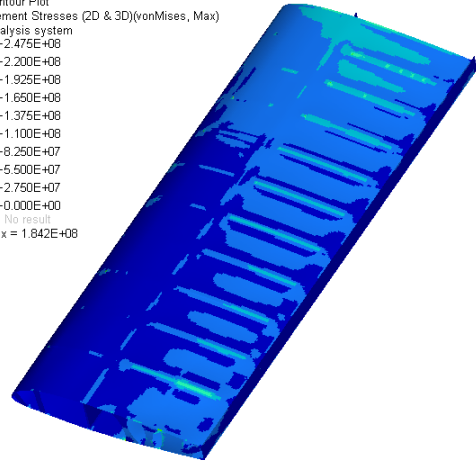
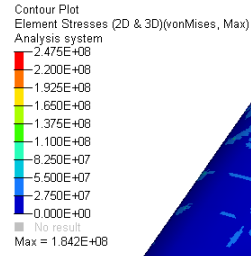
percent. Since the wing is completely constrained at the root, the rib at this location experiences very limited loading. If the rib is disregarded, there is a savings of 12.3 percent on average.



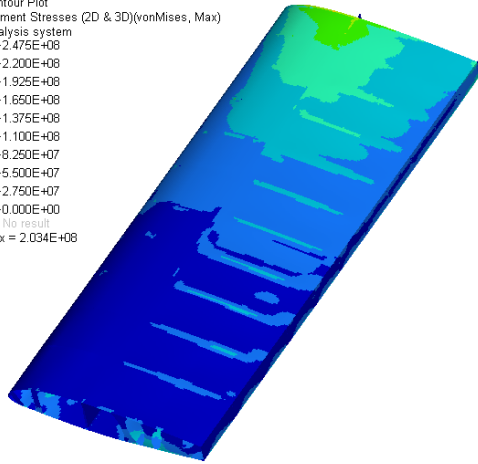
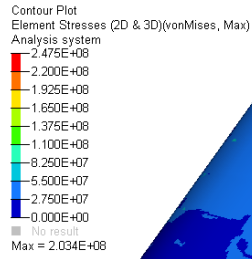
**Figure 39. Wing Deflection Contours for Each Flight Profile of Rib Optimized Wing without Pattern Repetition**



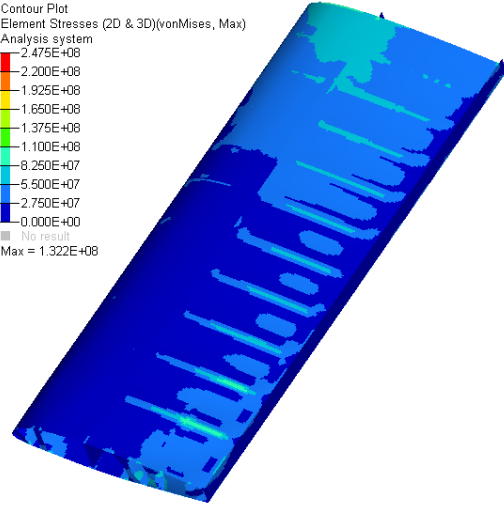
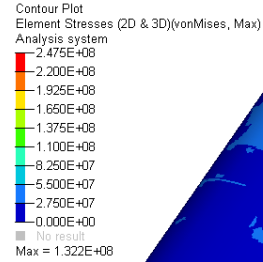
(a) +6g Stress Contour



(b) -3g Stress Contour



(c) +6g, Roll Right Stress Contour



(d) +6g, Roll Left Stress Contour

**Figure 40. Wing Stress Contours for Each Flight Profile of Rib Optimized Wing without Pattern Repetition**

**Table 12. Displacement and Stress of Rib Optimized Wing without Pattern Repetition Compared to Baseline Wing**

Condition	Total Displacement	Tip Displacement	von-Mises Stress
Local TO Without Pattern Repetition			
+6g	0.0444 m (1.75 in)	0.0345 m (1.36 in)	180.2 MPa (-3.7%)
-3g	0.0236 m (0.93 in)	0.0184 m (0.72 in)	126.6 MPa (+5.1%)
+6g, Roll Right	0.0510 m (2.01 in)	0.0397 m (1.56 in)	203.4 MPa (-2.2%)
+6g, Roll Left	0.0326 m (1.28 in)	0.0254 m (1.00 in)	132.2 MPa (+4.2%)
<i>Baseline Wing Analysis</i>			
<i>+6g</i>	<i>0.0425 m (1.67 in)</i>	<i>0.0338 m (1.33 in)</i>	<i>187.1 MPa</i>
<i>-3g</i>	<i>0.0211 m (0.83 in)</i>	<i>0.0167 m (0.66 in)</i>	<i>120.5 MPa</i>
<i>+6g, Roll Right</i>	<i>0.0492 m (1.93 in)</i>	<i>0.0390 m (1.54 in)</i>	<i>207.9 MPa</i>
<i>+6g, Roll Left</i>	<i>0.0313 m (1.23 in)</i>	<i>0.0225 m (0.89 in)</i>	<i>138.9 MPa</i>

For this optimization, total displacement remained close to the baseline analysis; increasing by less than 12 percent. Stresses generally decreased, but not by much. This analysis shows a reduction in mass, while von-Mises stress ranges between a decrease of 3.7 percent to an increase of 5.1 percent. Additional detail regarding the buckling analysis is discussed in Section 4.2.4.

#### **4.2.1.2 TO With Pattern Repetition.**

A slightly lower VF of 0.10 was used for the second model, with pattern repetition, in Figure 41. Changing the objective VF between the two analyses was accepted due to the realization the pattern repetition forced some of the ribs, mostly near the root, to have excessive material compared to what is most likely required. In other words, when using pattern repetition, each individual rib is constrained by the VF. Conversely, a model not using pattern repetition is only required to have an average



VF amongst all the ribs to meet the constraint. This is because the total rib area is used as the design space, rather than each individual rib required to have the same material volume.

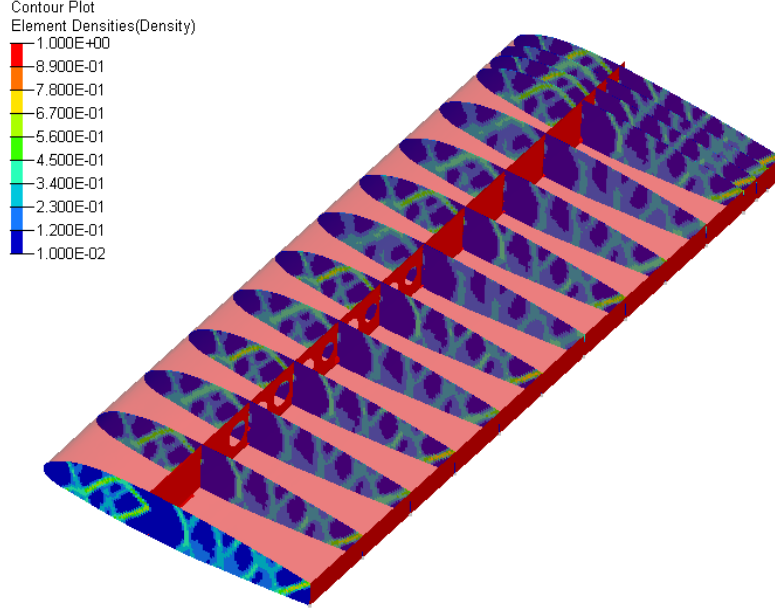


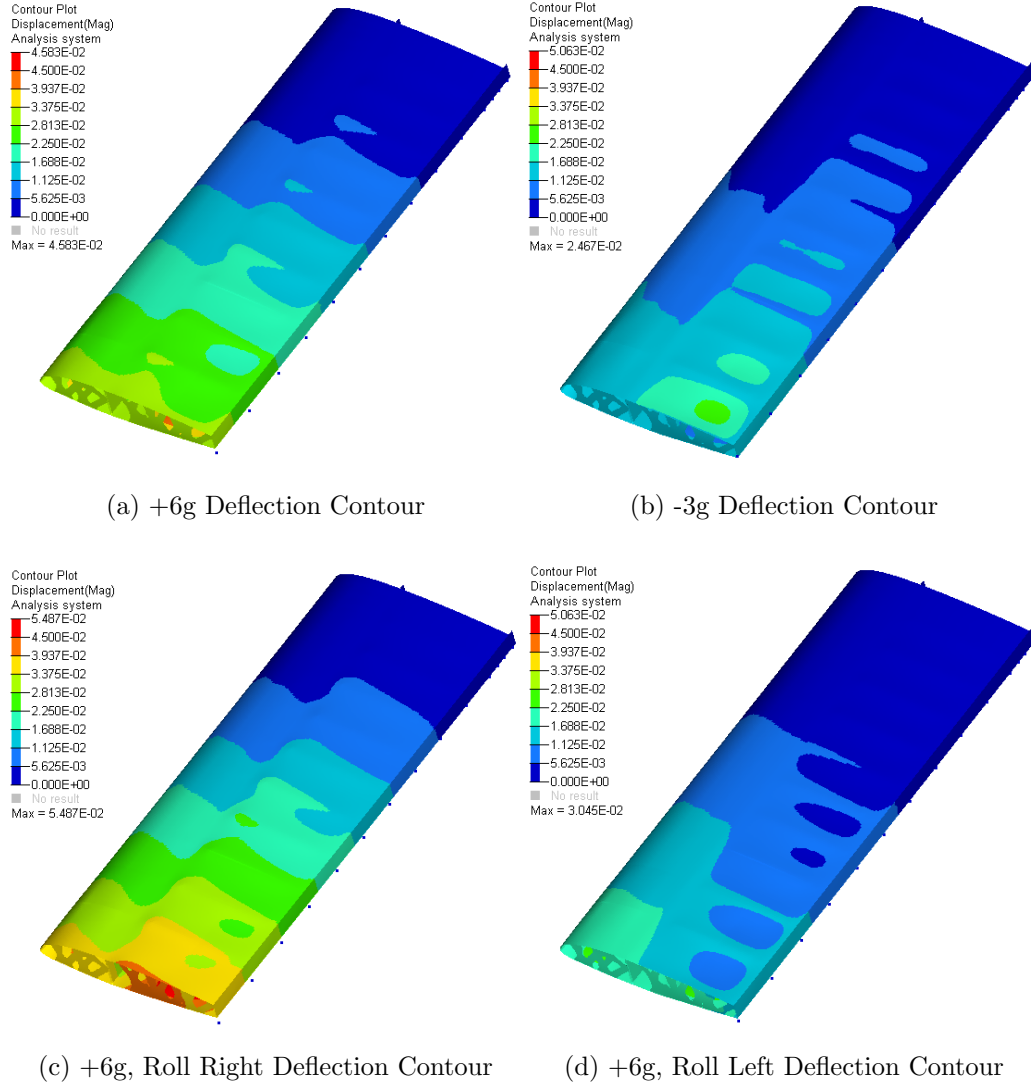
Figure 41. Element Density for 2D Rib Optimization With Pattern Repetition

Table 13. Rib TO with Pattern Repetition Component Surface Area, Volume, and Mass Compared to Baseline Wing

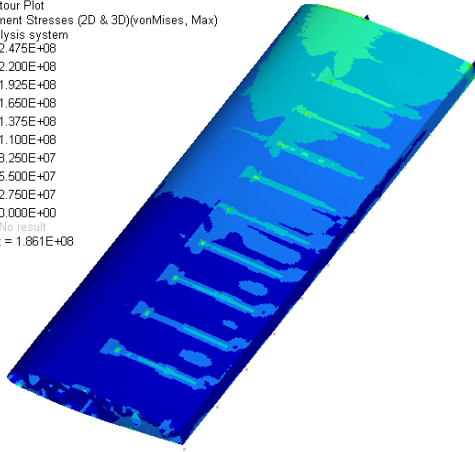
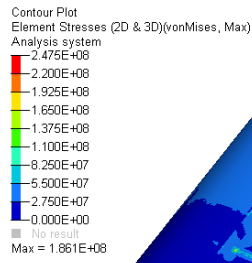
	Total Rib	Spars	Skin	Total
Surf Area ( $m^2$ )	1.582	0.790	6.479	8.730
Volume ( $m^3$ )	$1.29 \times 10^{-3}$	$0.80 \times 10^{-3}$	$5.23 \times 10^{-3}$	$7.36 \times 10^{-3}$
Mass ( $kg$ )	3.575	2.231	14.640	20.446
<i>Baseline Wing Mass (kg)</i>	<i>4.059</i>	<i>2.231</i>	<i>14.539</i>	<i>20.831</i>
<i>Savings From Baseline (%)</i>	<i>12.0</i>	<i>0</i>	<i>0</i>	<i>1.9</i>

In this case, the peak von-Mises stress of the optimized design did not meet the values seen in the baseline wing analysis. An increase in stress by up to 40.3 percent was seen. However, maximum stress remained less than the tensile yield

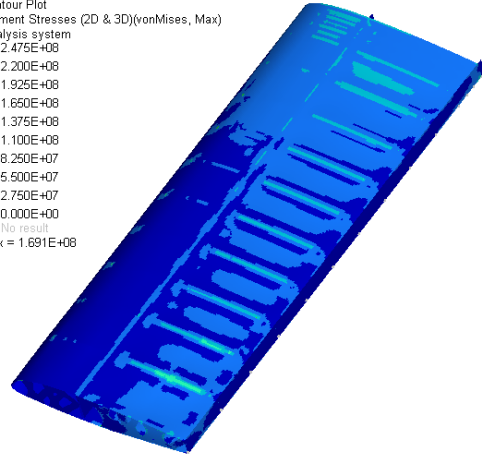
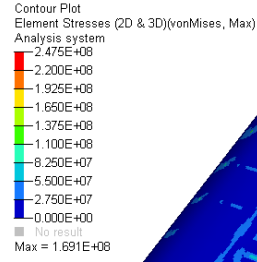
strength of the specified material, per Table 2, by 7.1 percent. A summary of mass and volume values is covered in Table 13. The displacement and stress contours are seen in Figure 42 and Figure 43, respectively. The results are summarized in Table 14. Overall, the rib mass was reduced by 12.0 percent. This value does show an improvement compared to the baseline wing, but once again, there are higher stress levels experienced.



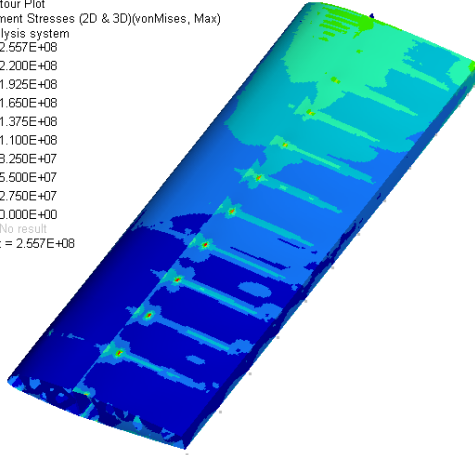
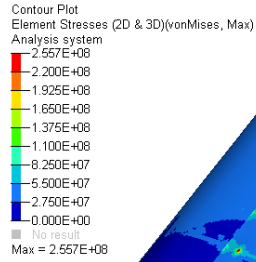
**Figure 42. Wing Deflection Contours for Each Flight Profile of Rib Optimized Wing with Pattern Repetition**



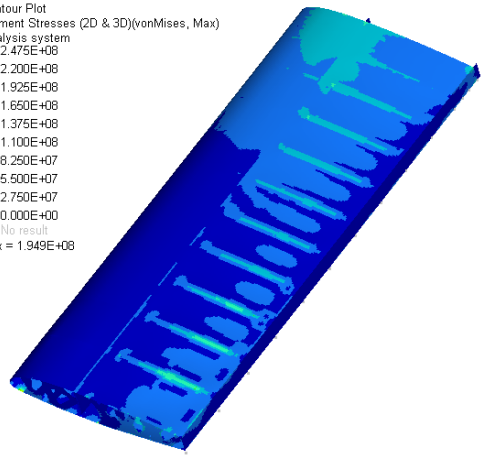
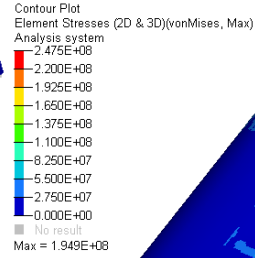
(a) +6g Stress Contour



(b) -3g Stress Contour



(c) +6g, Roll Right Stress Contour



(d) +6g, Roll Left Stress Contour

**Figure 43. Wing Stress Contours for Each Flight Profile of Rib Optimized Wing with Pattern Repetition**

**Table 14. Displacement and Stress of Rib Optimized Wing with Pattern Repetition Compared to Baseline Wing**

Condition	Total Displacement	Tip Displacement	von-Mises Stress
Local TO With Pattern Repetition			
+6g	0.0458 m (1.80 in)	0.0356 m (1.23 in)	186.1 MPa (-0.5%)
-3g	0.0247 m (0.74 in)	0.0165 m (0.66 in)	169.1 MPa (+40.3%)
+6g, Roll Right	0.0549 m (1.84 in)	0.0427 m (1.43 in)	255.7 MPa (+23.0%)
+6g, Roll Left	0.0305 m (1.14 in)	0.0203 m (0.80 in)	194.9 MPa (+40.3%)
<i>Baseline Wing Analysis</i>			
<i>+6g</i>	<i>0.0425 m (1.67 in)</i>	<i>0.0338 m (1.33 in)</i>	<i>187.1 MPa</i>
<i>-3g</i>	<i>0.0211 m (0.831 in)</i>	<i>0.0167 m (0.66 in)</i>	<i>120.5 MPa</i>
<i>+6g, Roll Right</i>	<i>0.0492 m (1.93 in)</i>	<i>0.0390 m (1.54 in)</i>	<i>207.9 MPa</i>
<i>+6g, Roll Left</i>	<i>0.0313 m (1.23 in)</i>	<i>0.0225 m (0.89 in)</i>	<i>138.9 MPa</i>

Both of the above optimizations provide an alternative approach to the traditional design. Through investigation of the displacement and stress contours in Figures 39, 40, 42, and 43, it is easy to see the similarities with the baseline analysis; both the displacement and stress contours show relatively similar distribution. This shows the optimized designs generally did not significantly hinder wing performance. However, localized stresses were as much as 40 percent higher for the wing optimized with pattern repetition compared to the baseline wing. This occurred at joints with sharp edges between some of the ribs and the skin. This is possibly attributed to a course mesh size near the sharp corners. Stress significantly lowers on adjoining elements, signifying this is at least partially a discrepancy with FEA. Additionally, a manufacturable 3D design would have smoother transitions reducing this impact further. An example of a more realistic design is seen in the following section, where the pattern repetition design is used to recreate an individual rib.

#### 4.2.1.3 Individual Redesigned Rib.

A redesigned rib was made as a way to directly compare an optimized design to the baseline rib. This was done through adaptation of the pattern repetition rib. Adding the thin material region around the exterior of the rib also reduced the peak stresses found in adjoining areas between the rib and skin. This redesigned rib was also made as a way to verify the advantages of skin and spar sizing optimization, discussed in following sections.

This rib is a direct interpretation of the design found with the local optimization with pattern repetition. Since the entire area for each rib was considered a design space, a thin area of material was applied around the exterior of the rib to maintain the desired aerodynamic shape of the airfoil. This is not necessarily required for a part built through additive manufacturing which is fabricated as a single part. However, it creates a better direct comparison to the baseline. Applying this material region around the rib also alleviated some peak stress areas found during the direct optimization. The redesigned rib is shown in Figure 44. Overall, the redesigned rib is 9.8 percent lighter than the baseline rib. The overall mass and volume is shown in Table 15 with a mass comparison to the baseline wing.

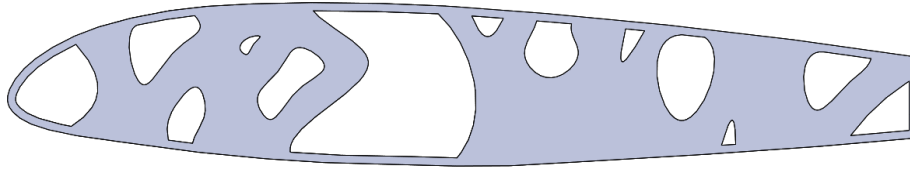


**Figure 44. TO Design Rib from Local Optimization with Pattern Repetition**

**Table 15. Redesigned TO Rib Surface Area, Volume, and Mass Compared to Baseline Wing**

	Total Rib	Spars	Skin	Total
Surf Area ( $m^2$ )	1.627	0.790	6.479	8.896
Volume ( $m^3$ )	$1.32 \times 10^{-3}$	$0.80 \times 10^{-3}$	$5.23 \times 10^{-3}$	$7.39 \times 10^{-3}$
Mass ( $kg$ )	3.677	2.231	14.640	20.548
<i>Baseline Wing Mass (<math>kg</math>)</i>	<i>4.059</i>	<i>2.231</i>	<i>14.539</i>	<i>20.831</i>
<i>Savings From Baseline (%)</i>	<i>9.5</i>	<i>0</i>	<i>0</i>	<i>1.4</i>

A comparison of the new TO rib to the original baseline rib is shown in Figure 45. The new rib is colored green where the baseline rib is blue. The TO rib is nearly identical to the pattern optimization rib, with the exception of the material region surrounding the exterior of the design. The original design relies heavily on circular holes along the centerline of the rib whereas the optimized design has more material on the bottom with voids primarily on the top and center of the rib. This is potentially a result of several different conditions. First, the original rib was not necessarily applied with the same loading conditions. The simple hole location and size throughout the chordwise centerline of the rib were likely chosen as an initial guess based on historic performance. Structural testing likely resulted in modifications of earlier designs to get the shape shown here. Another consideration for the difference is the simplicity of manufacturing. This rib, which is only marginally heavier than the optimized design in regard to the mass of the entire aircraft is very simple to make. The designers likely considered this rib as a component of the entire wing in which to provide adequate support without being significantly heavy.

The TO rib was also reintegrated back into the baseline model for analysis. Figure 46 is the deflection contour and Figure 47 is the stress contour for the wing with the new rib. Results are summarized in Table 16. The baseline wing results are included

for comparison.

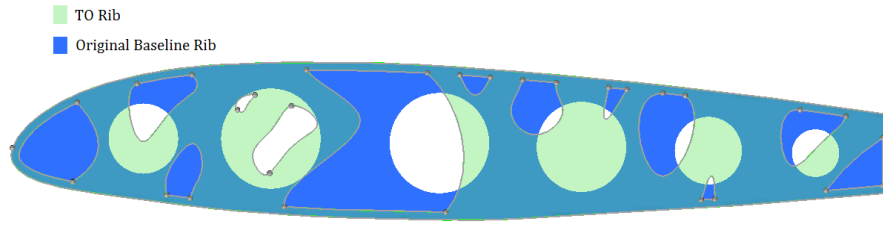


**Figure 45. Shape Comparison Between Baseline Rib and TO Rib**

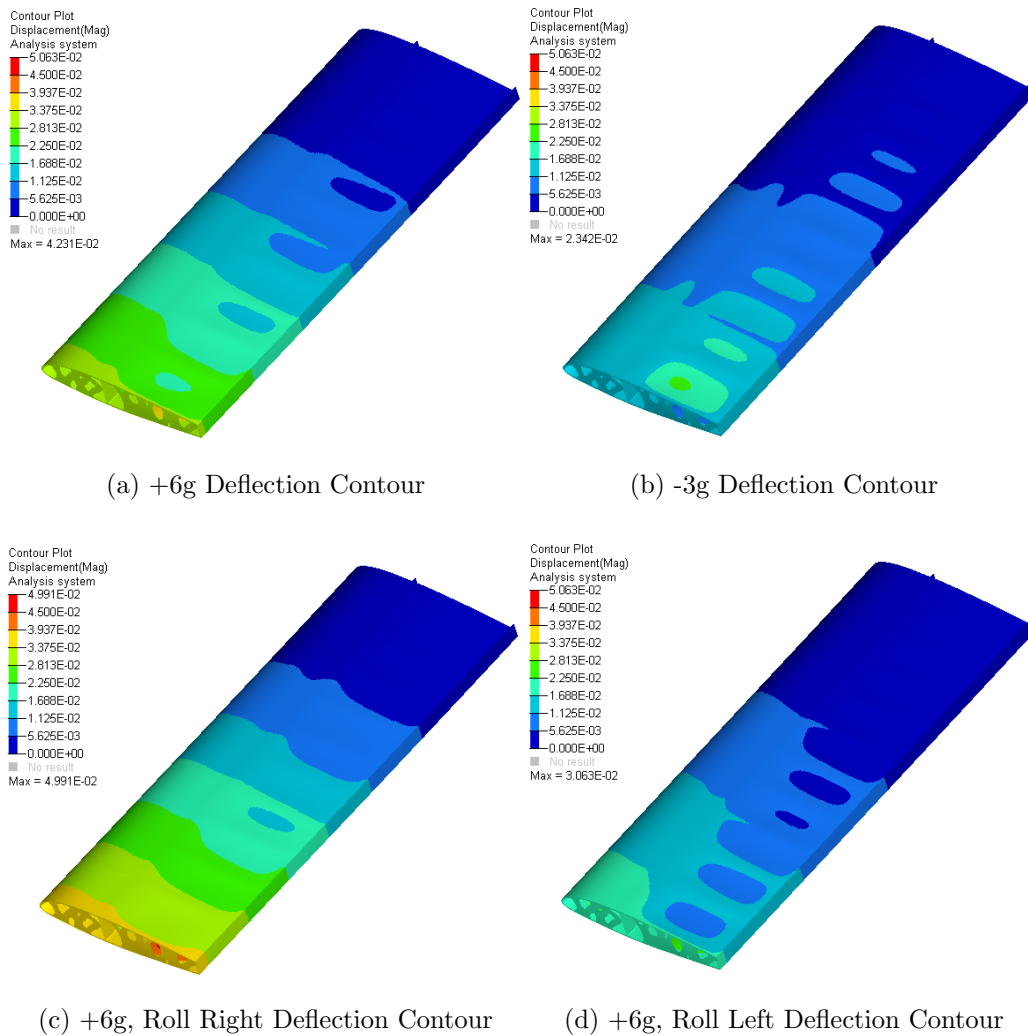
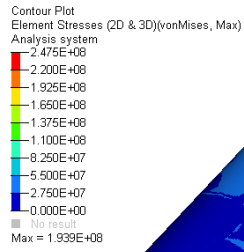
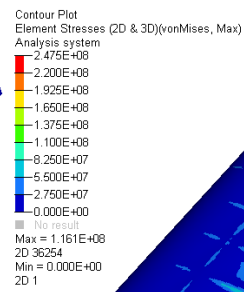


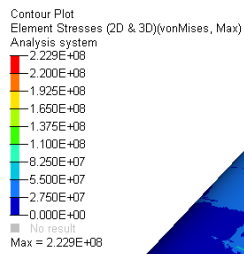
**Figure 46. Wing Deflection Contours for Each Flight Profile of Wing Integrated with TO Rib**



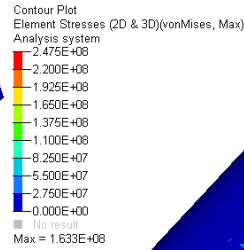
(a) +6g Stress Contour



(b) -3g Stress Contour



(c) +6g, Roll Right Stress Contour



(d) +6g, Roll Left Stress Contour

**Figure 47. Wing Stress Contours for Each Flight Profile of Wing Integrated with TO Rib**



**Table 16. Displacement and Stress of Wing with Integrated TO Rib Compared to Baseline Wing**

Condition	Total Displacement	Tip Displacement	von-Mises Stress
Individual Redesigned Rib			
+6g	0.0431 m (1.67 in)	0.0329 m (1.30 in)	193.9 MPa (+3.4%)
-3g	0.0234 m (0.92 in)	0.0156 m (0.61 in)	116.1 MPa (-3.6%)
+6g, Roll Right	0.0499 m (1.96 in)	0.0388 m (1.53 in)	222.9 MPa (+7.2%)
+6g, Roll Left	0.0306 m (1.20 in)	.0204 m (0.80 in)	163.3 MPa (+17.6%)
<i>Baseline Wing Analysis</i>			
<i>+6g</i>	<i>0.0425 m (1.67 in)</i>	<i>0.0338 m (1.33 in)</i>	<i>187.1 MPa</i>
<i>-3g</i>	<i>0.0211 m (0.831 in)</i>	<i>0.0167 m (0.66 in)</i>	<i>120.5 MPa</i>
<i>+6g, Roll Right</i>	<i>0.0492 m (1.93 in)</i>	<i>0.0390 m (1.54 in)</i>	<i>207.9 MPa</i>
<i>+6g, Roll Left</i>	<i>0.0313 m (1.23 in)</i>	<i>0.0225 m (0.89 in)</i>	<i>138.9 MPa</i>

Displacement and stress for this TO rib are similar when compared to the baseline wing. Overall displacement improved, but only marginally. This is a result of the ribs having little to do with lateral displacement. For each flight profile, peak von-Mises stress is within 17.2 percent of the baseline wing. However, stress levels at the peak loading condition is 7.2 percent over the baseline.

#### **4.2.2 Interpreted Design vs. TO Displacement and Stress.**

During the TO process in Optistruct, an FEA is conducted on the final iteration of the optimization. This analysis is somewhat misleading compared to a post-processed model since each element has a variable density. The stiffness of each element is linearly related to the density fraction of the element, which can cause structural performance which is unrealistic. It was therefore not a focus for this research when analyzing the feasibility of each design. However, a comparison of these displacement

and stress results to the post-processed FEA provides a validation of how reliable the initial variable density analysis is. A summary of results is shown in Table 17. The percentage difference of the TO analysis when compared to the post-processed FEA is shown in parenthesis for total displacement and von-Mises stress.

**Table 17. Displacement and Stress Comparison from TO Output of Rib Optimized Wing without Pattern Repetition with Percent Change Relative to the Post-Processed Results**

Condition	Total Displacement	Tip Displacement	von-Mises Stress
+6g	0.0491 m (1.93 in) (+10.5%)	0.0382 m (1.50 in)	179.0 <i>MPa</i> (-0.7%)
-3g	0.0265 m (1.04 in) (+12.3%)	0.0206 m (0.81 in)	181.1 <i>MPa</i> (-1.7%)
+6g, Roll Right	0.0576 m (2.27 in) (+12.9%)	0.0448 m (1.76 in)	207.1 <i>MPa</i> (+1.8%)
+6g, Roll Left	0.0344 m (1.35 in) (+5.5%)	0.0268 m (1.06 in)	143.5 <i>MPa</i> (+8.5%)

Displacement error is within 12.9 percent and stress error is within 8.5 percent. This is most likely a result of the higher density elements, supporting most of the load, with reduced stiffness. The lower density elements which do not exist in the post-processed model only minimally enhance structural integrity. The only significant outlier was for the +6g, roll left flight profile. In this case, a few high stress elements are concentrated on the wing skin near one of the inboard ribs. The low density fraction elements near this region do not support the skin as well as the fully dense, post-processed design. However, there is generally a very close relation for the two. For these particular loading conditions.

### 4.2.3 Spar and Skin Optimization.

The redesigned rib in Figure 44 was used for a wing spar and skin optimization. In this case, the rib was simply reapplied back into the baseline wing. The problem setup is seen in Section 4.2.1.3. In this setup, both spars and the wing skin are set as a design space. Since the spars were used as design space, the holes from the original

design were removed. The ratio between the original baseline spar volume and the design space spar with the holes removed was used as the initial VF for optimization.

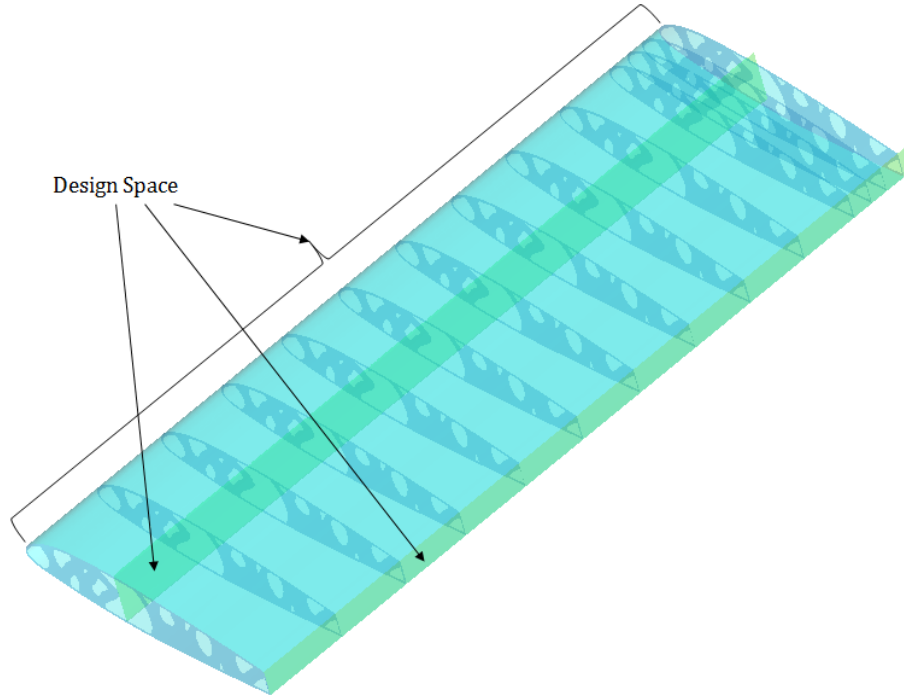


**Figure 48. 2D Spar and Skin Free Sizing Optimization Problem Setup**

A TO for the main spar was initially conducted with the expectation of similar results to the ribs, with hole locations identified through low elemental density fractions. However, the TO resulted in a transition from high density material at the root of the spar to low density at the tip. This did not provide an easy interpretation to a realistic design. Therefore, a free-sizing optimization was applied to the spar. A free-sizing optimization works in a similar manner to TO without variable density. Rather, element thickness is a variable with set bounds [9]. This was done for an easier interpretation of the results and application to AM. Concurrently, the skin thickness was also optimized. With free-sizing, there is a direct correlation between volume fraction constraints and final design, not necessarily the case with variable density TO results. Therefore, the mass and volume values for this model is in-line

with the values for the model shown in Figure 44. Another advantage of performing a sizing optimization is the ability to use von-Mises stress as design constraints. This is because each material element changes in thickness, not in density. Doing so increases the likelihood of a result satisfying the desired outcome.

The spar and skin optimization results are seen in Figure 49. The optimization for all three design spaces were constrained in volume to the baseline measurements. The range of material thickness was set to fluctuate between 0.635 mm to 2.500 mm. The minimum thickness limit is the thinnest value aluminum sheet metal found on the RV-4 aircraft. The upper limit was set at approximately four times the thickness of the minimum value. Using these values, the spar thickness VF constraint was set to 0.368 for the main spar, 0.406 for the back spar, and 0.329 for the skin. The objective to minimize weighted compliance for each load condition was consistent with other optimizations conducted in this research. The results are seen in Figure 49. Contour thickness is in meters. These redesigned spars retain the same mass as the baseline wing, but decrease overall displacement and stress. Displacement and stress results from the optimization are shown in Figure 50 and 51, respectively. The results for displacement and peak stress are also summarized in Table 18. The original baseline wing results are also shown in the table.

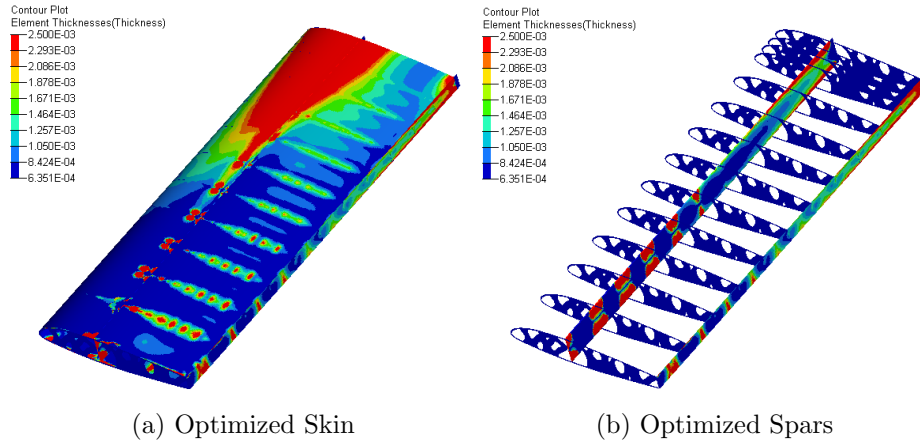


Figure 49. Local TO Results for Spar and Skin Free-Sizing Optimization of Local Wing Design

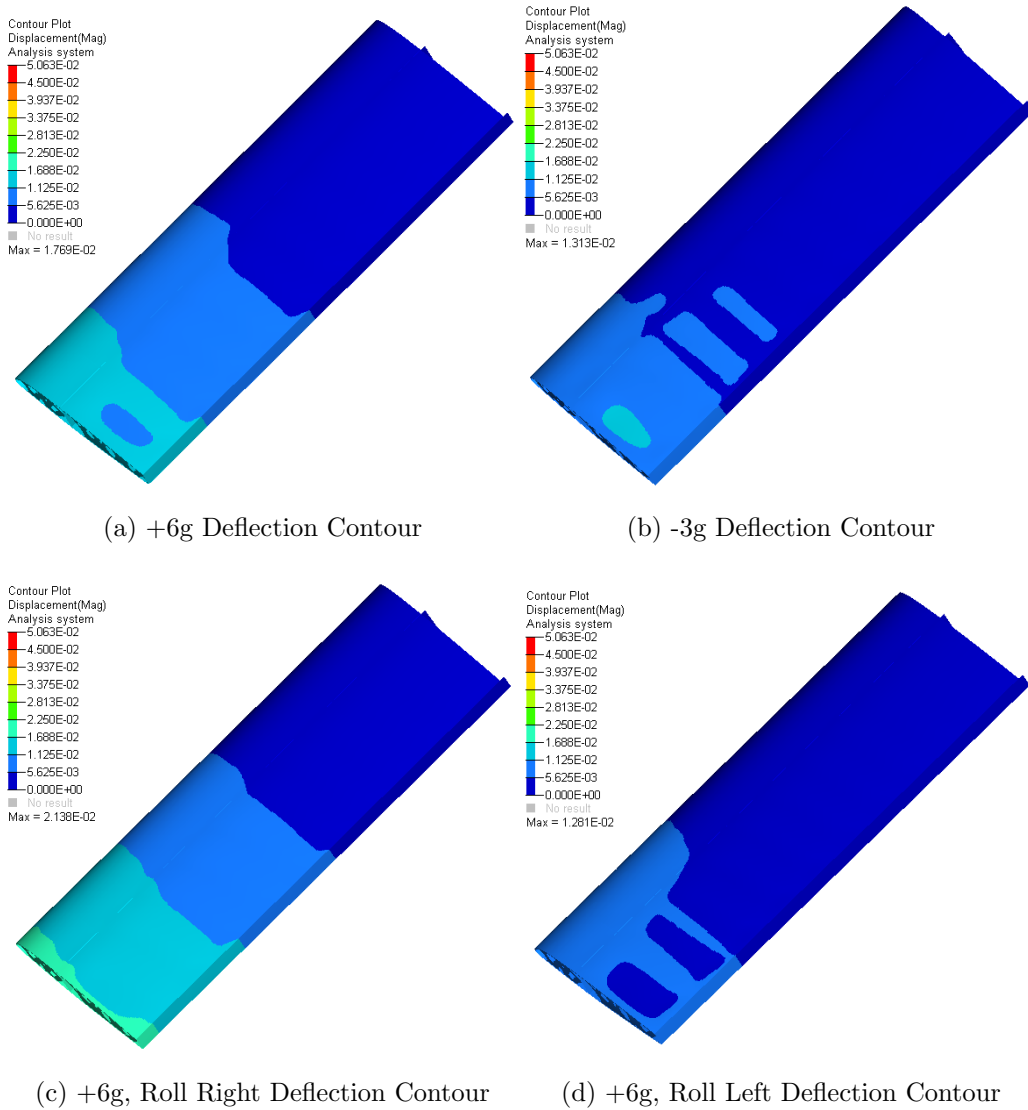
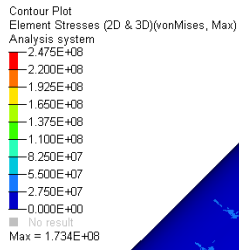
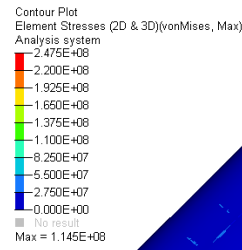


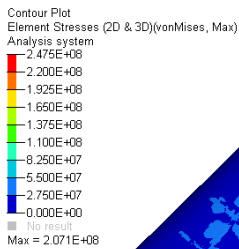
Figure 50. Wing Deflection Contours for Each Flight Profile of Wing with TO Ribs and Sizing Optimized Spars and Skin



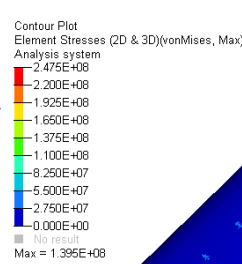
(a) +6g Stress Contour



(b) -3g Stress Contour



(c) +6g, Roll Right Stress Contour



(d) +6g, Roll Left Stress Contour

**Figure 51. Wing Stress Contours for Each Flight Profile of Wing with TO Ribs and Sizing Optimized Spars and Skin**

**Table 18. Displacement and Stress of Wing with TO Ribs and Sizing Optimized Spars and Skin Compared to the Baseline Wing**

Condition	Total Displacement	von-Mises Stress
Redesigned Rib with Spar and Skin Sizing Optimization		
+6g	0.0177 m (0.70 in)	173.4 MPa (-7.3%)
-3g	0.0131 m (0.51 in)	114.5 MPa (-5.0%)
+6g, Roll Right	0.0214 m (0.84 in)	207.1 MPa (-0.4%)
+6g, Roll Left	0.0128 m (0.50 in)	139.5 MPa (+0.4%)
<i>Baseline Wing Analysis</i>		
+6g	0.0425 m (1.67 in)	187.1 MPa
-3g	0.0211 m (0.83 in)	120.5 MPa
+6g, Roll Right	0.0492 m (1.93 in)	207.9 MPa
+6g, Roll Left	0.0313 m (1.23 in)	138.9 MPa

When compared to the baseline wing, stress levels remained relatively the same. Peak stress levels still occur at the root of the spar. However, the universal von-Mises stress is generally lower and more evenly distributed throughout the skin. This is especially noticeable when comparing Figure 51 to Figure 47. In addition, total displacement decreased by over 50 percent. The variable skin thickness also caused a decrease in deflection between the ribs, resulting in a more uniform global displacement. These results show a significant improvement compared to the baseline. However, fabrication is not very reasonable without AM. This is an excellent case showing TO as a technology enabler of AM. As AM technology advances, this design becomes more feasible. Further discussion on this topic is covered in Section 5.2.

#### 4.2.4 Buckling Comparative Analysis.

Even though none of these designs were optimized for buckling, a full analysis was conducted for comparative purposes. Constraining an optimization for buckling on a design like this is not very reasonable. The long wingspan results in a significant bending moment near the root which can result in elastic buckling conditions. The goal of performing a buckling analysis is to show buckling does not worsen with the optimizations. This analysis provides a means of comparison for the different designs. Once again, the BLF for each load condition is the most significant consideration when analyzing buckling.

The first buckling case examined is the rib optimization without pattern repetition. The buckling for the +6g, roll right maneuver is shown graphically in Figure 52. Only this flight profile is shown since it has the most severe loading conditions. The resulting BLF values from the post-processed FEA are listed in Table 19. For comparative purposes, the baseline BLF values are provided as well. Similar to the baseline model, only the first three modes of buckling were examined.

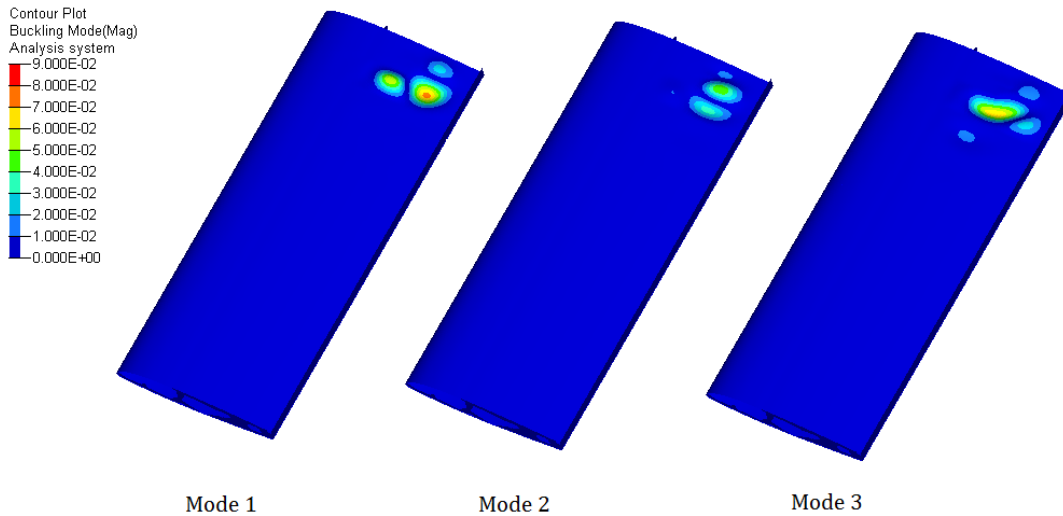


**Figure 52. Buckling Analysis for +6g, Rolling Right Maneuver for Rib Optimized Wing without Pattern Repetition**



**Table 19. Buckling Load Factor of Rib Optimized Wing without Pattern Repetition Compared to Baseline Wing**

	Buckling Load Factor			<i>Baseline Values</i>		
Condition	Mode 1	Mode 2	Mode 3	<i>Mode 1</i>	<i>Mode 2</i>	<i>Mode 3</i>
+6g	0.091	0.097	0.103	<i>0.095</i>	<i>0.102</i>	<i>0.106</i>
-3g	0.141	0.144	0.181	<i>0.104</i>	<i>0.129</i>	<i>0.153</i>
+6g, Roll Right	0.079	0.083	0.088	<i>0.081</i>	<i>0.086</i>	<i>0.089</i>
+6g, Roll Left	0.130	0.140	0.154	<i>0.143</i>	<i>0.155</i>	<i>0.165</i>

For this case, the BLF values are generally similar when compared to the baseline analysis. This is expected since there was not an optimization performed on the skin or spars for this case. The skin thickness and spar resistance to deflection is highly related to skin buckling. The exception for similar BLF performance is with the -3g flight profile. This is possibly attributed to how the ribs support the skin. All positive g maneuvers have a BLF within a 10 percent error and the buckling occurs primarily at the top root of the wing. However, the negative flight profile buckles at the bottom root of the wing since tip deflection is down for negative g's. The higher BLF deviation is therefore most likely a result of how the ribs support the skin along the bottom of the wing. The TO created less rib support on the bottom of the wing near the root. Since the aircraft is in a descent for this condition, buckling occurs on the bottom of the wing. As discussed in the following paragraphs, BLF is not necessarily higher for other TO designs, depending on how the skin is supported at the respective locations along the wing.

A full buckling analysis was also conducted for the rib optimization with pattern repetition. The buckling for the +6g, roll right maneuver is shown graphically in Figure 53. The resulting BLF values are listed in Table 20, along with the baseline values. In this case, all of the ribs are the same shape.

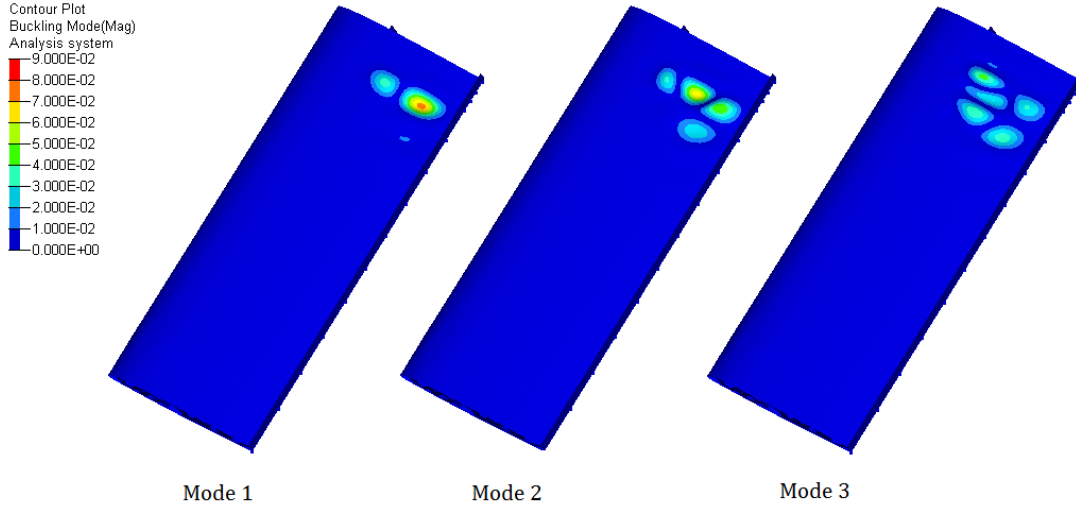


**Figure 53. Buckling Analysis for +6g, Rolling Right Maneuver for Rib Optimized Wing with Pattern Repetition**

**Table 20. Buckling Load Factor of Rib Optimized Wing without Pattern Repetition Compared to Baseline Wing**

Condition	Buckling Load Factor			<i>Baseline Values</i>		
	Mode 1	Mode 2	Mode 3	<i>Mode 1</i>	<i>Mode 2</i>	<i>Mode 3</i>
+6g	0.099	0.107	0.112	<i>0.095</i>	<i>0.102</i>	<i>0.106</i>
-3g	0.110	0.134	0.161	<i>0.104</i>	<i>0.129</i>	<i>0.153</i>
+6g, Roll Right	0.082	0.089	0.094	<i>0.081</i>	<i>0.086</i>	<i>0.089</i>
+6g, Roll Left	0.155	0.161	0.174	<i>0.143</i>	<i>0.155</i>	<i>0.165</i>

For this wing, the BLF values are similar for each unique loading condition. The maximum deviation is within 12 percent error. Similar to the rib optimization without pattern repetition, lower BLF values are attributed to how the ribs support the skin near the root of the wing. This design therefore performs better in regards to buckling than the optimization without pattern repetition.

A buckling analysis was also applied to the wing with the optimized rib reintegrated into the model. The +6g, roll right maneuver buckling is shown graphically

in Figure 54 and the BLF values are in Table 21.

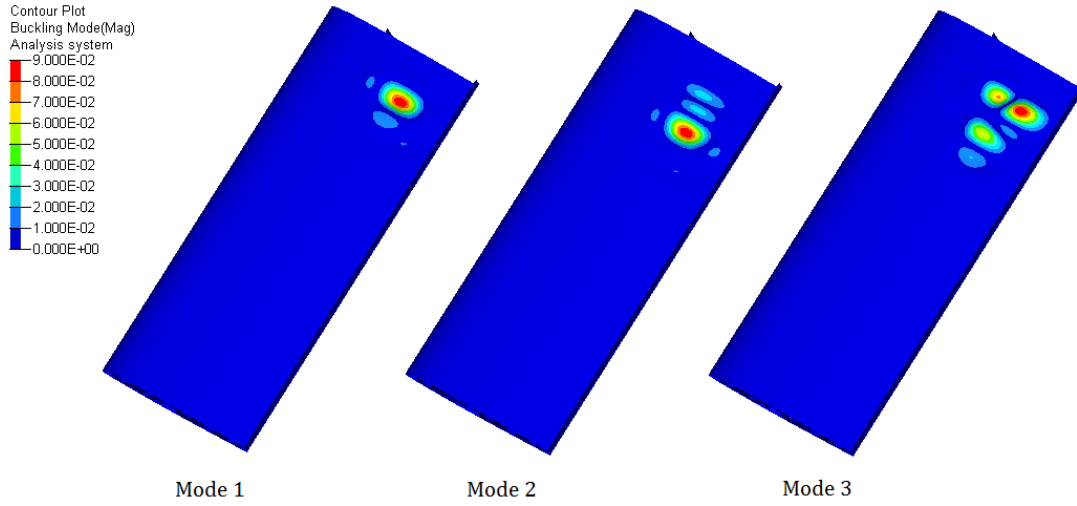


**Figure 54. Buckling Analysis for +6g, Rolling Right Maneuver for Wing Integrated with TO Optimized Rib**

**Table 21. Buckling Load Factor of Wing Integrated with TO Rib Compared to Baseline Wing**

	Buckling Load Factor			<i>Baseline Values</i>		
Condition	Mode 1	Mode 2	Mode 3	<i>Mode 1</i>	<i>Mode 2</i>	<i>Mode 3</i>
+6g	0.088	0.096	0.105	<i>0.095</i>	<i>0.102</i>	<i>0.106</i>
-3g	0.108	0.132	0.155	<i>0.104</i>	<i>0.129</i>	<i>0.153</i>
+6g, Roll Right	0.073	0.080	0.088	<i>0.081</i>	<i>0.086</i>	<i>0.089</i>
+6g, Roll Left	0.134	0.146	0.159	<i>0.143</i>	<i>0.155</i>	<i>0.165</i>

Once again, this wing performed similar to the baseline wing in regards to BLF and is generally within 10 percent for the various flight profiles. Similar to the discussion above, the most significant contribution to improving BLF in the aircraft skin is by reducing deflection. This is done with a stiffer skin or spar. Also note buckling occurred roughly at the same location for all three of the above optimizations. Since the loading conditions are the same for all three and they each have the same spars

and ribs this is an expected result.

The final buckling analysis performed for this section is for the skin and spar sizing optimization discussed in Section 4.2.3. The buckling for the +6g, rolling right maneuver is shown graphically in Figure 55. A summary of BLF values for this optimization is shown in Table 22. The baseline values are added for comparative purposes.

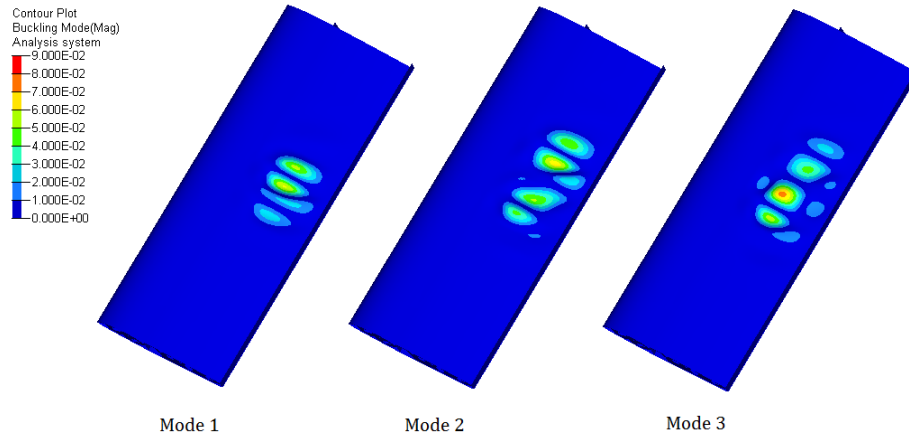


**Figure 55. Buckling Analysis for +6G, Rolling Right Maneuver for Wing with TO Ribs and Sizing Optimized Spars and Skin**

**Table 22. Buckling Load Factor of Wing with TO Ribs and Sizing Optimized Spars and Skin Compared to Baseline Wing**

	Buckling Load Factor			<i>Baseline Values</i>		
Condition	Mode 1	Mode 2	Mode 3	<i>Mode 1</i>	<i>Mode 2</i>	<i>Mode 3</i>
+6g	0.254	0.279	0.285	<i>0.095</i>	<i>0.102</i>	<i>0.106</i>
-3g	0.231	0.250	0.316	<i>0.104</i>	<i>0.129</i>	<i>0.153</i>
+6g, Roll Right	0.207	0.226	0.235	<i>0.081</i>	<i>0.086</i>	<i>0.089</i>
+6g, Roll Left	0.271	0.291	0.350	<i>0.143</i>	<i>0.155</i>	<i>0.165</i>

Buckling for the wing with the spar and skin sizing optimization was significantly different than from the baseline wing. BLF values were on the order of three times

greater than from previous analysis. The greater resistance to buckling in the skin did result in some buckling of the ribs, which was not seen in previous optimizations. Additionally, the skin buckling did not necessarily occur at the root for each of the various loads. Rather it was more evenly distributed near the middle of the wing laterally. The ability to apply a thickness optimization significantly improved the buckling performance of this wing. The ability to simply manufacture a traditionally 2D component with inconsistent thickness is a noticeable advantage for buckling performance.

As stated above, constraining an optimization to buckling proves difficult. A long slender wing placed under high loads will have some form of elastic buckling in the skin. If this wing was only placed under light loading conditions, constraining the design to zero buckling could prove more effective. This is also the case for an aircraft with shorter wings, less susceptible to deflection. Various wing designs for future analysis should consider buckling for optimization conditions on an individual basis.

#### **4.2.4.1 Local Design Conclusion.**

From all of these results, the TO without pattern repetition showed the most significant improvement over the baseline design when only considering rib redesign. This is somewhat intuitive, since each rib design space is not constrained to the performance of any other rib. Stress remained within approximately 5 percent and displacement within 12 percent. This design had a savings of mass of 3.7 percent from the baseline. Likewise, the BLF stayed roughly the same compared to the baseline wing, with the exception of small improvement in the -g region. The pattern repetition model did not perform as well. Stress levels increased for each maneuver except the straight climb. Wing displacement did, however, stay roughly the same.

Finally, individual rib redesign experienced both displacement and stress levels very similar to those in the baseline wing.

For AM purposes, pattern repetition is not necessary. However, simply applying a traditional rib and spar design is not ideal for AM regardless. The most likely usage of TO for an individual rib is a simple 2D rib design, such as the one in Figure 44. This case allows for more traditional means of manufacturing. Yet, difficulties in adapting a 3D global design still make the local rib optimization relevant. Continued optimizations to enhance performance are discussed in the following sections. The most drastic improvement was seen with the sizing optimization performed on the skin and spars. This design had a very noticeable reduction in average von-Mises stress and total displacement compared to previous optimizations. However, these optimizations did not result in any reduction in mass. To do so, an iterative reduction in VF followed by analysis would result in a lighter wing. This is a meaningful consideration for future study.

### 4.3 Global Optimization

Ideally, a global optimization provides a design most suitable to AM. This situation should take full advantage of the AM capabilities. However, there is difficulty in administering a good design. The initial attempts of a true global design space consisted of a simple design space surrounded by the shell skin illustrated in Figure 32. These optimizations were performed with a VF of 0.10. In the baseline wing, the VF of material with respect to the total wing volume accounts for approximately 2 percent of the total volume inside the wing. The minimum VF allowed by the Optistruct solver is 0.03. Several attempts of optimizing with this constraint resulted in generally poor results with extremely low density elements rather than decipherable members. Therefore, this value of 0.10 was used to allow for an easier interpretation

of the results. Unfortunately, an error within the Optistruct software does not allow for FEA analysis after post-processing. Further discussion on this problem is covered in Chapter 5.

Figure 56 is the first example of a global optimization. The design space for this problem was shown in Figure 32. The high density fraction areas are in red and primarily form an I-beam shape beginning at the root along the constrained mount. This is more apparent in Figure 57, which is a series of different orientations for this optimization at a density fraction threshold of 0.20. In all of these images, the skin is removed for easier viewing. Reference Figure 56 for contour color values. The I-beam shape is most likely a result of the simple static loading conditions applied on the wing. An I-beam shape is generally the ideal shape for bending loads. The extremely low density areas towards the tip of the wing suggest minimal support is required to support the skin.

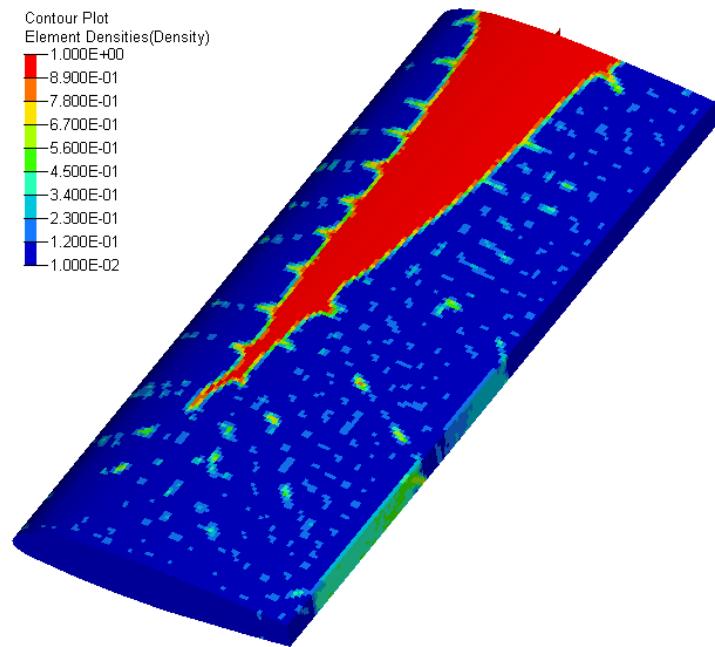


**Figure 56. Density Fraction Contour of Global Wing TO**

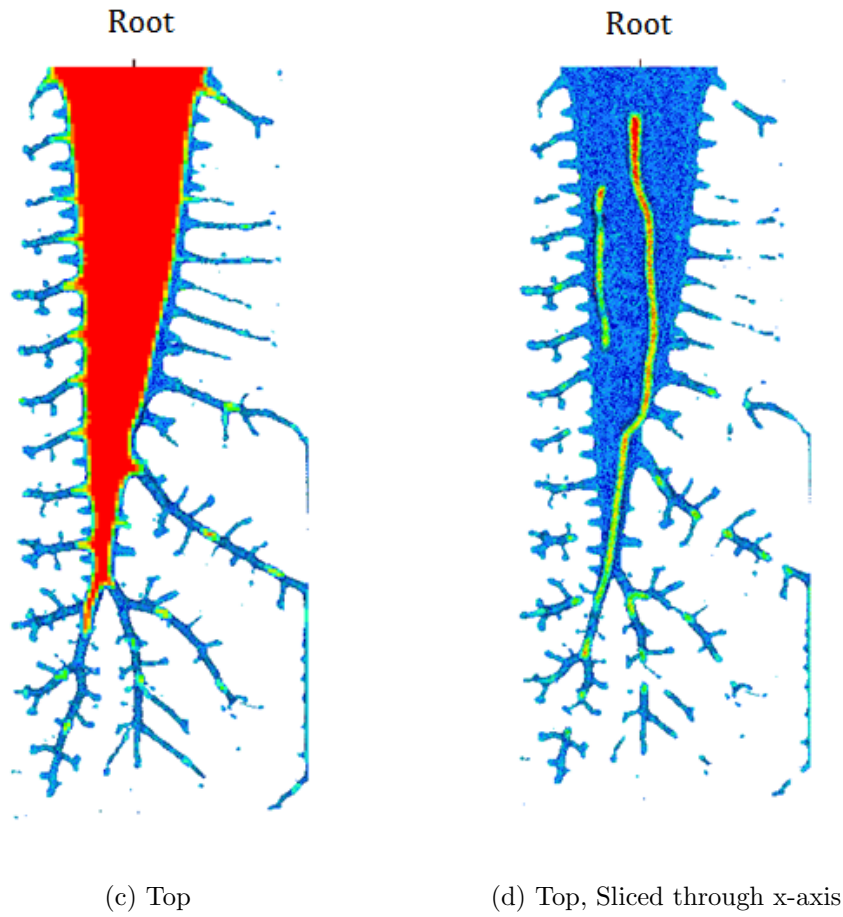
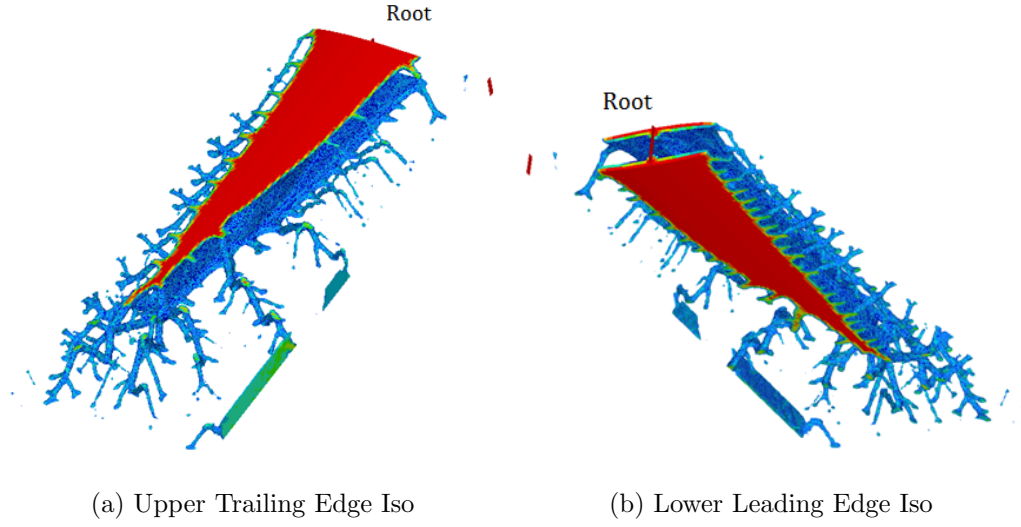


**Figure 57. Various View Orientations for Global TO with Density Fraction Threshold of 0.20**

Figure 58 is the TO for the similar design space shown in Figure 33, with a rib



and rear spar used to support the skin. The rib was placed at the tip of the design space and a rear spar was used in order to retain the aerodynamic shape of the skin at those locations. Figure 59 is the various orientations for the TO results at a density fraction threshold of 0.20.

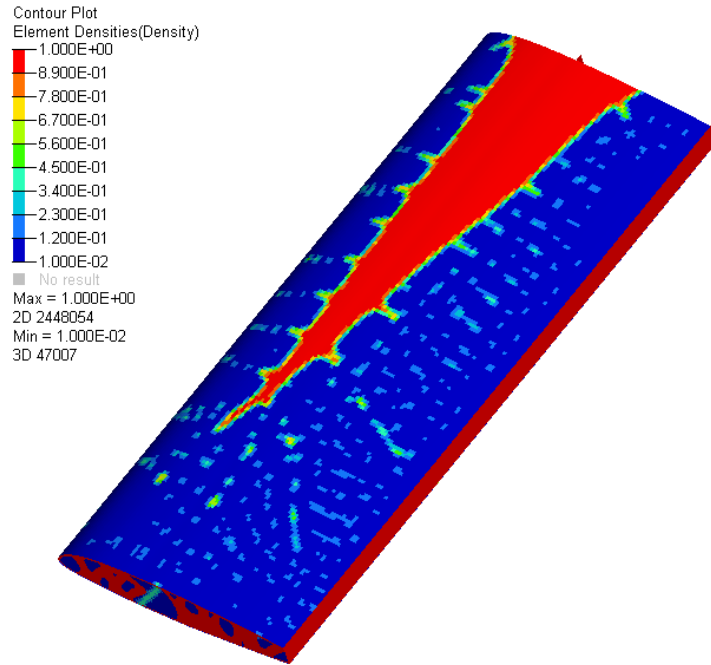
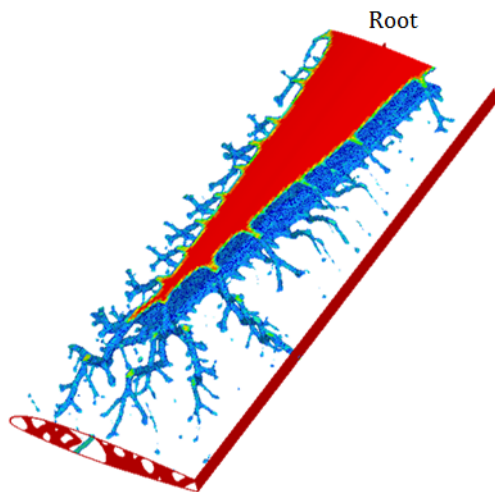
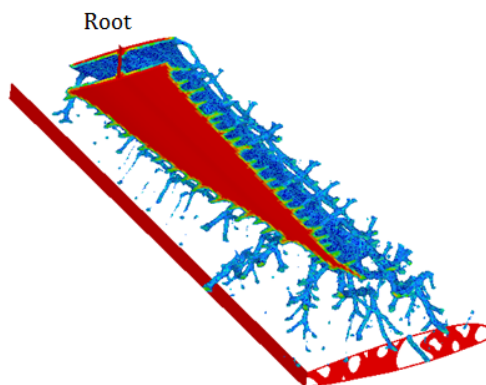


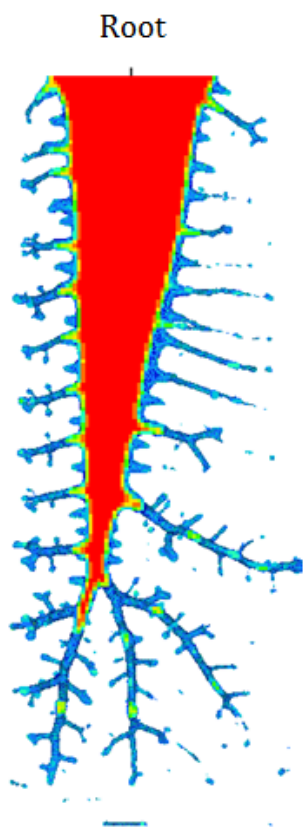
Figure 58. Density Fraction Contour of Global Wing TO with Tip Ribs and Rear Spar



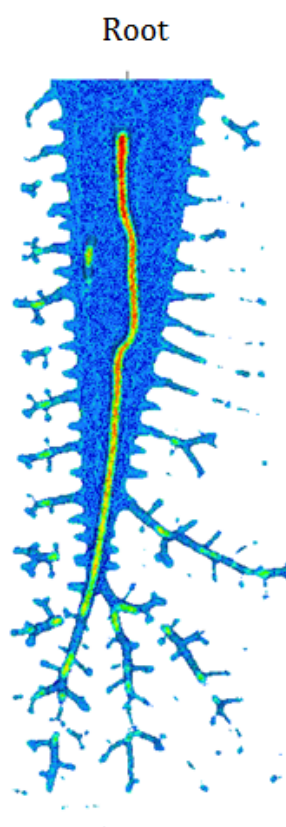
(a) Upper Trailing Edge Iso



(b) Lower Leading Edge Iso



(c) Top



(d) Top, Sliced

**Figure 59. Various View Orientations for Global TO with Density Fraction Threshold of 0.20**

Neither one of these designs is able to meet the material volume measurements of the baseline wing. The material required to create the members seen to support the wing is relatively significant when compared to extremely thin ribs. Intuitively, the amount of material required to fabricate a single beam is relatively large when compared to baseline wing. However, a different problem setup may produce better results. The mesh size was selected as a computing power constraint. A finer mesh would most likely produce more detailed results. With the current analysis, the course mesh creates large support members rather than thinner rib-like structures. A properly setup optimization would also disregard volumes for the design space which were found to provide minimal support. This process is highly iterative and requires significant engineering judgment. Performing this method is suggested for future research. Another consideration is mesh size. A finer mesh is desired for higher quality results and is also recommended for future research. However, reducing the mesh size results in an exponential increase in runtime.

#### **4.4 Component Integration**

Another advantage to AM is the ability to integrate various components which selected as the most prevalent independent structure in the wing. The tank location and shape was interpreted from the high material volume regions, resulting from high density fractions, found in the global 3D optimizations. This was done to allow the tank to act as a structural component rather than an independent entity. This process was accomplished for both a local 2D and global 3D TO. The loading resulting from fuel was disregarded in this research. Tank walls maintained the material thickness associated with the wing spars and baseline fuel tank. The material which encloses the fuel tank on the top and bottom is the exterior wing skin. This is the same methodology used for the baseline wing.

#### 4.4.1 Local Tank Integration.

For simplicity, the tank for the local design is relatively basic. The shape retains the same volume as the baseline tank shown in Figure 27. The new design, seen in Figure 60, has mostly straight faces for easy adaptation to design space ribs.

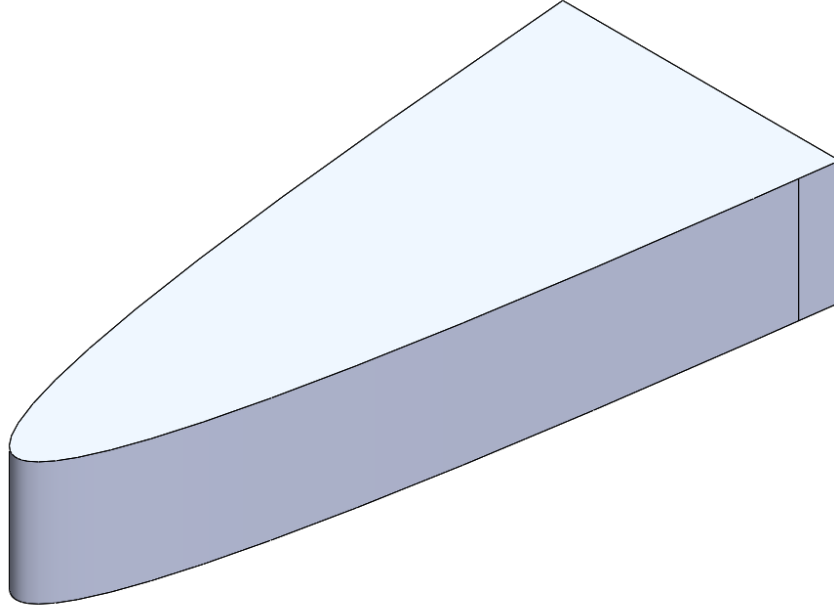


**Figure 60. Fuel Tank Design for Local TO**

As discussed above, the component design was inspired by the structurally vital shape of the global optimization. Figure 61 illustrates this methodology. On the left-hand side is the density contour created from a global TO. This image was overlaid with the local design space wing seen in Figure 31. The high density fraction area, shown in red, is crucial to structural integrity. The Optistruct TO design is shown in Figure 62. Lateral placement of the design space ribs is consistent with all previous local designs. The holes in the main spar were removed since a significant portion of the original design was replaced by the tank. A sizing optimization on the spar, discussed previously, did reduce the mass on the spar.

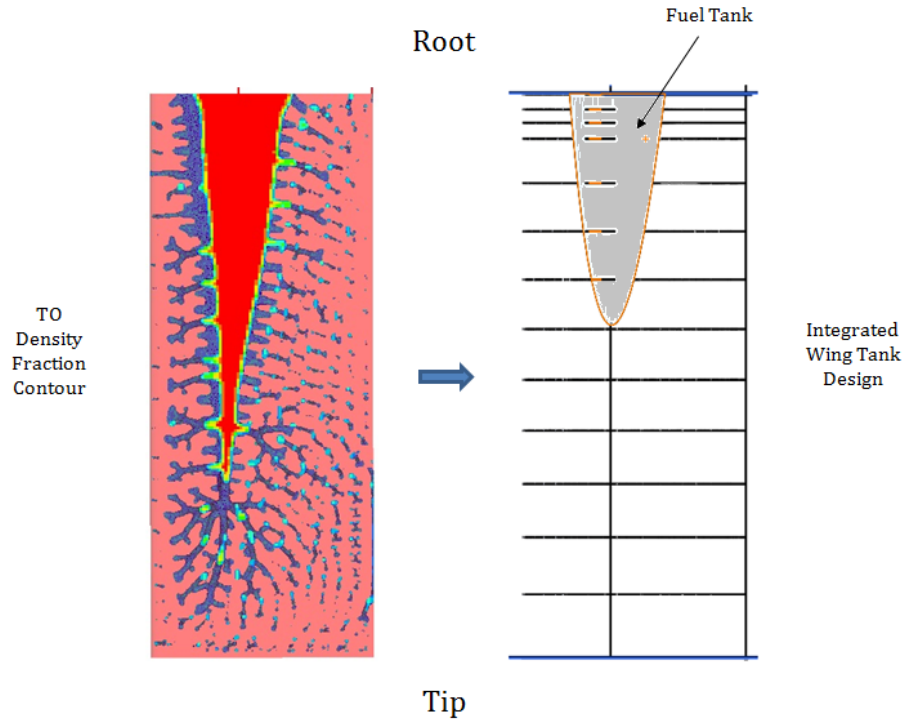


Figure 61. Global Stress Contour Interpretation to Local TO Fuel Tank Design

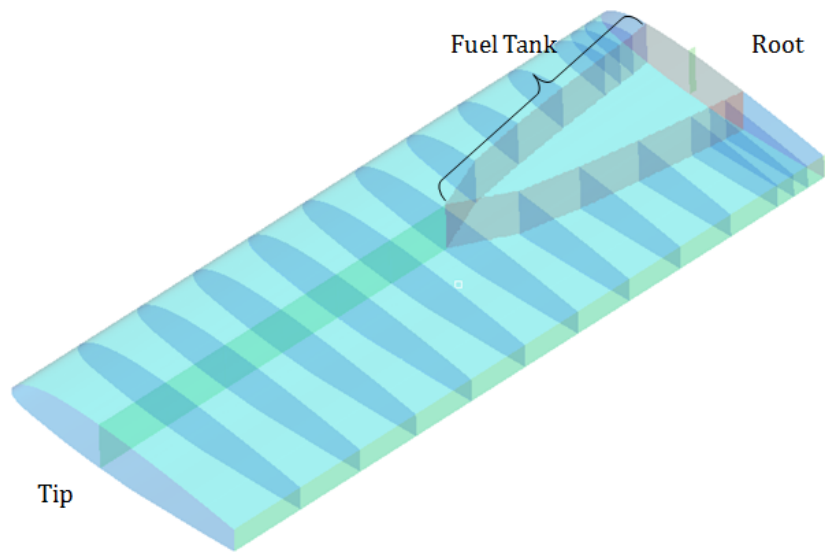
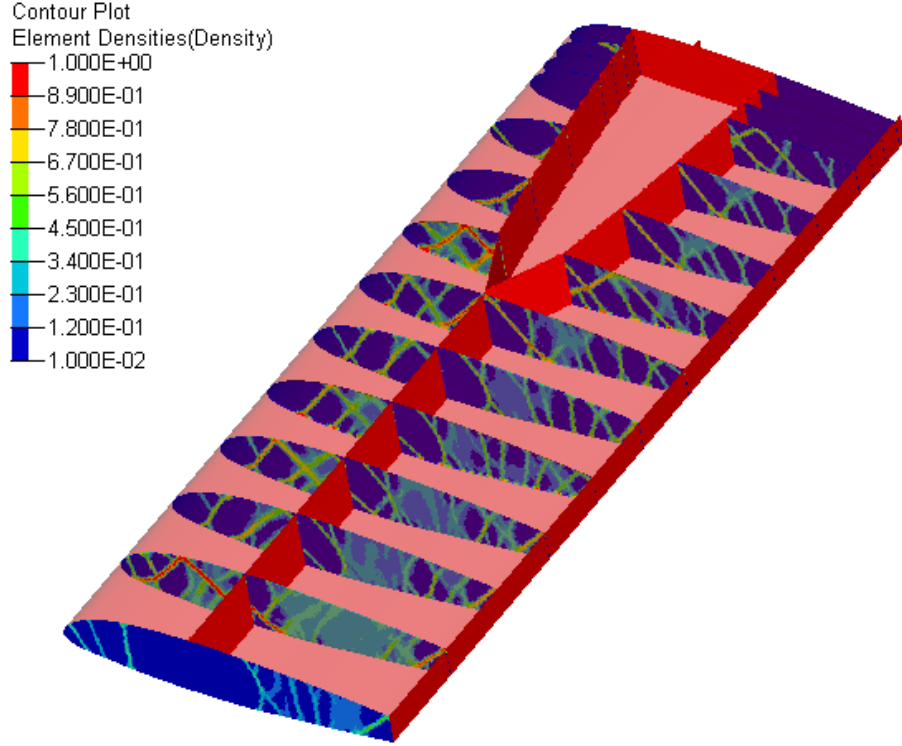


Figure 62. Optistruct Local TO Tank Integration Model Problem Setup for Rib Design

The optimization was performed with a VF constraint of 0.15 with an objective of minimizing weighted compliance, similar to previous optimizations. This was a two-

step process. The first step involved a rib-only optimization without manipulation of the skin or spars. The second step utilized the initial TO results and applied a sizing spar and skin optimization. The results for the rib-only tank design are seen in Figure 63.



**Figure 63. Results for Fuel Tank TO with Rib Only Design Space**

In this case, a density fraction threshold of 0.10 was used. The post-processed analysis of this design provided generally good results comparable or better than the baseline wing with a fuel tank. However, extremely high stress concentrations formed at the joint between the fuel tank and the main spar. This is commonly seen in FEA with 2D shell elements. The singular point where the faces join artificially generates a very high stress region. This is avoided in part design through the use of fillets, not applicable to 2D analysis [41]. In order to reduce the high levels of peak stress found at the joints, a sizing and skin optimization was performed.

#### 4.4.1.1 Sizing Optimization and Analysis.

The optimized design was reevaluated with skin and spar optimization. Doing so alleviated most of the high-stress areas in the structure. This optimization, seen in Figure 64, utilized the same design practices discussed in Section 4.2.3. The spar and skin optimization using the TO ribs is shown in Figure 64. Figure 64a is the tank optimized skin and Figure 64b is the same model with the skin removed, making the TO spars visible. A summary of the component mass and volumes are covered in Table 23. Similar to the local optimizations conducted without the tank, the baseline mass values for the baseline wing the fuel tank are also listed in the table.

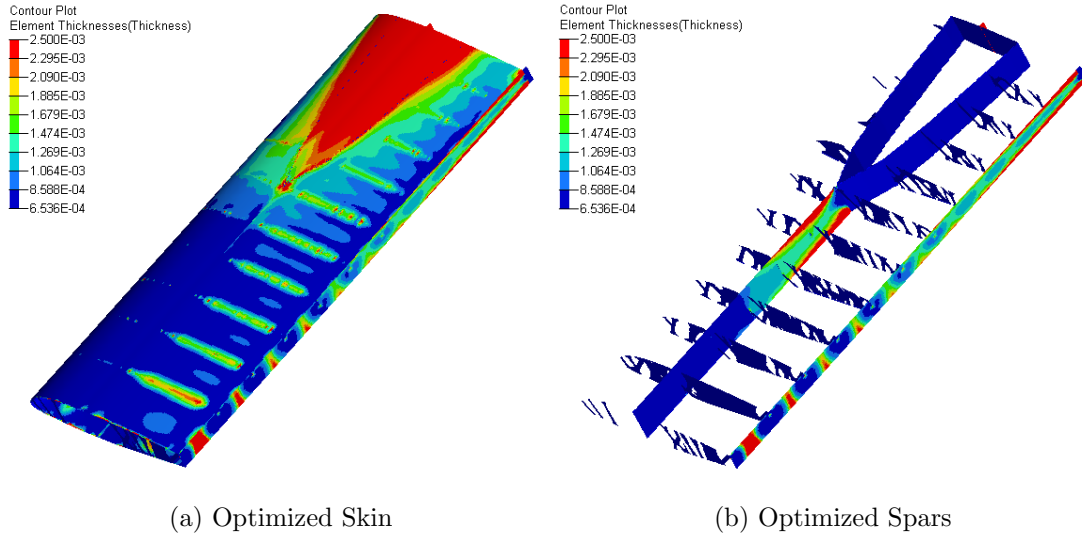


**Figure 64. Local TO Results for Spar and Skin Free-Sizing Optimization of Local Wing Design with Integrated Tank**

**Table 23. Rib, Spar, and Skin TO with Integrated Fuel Tank Component Surface Area, Volume, and Mass Compared to Baseline Wing**

	Total Rib	Spars	Fuel Tank	Skin	Total
Surf Area ( $m^2$ )	0.812	0.616	0.543	6.479	8.45
Volume ( $m^3$ )	$0.66 \times 10^{-3}$	$0.63 \times 10^{-3}$	$0.55 \times 10^{-3}$	$5.23 \times 10^{-3}$	$7.10 \times 10^{-3}$
Mass ( $kg$ )	1.835	1.740	1.534	14.640	19.479
<i>Baseline Wing with Tank Mass (<math>kg</math>)</i>	<i>3.482</i>	<i>2.236</i>	<i>1.565</i>	<i>14.539</i>	<i>21.822</i>
<i>Savings From Baseline (%)</i>	<i>47.4 %</i>	<i>22.1 %</i>	<i>1.9 %</i>	<i>-0.1%</i>	<i>10.8%</i>

Even after the sizing optimization on the skin and spar was completed, peak stress on each model remained at the connection between the spar and the fuel tank. An example of this is seen in Figure 65 for the +6g, roll right maneuver. However, the maximum von-Mises stress remained below the failure limit of the baseline fuel tank wing analyzed in Section 3.7.3. Once again, it is also possible to reduce this high stress region through fillets in a manufactured model.

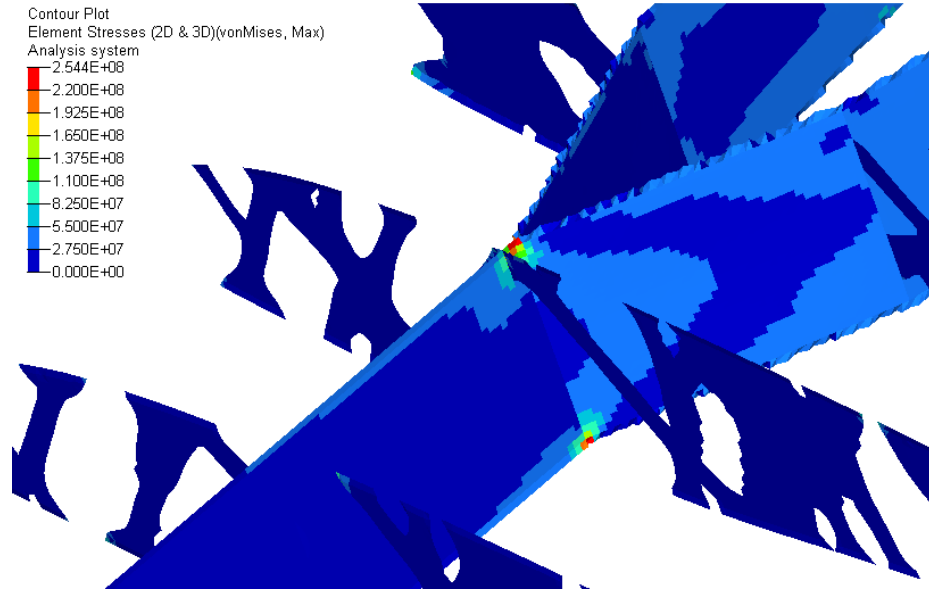


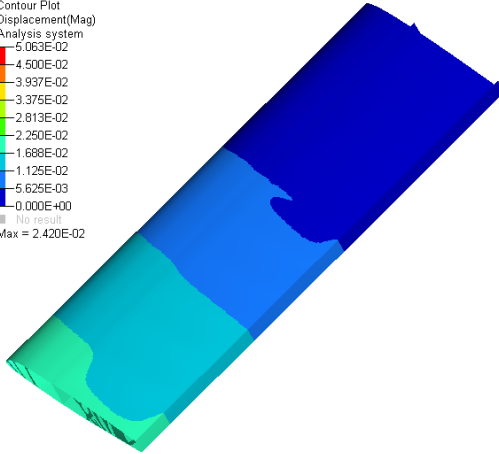
**Figure 65. High Stress Region at Joint Between Spar and Fuel Tank in Integrated Fuel Tank Local TO**

The displacement and stress results for this optimization show significant improve-

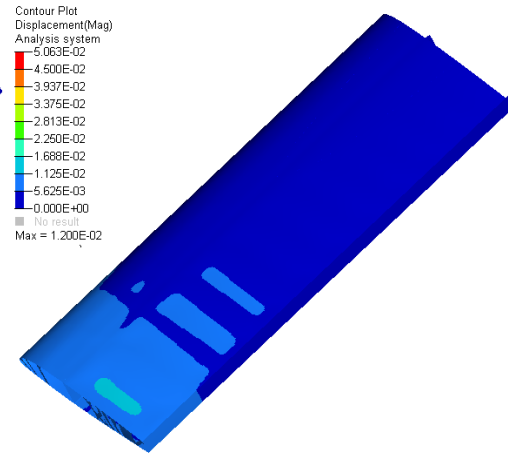


ment over the baseline wing with the fuel tank. Skin deflection between the ribs was also significantly reduced. Figures 66 and 67 are the deflection and stress contours, respectively. The peak stress remained approximately the same as the baseline wing. However, it was constrained to the joint between the spar and tank. From the stress contour, it is apparent the stress is much more evenly distributed throughout the skin. If the joining location between the spar and the tank is disregarded, maximum von-Mises stress is  $154.1 \text{ MPa}$ . This is 39.4 percent less than the baseline wing with fuel tank.

Contour Plot  
Displacement(Mag)  
Analysis system  
5.063E-02  
4.500E-02  
3.937E-02  
3.375E-02  
2.813E-02  
2.250E-02  
1.688E-02  
1.125E-02  
5.625E-03  
0.000E+00  
No result  
Max = 2.420E-02

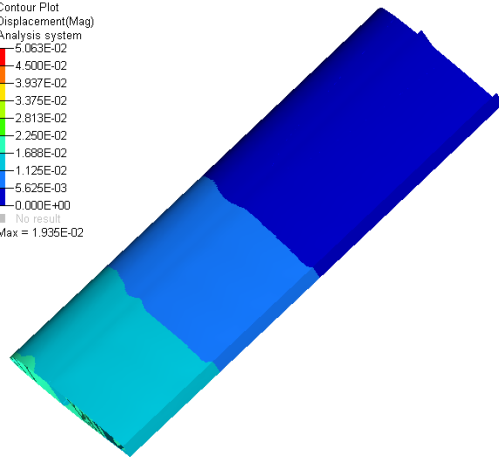


(a) +6g Deflection Contour



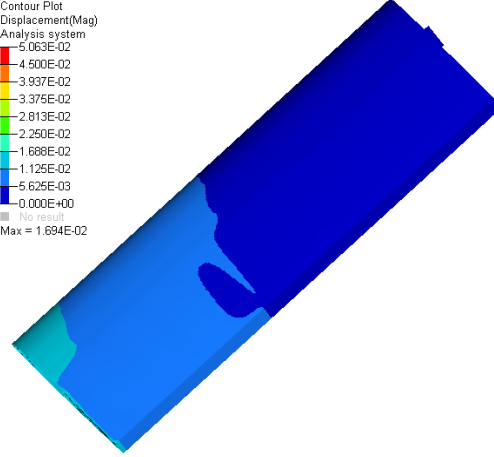
(b) -3g Deflection Contour

Contour Plot  
Displacement(Mag)  
Analysis system  
5.063E-02  
4.500E-02  
3.937E-02  
3.375E-02  
2.813E-02  
2.250E-02  
1.688E-02  
1.125E-02  
5.625E-03  
0.000E+00  
No result  
Max = 1.935E-02



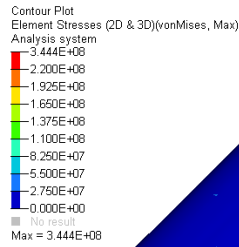
(c) +6g, Roll Right Deflection Contour

Contour Plot  
Displacement(Mag)  
Analysis system  
5.063E-02  
4.500E-02  
3.937E-02  
3.375E-02  
2.813E-02  
2.250E-02  
1.688E-02  
1.125E-02  
5.625E-03  
0.000E+00  
No result  
Max = 1.694E-02

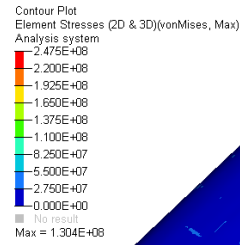


(d) +6g, Roll Left Deflection Contour

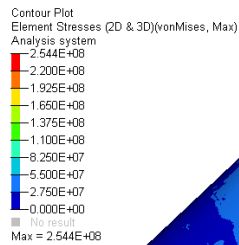
**Figure 66. Free Sizing Optimization Wing Deflection Contours for Each Flight Profile of Wing Integrated with Fuel Tank**



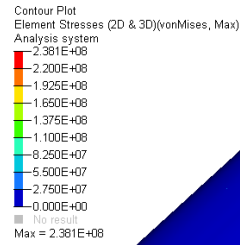
(a) +6g Stress Contour



(b) -3g Stress Contour



(c) +6g, Roll Right Stress Contour



(d) +6g, Roll Left Stress Contour

**Figure 67. Free Sizing Optimization Wing Stress Contours for Each Flight Profile of Wing Integrated with Fuel Tank**

**Table 24. Displacement and Stress of Free Sizing Optimized Wing with Integrated Fuel Tank Compared to Baseline Wing**

Condition	Total Displacement	von-Mises Stress
FS Optimization of Wing with Fuel Tank		
+6g	0.0169 m (0.67 in)	217.2 MPa (-1.9%)
-3g	0.0120 m (0.47 in)	130.4 MPa (0%)
+6g, Roll Right	0.0194 m (0.76 in)	254.4 MPa (0%)
+6g, Roll Left	0.0169 m (0.67 in)	145.5 MPa (-11.5%)
<i>Baseline Wing with Fuel Tank Analysis</i>		
<i>+6g</i>	<i>0.0416 m (1.64 in)</i>	<i>221.4 MPa</i>
<i>-3g</i>	<i>0.0201 m (0.79 in)</i>	<i>130.6 MPa</i>
<i>+6g, Roll Right</i>	<i>0.0487 m (1.92 in)</i>	<i>254.5 MPa</i>
<i>+6g, Roll Left</i>	<i>0.0306 m (1.20 in)</i>	<i>164.4 MPa</i>

Similar to the previous discussion on spar and skin sizing optimizations, overall stress and displacement decreased considerably. This is an important consideration for AM type designs. The strongest region of the components are now located where the greatest loads are. Conversely, low loading areas require much less material volume. This process shows drastic improvement in structural strength without compromising mass.

#### 4.4.1.2 Buckling Analysis.

Buckling for the wing with the spar and skin sizing optimization results mimicked the spar and skin optimization discussed in Section 4.2.3. A summary of the BLF for the various flight profiles of the integrated fuel tank wing with TO ribs and sizing optimized spars and skin is shown in Table 25. Baseline values are included as well for reference.

**Table 25. Buckling Load Factor of Integrated Fuel Tank Wing with TO Ribs and Sizing Optimized Spars and Skin Compared to Baseline Wing**

	Buckling Load Factor			<i>Baseline Values</i>		
Condition	Mode 1	Mode 2	Mode 3	<i>Mode 1</i>	<i>Mode 2</i>	<i>Mode 3</i>
+6g	0.302	0.349	0.370	<i>0.094</i>	<i>0.102</i>	<i>0.111</i>
-3g	0.317	0.366	0.430	<i>0.109</i>	<i>0.134</i>	<i>0.157</i>
+6g, Roll Right	0.290	0.306	0.315	<i>0.079</i>	<i>0.086</i>	<i>0.093</i>
+6g, Roll Left	0.277	0.356	0.403	<i>0.142</i>	<i>0.153</i>	<i>0.167</i>

Similar to previous sizing optimizations, the BLF values for a design with a sizing optimization were approximately three times those of the baseline wing and buckling is more evenly distributed laterally. This is because the skin and spar is thicker near the root and can therefore limit overall displacement by stiffening high stress regions. The skin and spars are thinner near the tip since there is less crucial loading away from the wing root. Overall for a wing built through AM, a sizing optimization is very advantageous in regards to buckling performance.

#### 4.4.1.3 AM of Design Models.

In addition to the AM sizing restrictions discussed in Section 2.8, the designs were limited by other factors. DMLS designs cannot create overhangs of more than 45 degrees without building support structures. The material thickness is also an important consideration. Even though build layers are as low as 16-microns, any thickness less than approximately 1 mm is unlikely to support any weight. Therefore, any designs which were sized down to meet restrictions on build volume were reevaluated to ensure manufacturing capability.

This wing design was manufactured in both plastic and aluminum via AM. For both materials, the design was resized significantly to remain within size limits of

the AM equipment. The wing was redesigned to a 1/12 scale. Consequentially, the component thickness also needed scaling in order to avoid structural failure during the build. Most components are on the order of 1 mm thick in the scaled down version, approximately 10 to 12 times the size of a true scaled version. Figure 68 is the plastic print of the model with the top half of the skin removed. An aluminum model of the same design was also manufactured through DMLS and is shown in Figure 69

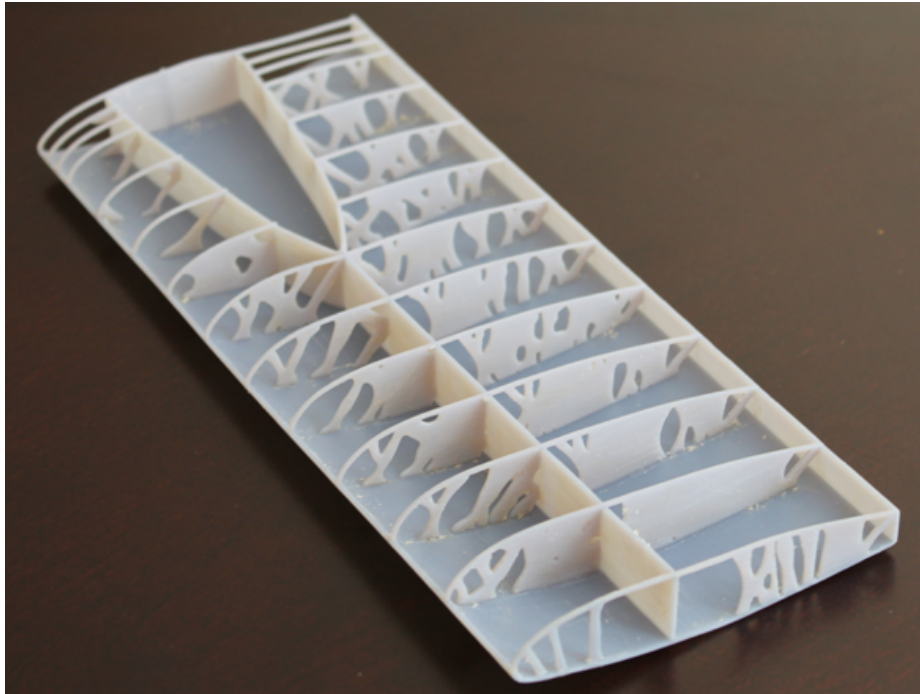


**Figure 68. Plastic 3D Printed Model of Local TO Integrated With Fuel Tank with Top Skin Removed**



**Figure 69. Aluminum AM Model of Local TO Integrated With Fuel Tank with Top Skin Removed**

#### **4.4.1.4 Dual Purpose Structure Conclusion.**

The use of a dual purpose structure for the fuel tank showed a 10.1 percent reduction in overall mass of the wing while improving displacement and stress characteristics. The amount of savings is rather significant considering the rib only TO showed a savings of 3.7 percent. This shows the benefit of implementing multiple structures into a single component. However, the sizing optimization was required to reduce high stress regions at the joints. Through AM, this is not a problem. Additionally, further analysis to ensure ample structural integrity within the fuel tank is required. Regardless, this process is very enlightening regarding the capabilities of dual purpose structures, combined with TO and sizing optimizations.

#### 4.4.2 Global Tank Integration.

A fuel tank for the global model was also applied for TO. In this case, the fuel tank was once again shaped to retain the volume of the baseline tank. However, this design mimics the high density fraction regions from the global design more closely; the tank is slightly I-beam shaped. This tank is shown in Figure 70. This was done to enhance the load bearing capability of the fuel tank compared to the simpler design discussed in the previous section.

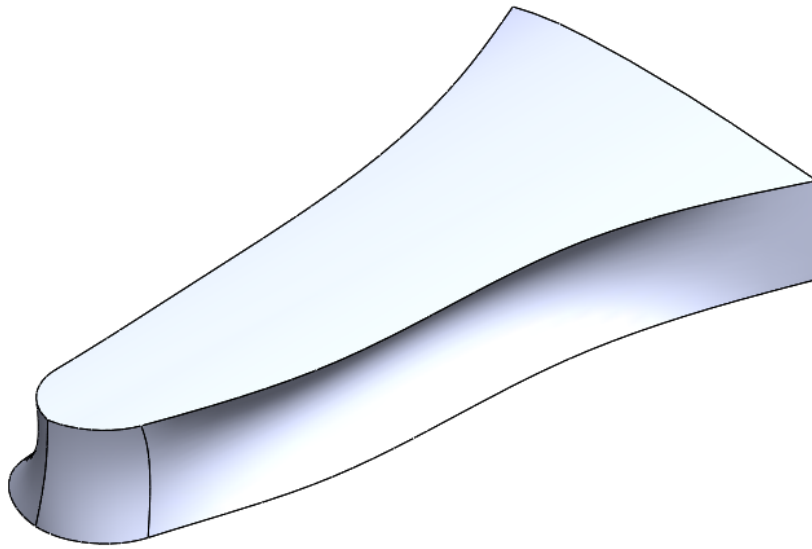


**Figure 70. Fuel Tank Design for Global TO**

VF for these models was once again set at 0.10, similar to previous global TO, with an objective of minimizing weighted compliance. In this case, a tip rib and rear spar were used to maintain the aerodynamic shape of the wing. To determine the shape of the rib at the tip of the wing, an optimization was conducted with both a 3D solid design space and a 2D shell design space for the rib. The rib design was then reinserted back into the model and the 3D TO was completed again. The original rear spar thickness was retained throughout this process. This is graphically represented in Figure 71. The skin was removed in this illustration for simplicity. This process



was also used for the lattice TO discussed in the following section. A density fraction threshold of 0.20 was used for the results in Figure 72. Similar to the global design without a fuel tank, the TO generated an I-beam like shape along the edges of the tank.

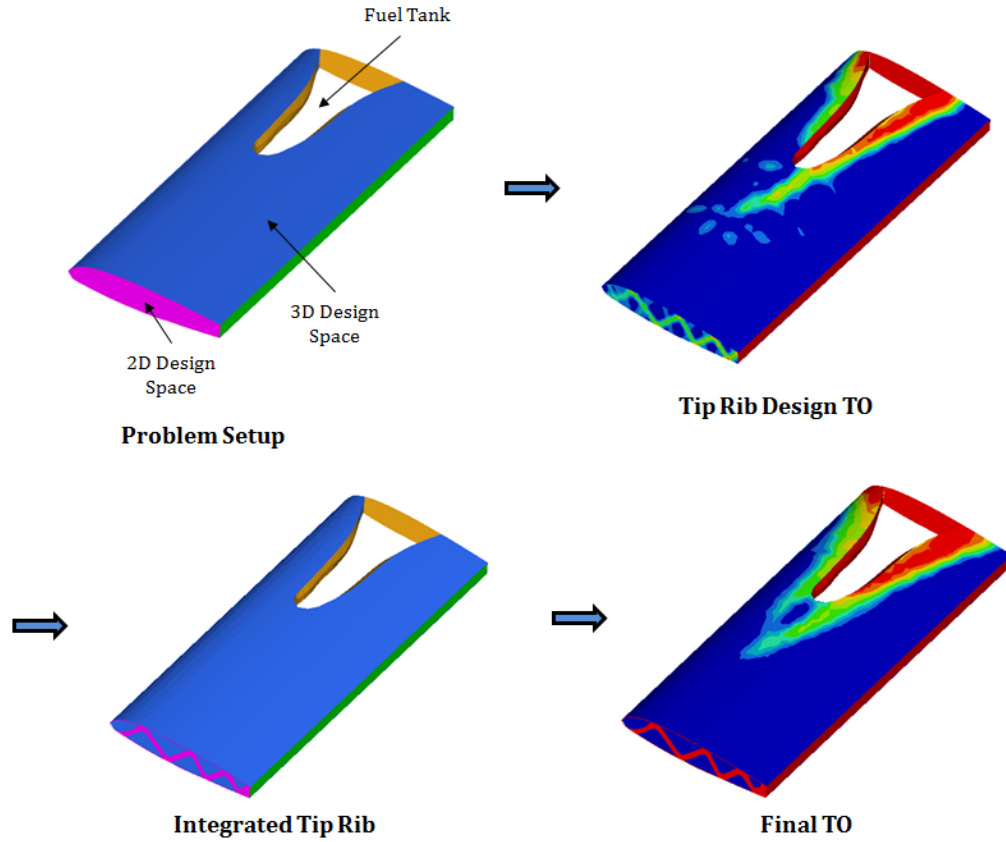
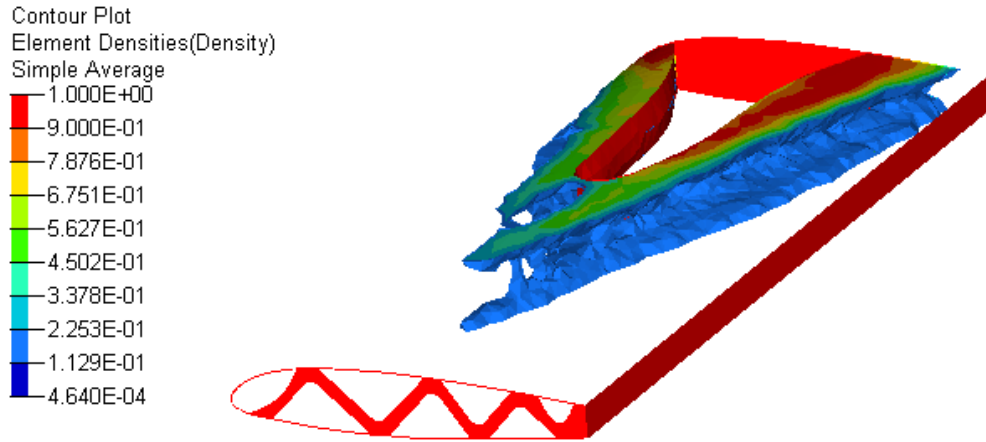


Figure 71. Global Design with Integrated Fuel Tank Process to Determine Tip Rib Design and Generate TO



**Figure 72. Global Design with Integrated Fuel Tank TO Results with 0.20 Density Fraction Threshold**

Once again, FEA results for the global TO were not available. However, an FEA was conducted on the lattice structures examined in Section 4.5. Lattice structures provided generally better results than the traditional means of setting a density fraction threshold. Therefore, a greater emphasis was placed towards this design.

## 4.5 Lattice Structures

Finally, lattice structures were considered as a means to physically interpret variable density structures. This was accomplished for the integrated fuel tank design discussed in Section 4.4. All of the lattice structures used in this research were automatically generated and sized within the Optistruct software. Since this is a relatively new capability, manufacture of these parts was not possible at the time of this research. However, a stress and displacement analysis was conducted.

The lattice TO process in Optistruct is essentially a three step procedure. The problem setup is the same as with any traditional 3D optimization. However, a density fraction range to generate lattice is selected. The initial TO generates the standard TO output file for variable density, while Optistruct generates an additional solver

file which replaces the variable density elements with lattice structure. The lattice structure size is determined based on the density fraction of each element. In other words, a 50 percent dense element will have a lattice structure of 50 percent material. During the second step, the solver file performs a sizing optimization on the lattice structure elements with an objective to minimize volume with a constraint of maximum stress. The sizing optimization design variable is the lattice member diameter. For the purpose of this research, the stress levels were constrained to the baseline analysis maximum stress at each loadstep. This ensures the wing performance is not significantly worse than the baseline in regards to maximum von-Mises stress. This process outputs another solver file with the size optimized lattice structures. Finally, an FEA is completed on the lattice structure by running this file. This process is graphically interpreted in Figure 73.

#### **STEP 1**

Build Design Space  
Input Desired Density Fraction for Lattice Generation  
Constraint: Volume Fraction  
Objective: Min Compliance

Output: 1) Variable Density TO  
2) Design Space Lattice Structure



#### **STEP 2**

Set Stress Constraints  
Perform Sizing Optimization  
Constraint: Stress and Volume Fraction  
Objective: Min Volume Fraction

Output: Size Optimized Lattice Structure



#### **STEP 3**

Run FEA

Output: Stress and Displacement Analysis

**Figure 73. Optistruct Process for Lattice Optimization of 3D Design Space**

An example of the lattice structures was built in the same design space as the global designs previously discussed. The wing with a tip rib and rear spar was used. In this case, a very course mesh was implemented to allow for the construction of the lattice and for the resizing required to manufacture a scaled model. Additionally, the VF was decreased to 0.05. This was reasonable since, with lattice structures, there is no interpretation of variable density elements and therefore no large solid members to support the structure. Rather, almost the entire internal volume of the wing consists of lattice structures. Figure 74 is the generated lattice structure with both a full view and zoomed in view for inspection of the design. The colors in the images show independent lattice members, not any deviation in design.

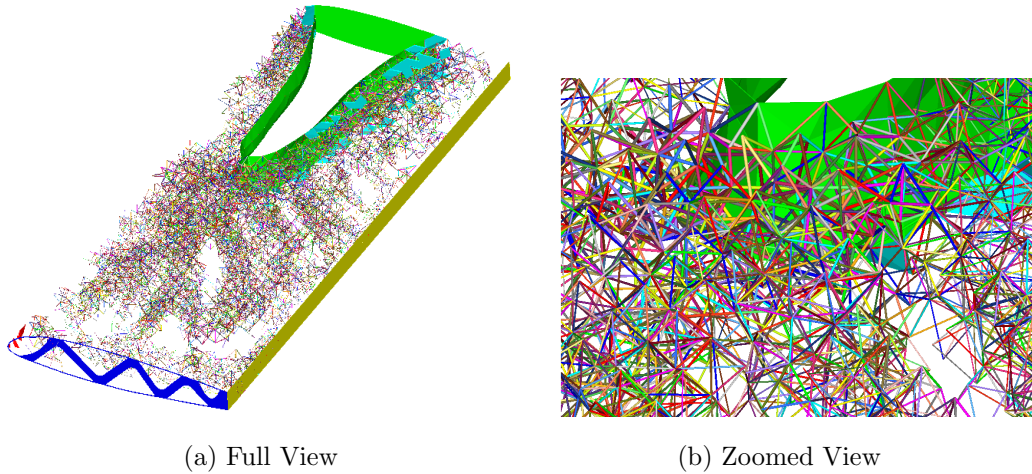


**Figure 74. Lattice Structure for Global Design Space with Integrated Fuel Tank at VF of 0.05**

A stress and displacement analysis was accomplished on the lattice structure. For all flight profiles, the peak von-Mises stress decreased compared to the baseline wing with the fuel tank. The most significant reduction was 11.5 percent. Overall displacement values are low in comparison and in-line with displacement from the spar and skin optimizations. These values are summarized in Table 26. BLF results for this design are shown in Table 27.

**Table 26. Displacement and Stress of Lattice Structure for Global Design Space with Integrated Fuel Tank Compared to Baseline Wing with Fuel Tank Compared to Baseline Wing**

Condition	Total Displacement	von-Mises Stress
Global Lattice Structure		
+6g	0.0230 m (0.91 in)	217.2 MPa (-1.9%)
-3g	0.0157 m (0.62 in)	130.4 MPa (-0.1%)
+6g, Roll Right	0.0271 m (1.07 in)	254.4 MPa (0%)
+6g, Roll Left	0.0155 m (0.61 in)	145.5 MPa (-11.5%)
<i>Baseline Wing with Fuel Tank Analysis</i>		
<i>+6g</i>	<i>0.0416 m (1.64 in)</i>	<i>221.4 MPa</i>
<i>-3g</i>	<i>0.0201 m (0.79 in)</i>	<i>130.6 MPa</i>
<i>+6g, Roll Right</i>	<i>0.0487 m (1.92 in)</i>	<i>254.5 MPa</i>
<i>+6g, Roll Left</i>	<i>0.0306 m (1.20 in)</i>	<i>164.4 MPa</i>

**Table 27. Buckling Load Factor of Lattice Structure for Global Design Space with Integrated Fuel Tank**

	Buckling Load Factor			<i>Baseline Values</i>		
Condition	Mode 1	Mode 2	Mode 3	<i>Mode 1</i>	<i>Mode 2</i>	<i>Mode 3</i>
+6g	0.224	0.246	0.253	<i>0.094</i>	<i>0.102</i>	<i>0.111</i>
-3g	0.216	0.223	0.225	<i>0.109</i>	<i>0.134</i>	<i>0.157</i>
+6g, Roll Right	0.193	0.210	0.217	<i>0.079</i>	<i>0.086</i>	<i>0.093</i>
+6g, Roll Left	0.221	0.240	0.273	<i>0.142</i>	<i>0.153</i>	<i>0.167</i>

Total maximum displacement for the lattice structure wing decreased significantly in most cases. This is likely a result of a relatively continuous support structure throughout the wing, much different than the rib design with large gaps between spars. This is possibly the case for the overall stiffer internal construction leading to

the decreased values. Maximum von-Mises stress values remain very similar to those of the baseline wing, with improvements of up to 11.5 percent. Buckling also showed significant improvement compared to the baseline wing with fuel tank. BLF values for this design were generally twice those of the baseline. This analysis shows the lattice design at least performs as well or better than the baseline structure.

However, the overall mass of this structure is 27.910 *kg*, noticeably heavier than any of the other optimizations. This is nearly a 28 percent increase over the baseline design with a fuel tank. This is likely at least partially attributed to the VF selected. A lower volume fraction, which is limited by the Optistruct solver, would obviously reduce mass. Another consideration is the range of density fraction in which to use lattice. Even though extremely low density elements do not add much mass, they are not necessarily required to provide sufficient support. As lattice capabilities within Optistruct improve, further research towards reducing mass should take place. Overall, stress levels for the lattice structure were no worse than the baseline design. Further examination into the lattice may reduce these levels even further. This, along with the much lower peak displacement, hints at a drastically improved 3D design using lattice structures for future work.

## 4.6 Summary

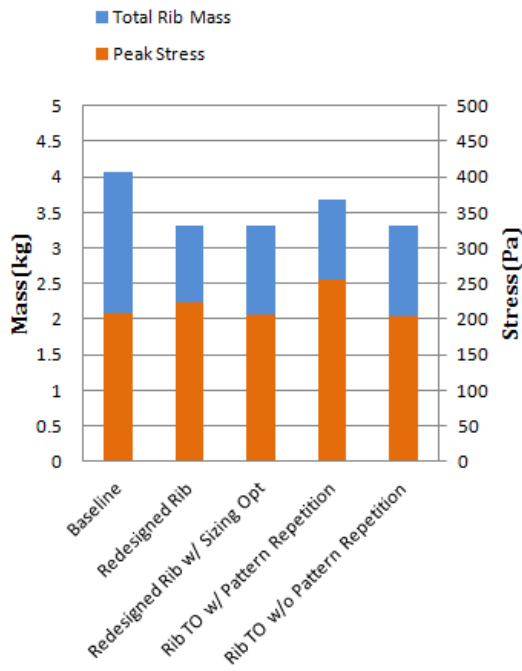
Table 28 is a performance summary of the optimized wings designed in this research. For simplicity, a summary of all the wing designs is shown in Appendix B with the associated titles. It is important to note the values from the table do not tell the whole story. An examination of each result illustrates a much better comparison. Even though wing designs may have a peak stress which is similar, the average von-Mises stress in the components is potentially much less. Displacement for rib optimizations, on the other hand, was relatively similar to the baseline for

most cases. However, the spar and skin optimizations significantly reduced this measurement. When considering mass savings for the rib-only optimizations, the mass does not appear to significantly reduce relative to the total mass of the wing. However, the individual structures which were optimized saw a significant mass reduction. Therefore, this study is regarded on a relative scale. Minor mass savings for the total wing is a result of convincing savings in the ribs.

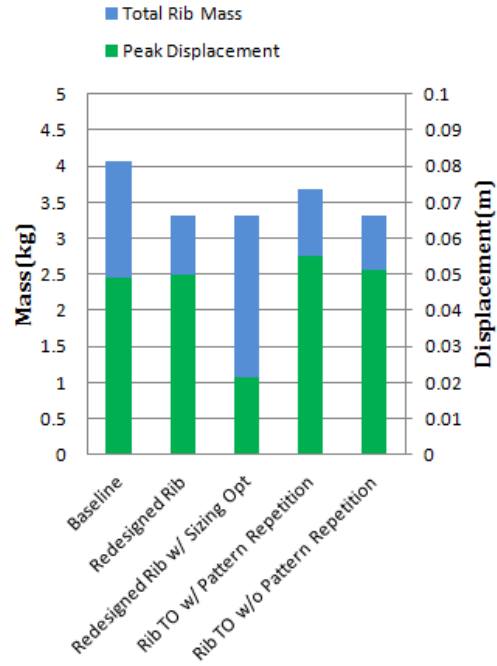
**Table 28. Performance Summary for all TO Results**

Design Iteration	Mass ( <i>kg</i> )	Peak Disp (m)	Peak Stress (Pa)	Min BLF (n=1)	Max BLF (n=1)
Baseline	20.831 (0%)	0.0492 (0%)	207.9 (0%)	0.081 (0%)	0.143 (0%)
Baseline w/ Tank	21.822 (0%)	0.0487 (0%)	254.5 (0%)	0.079 (0%)	0.142 (0%)
Rib TO w/o Pat Rep	20.076 (-3.7%)	0.0510 (+3.6%)	203.4 (-2.2%)	0.079 (-2.5%)	0.141 (-1.4%)
Rib TO w/ Pat Rep	20.446 (-1.9%)	0.0549 (+11.6%)	255.7 (+23.0%)	0.082 (+1.2%)	0.155 (+8.4%)
Redesigned Rib	20.548 (-1.4%)	0.0499 (+1.4%)	222.9 (+7.2%)	0.073 (-9.9%)	0.134 (-6.3%)
Reint. Rib w/ Sizing Opt	20.078 (-3.7%)	0.0214 (-56.5%)	207.1 (-0.4%)	0.207 (+155.6%)	0.271 (+89.5%)
Local Tank w/ Sizing Opt	19.479 (-10.8%)	0.0194 (-60.0%)	254.4 (0%)	0.277 (+250.6%)	0.317 (+122.7%)
Lattice Design	27.910 (+27.8%)	0.0271 (-44.4%)	254.4 (0%)	0.193 (+144.3%)	0.224 (+57.7%)

These results are more clearly displayed in Figure 75. In this chart, the various designs are directly compared to the baseline wing for mass, stress, and displacement. The rib TO without pattern repetition was the lightest and had the lowest stress level. The wing with the spar and skin optimization had the lowest displacement.



(a) Mass and Stress vs. Design



(b) Mass and Displacement vs. Design

**Figure 75. Mass with Stress and Displacement vs Design for TO Wings without Integrated Fuel Tank**

The same analysis was performed with the fuel tank designs. By implementing the fuel tank into the design, this method applied more emphasis on the necessity of AM. Figure 76 shows the mass, stress, and displacement for the baseline and optimized designs with a fuel tank. In this case, ribs were not necessarily used. Therefore, the mass of the total design was used.



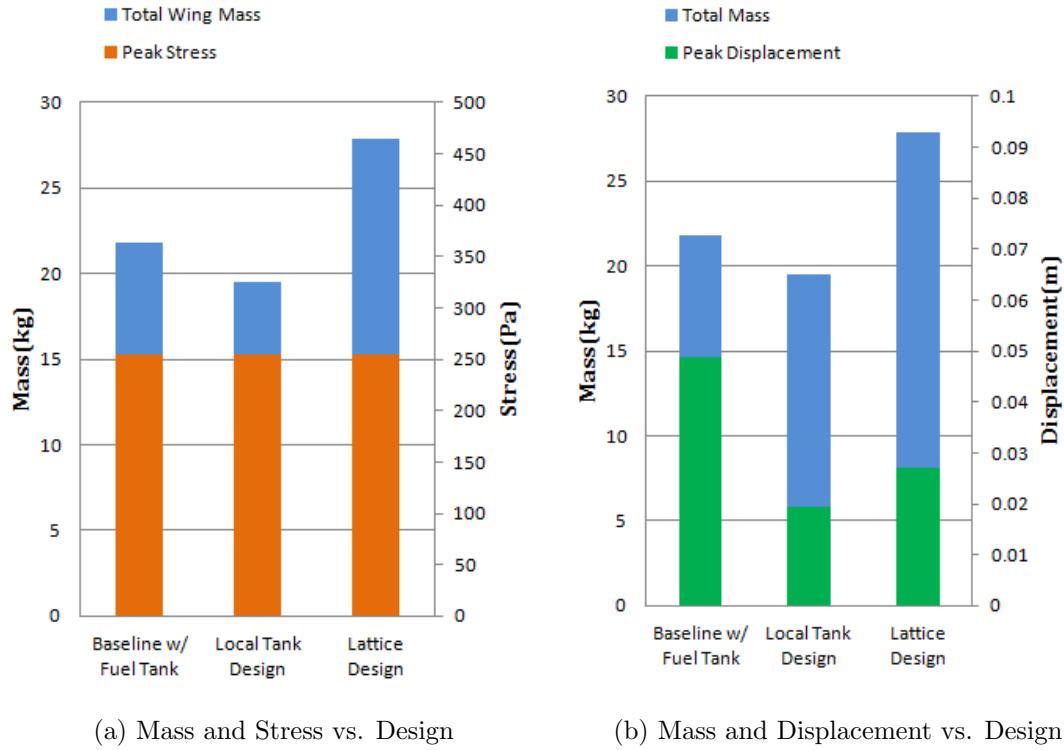


**Figure 76. Mass with Stress and Displacement vs Design for TO Wings with Integrated Fuel Tank**

Figure 75 and Figure 76 show of some the advantages experienced with the optimization process. For 2D designs, TO reduces the overall mass while at least reducing the displacement and stress of the component. The most noticeable improvement is seen when TO is combined with a sizing optimization. The thicker regions of material compensated for high load regions whereas less material was required for low load regions. Overall, this procedure improved on current wing design, but is still somewhat limited by manufacturing constraints with modern day practices. The most improvement was seen with a TO and sizing optimization on the local design with the integrated fuel tank. Using the walls of the fuel tank as a dual purpose structure provided a relatively significant reduction in mass. This along with the sizing optimization reduced high stress regions found along sharp connections in the wing. Once again, these optimizations resulted in a design which improved structural performance

while simultaneously reducing mass. Even though the overall weight savings may be minimal regarding the overall structure, they are a resultant of drastic improvement on a smaller scale. This process shows these advancements are simply applied by using this methodology.

## V. Conclusions and Recommendations

### 5.1 Review of Research Objectives

The overarching goal of this research was to optimize the entire structure of a wing which is manufacturable through AM. To fulfill this goal, the research was split into five objectives:

1. Determine pressure loading on the wing for critical phases of flight and apply the values towards the analysis and optimization processes.
2. Perform a computational analysis on the baseline aircraft wing to determine localized stress and displacement values.
3. Generate a computational analysis on the optimized designs used for comparative purposes.
4. Integrate a traditionally independent component into the optimized wing as a dual-purpose structure.
5. Interpret full-scale design to meet AM constraints and produce the model.

The first objective was met by applying a CFD analysis on the chosen wing. The wing was built with a generic fuselage to better simulate pressure losses laterally along the wing. Critical phases of flight were selected as those which met the load factor structural limitations of the aircraft. Additionally, full aileron deflection at maximum positive loading was used as a critical condition. These conditions were applied on a baseline wing model with and without a fuel tank, to satisfy the second objective. The wing model was build using 2D shell structures and disregarding components outside of spars, ribs, and skin. The third objective was met by analyzing the optimized designs under the same loading conditions. In general, the 2D optimizations were

post-processed to fully dense elements prior to FEA. The fourth objective was met by designing a similarly sized fuel tank compared to print the baseline model for both 2D and 3D optimizations. The tank shape and location was adapted from the highly dense regions found in a 3D TO. The final objective was met by sizing the wing design down to meet sizing limitations imposed by the AM equipment used. By doing so, the 2D shell elements became extremely thin. Therefore, they were appropriately scaled up to meet minimum printing constraints. Two aluminum models were built through the AM process, in addition to the polymer models manufactured locally.

The manufactured models primarily focused on the local design, which was essentially a variant of the baseline model. Since this was not possible for the lattice structure designed in this research, development of a metallic lattice global design was initiated through a partnership with Within Engineering headquartered in London, United Kingdom. Design and manufacture of these parts is currently ongoing and is a subject of future research.

## **5.2 Additive Manufacturing Design**

As discussed early in this research, AM with present day technologies does not allow for feasibly building a part as large as an aircraft wing. However, the capability may exist in the near future. If AM does become a method in which parts like this are built, it is vital to ensure the designs remain compliant with equipment barriers. For the models built here, the minimum sizing requirements inherent with the process limited how closely a scaled model was built to the actual design. Likewise, this prevented any quality wind-tunnel or structural testing outside of computational analysis. Another consideration which affect the design of AM parts is material overhang. A plastic 3D printer generally builds support material underneath any overhang. This is often difficult to remove in confined spaces. Likewise, a DMLS

machine, which does not have easily removable support material, can generally not have overhangs greater than 45 degrees. Additionally, enclosed areas are vented to allow for removal of the metallic powder.

However, AM provides an unparalleled capability towards radical design shapes. Even when considering the basic rib optimizations discussed in Section 4.2.1, a pattern methodology is not necessary. The time and effort to build a part with AM is not constrained by repeatability. There is therefore no advantage to pattern repetition with AM. The disadvantages toward performance easily outweigh any benefits which are seen. In reality, the traditional design space shape adapted from the baseline model is poor for AM. Setting up the problem in this way is limiting the overall capabilities of AM and TO. Recommendations alleviating this are discussed in the following section.

### **5.3 Recommendations for Improvement**

The ability to perform an effective TO is highly dependent on the mesh size. For the 2D optimizations in this study, the mesh was selected on the basis of the largest mesh which would produce reasonable results; this was a relatively iterative process. However, the 3D optimizations require significantly more computational power and thus much more time per iteration. The mesh for the global optimizations was selected at 1.5 cm along the sides. Even with this large of a mesh, TO times took on the order of 36 hours to complete. Shrinking down the mesh smaller would cause run times to increase exponentially. As discussed above, using the baseline design as a design space for the optimizations was not ideal. Since the ribs are very thin, a proper mesh for comparison would need sizing relative to the thickness. For future analysis, once the problem is properly setup, it is recommended to reduce mesh size and allow for extended computation time or use a more powerful computer.

Another consideration for further research is in how the loads were applied. For this research, only the static pressure loading was considered. This disregards forces generated on connections from the control surfaces or fuselage. Once a complete TO process is structured, additional loading will help strengthen the quality of results. Additionally, dynamic loading is a concern, but modeling is difficult. The fluid pressure on the walls of the fuel tank could create different results. Implementing this loading condition will determine the ability of the structure to support the fuel, and an optimization may then reduce the structural mass.

## 5.4 Future Work

Even though not addressed in this work, a spacing optimization was attempted on the local rib design. However, all efforts were unsuccessful. The current RV-4 baseline design, as well as most aircraft, relies on heuristics and tedious testing to establish the number of ribs and their respective locations. Doing this process mathematically has the potential to significantly streamline the aircraft design process.

Similarly, an extremely fine mesh size would generate the “true” optimized locations for any support structures in a 3D space. If the perpendicular ribs were the ideal design, a mesh equivalent to the rib width would generate a TO similar to the rib shape. Intuitively, this is not the case. How fine of a mesh which is analyzed in a reasonable amount of time is restricted by computational power. As the computational capability increases, the mesh size for analysis should decrease.

The real future of TO with AM lies with lattice structures. A lattice is one of the most directly manufacturable interpretations of variable density elements. Unfortunately, software limitations prevented further research in this realm. Future aircraft wing body TO research should definitely considering lattice structures.

A final consideration for future work is with the objectives and constraints used in

this research. A constrained volume fraction with an objective to minimize compliance was used almost exclusively. This is often the case with other TO research. However, doing so does not consider every failure mode or objective in designing a wing. Ideally, the objective is to minimize mass while constraining to failure modes, such as buckling or stress. However, attempts to change the objective did not provide feasible results. Therefore, further study into how objectives and constraints are applied are important for future analysis.

Regardless, the optimizations focusing on minimizing compliance accomplished in this research did provide improved designs. In every case, the TO created a better performing structure under the given constraints. As discussed previously, aircraft wings are historically “optimized” through heuristics and tedious testing. A TO process, however, can significantly formalize this method. A good problem setup with well-defined loading conditions will make the process much simpler, especially for radical aerodynamic shapes. This process is significantly more streamlined than historical methods. Combining the capabilities of AM as an enabler for TO drastically reduces several historical constraints, further enhancing potential. Expanding on the methodology developed in this research allows for significant improvement in current aircraft structural design.





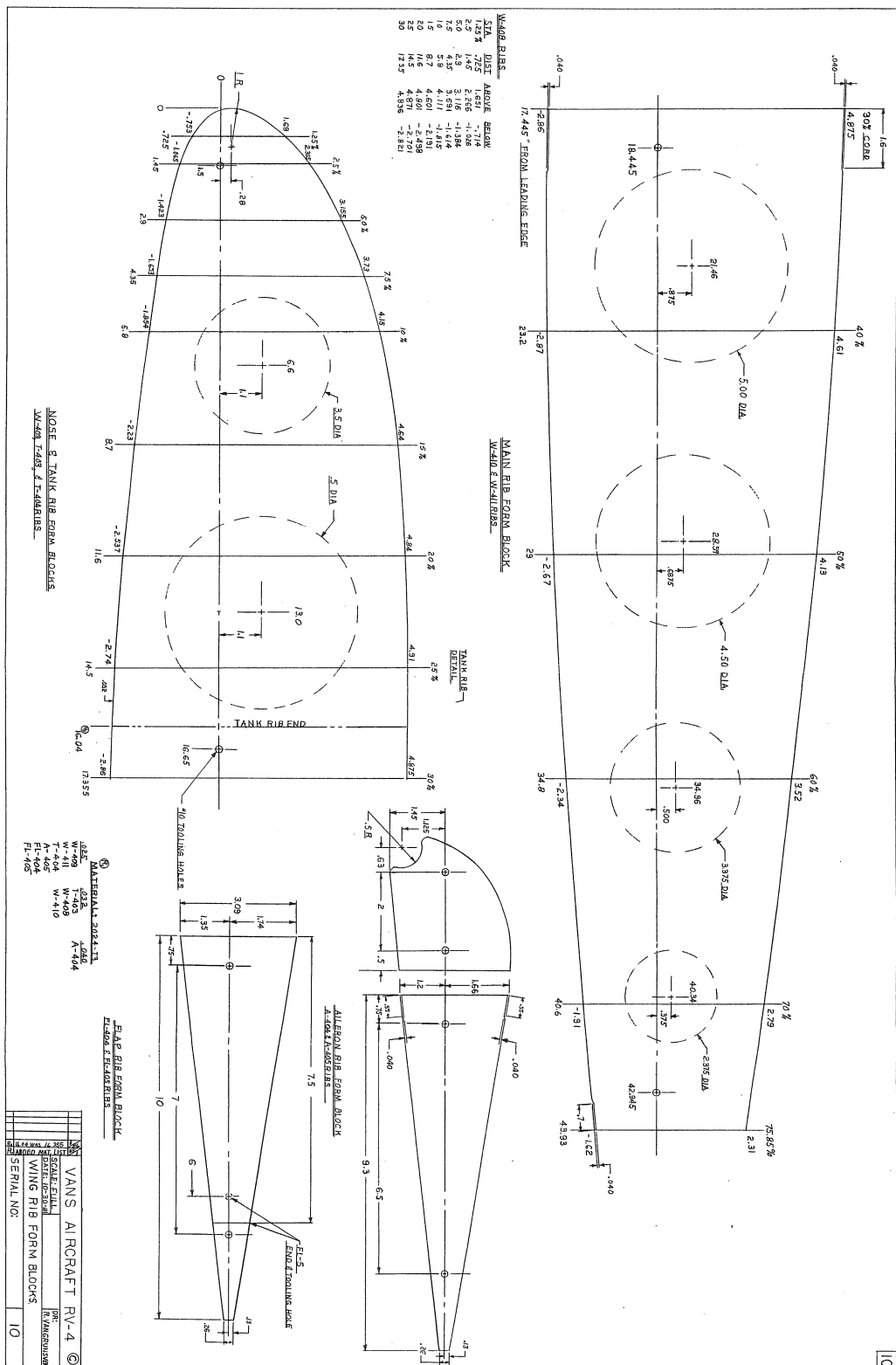
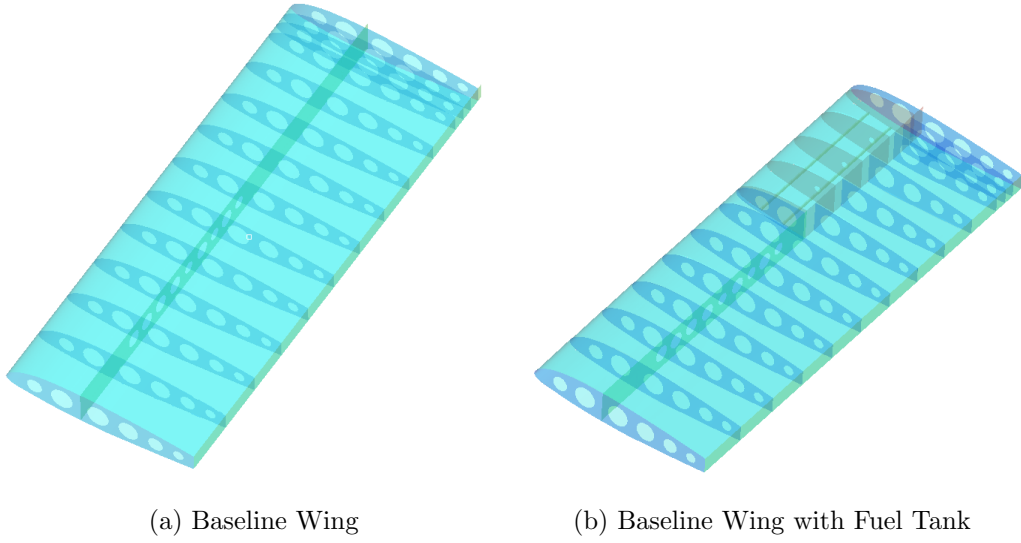


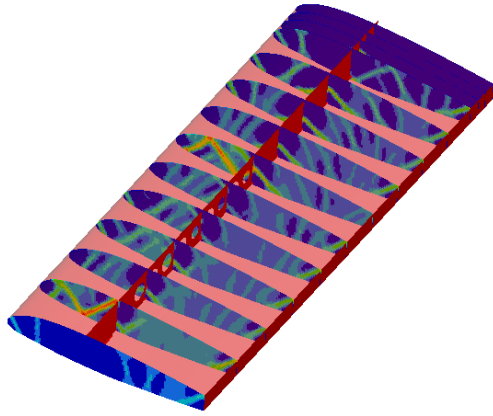
Figure 78. Van's RV-4 Rib Schematic [5]



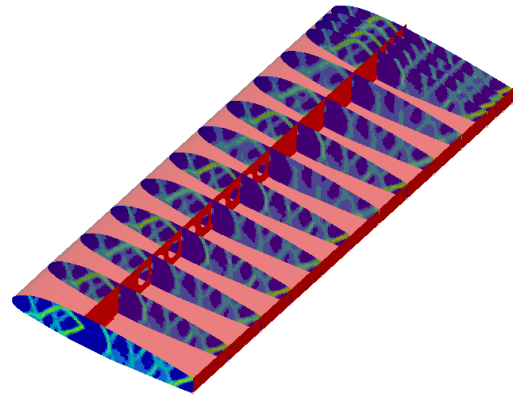
## B. Summary of Optimized Designs



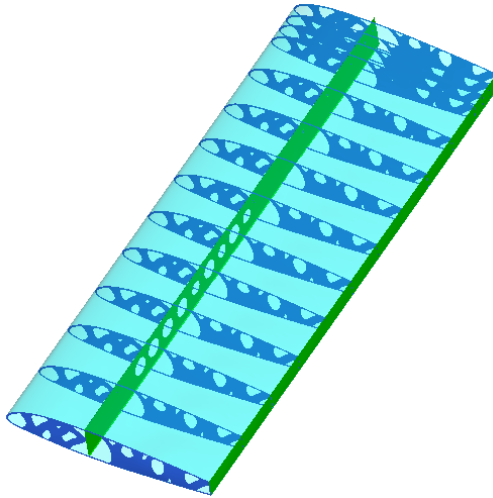
**Figure 80. Baseline Analysis Models**



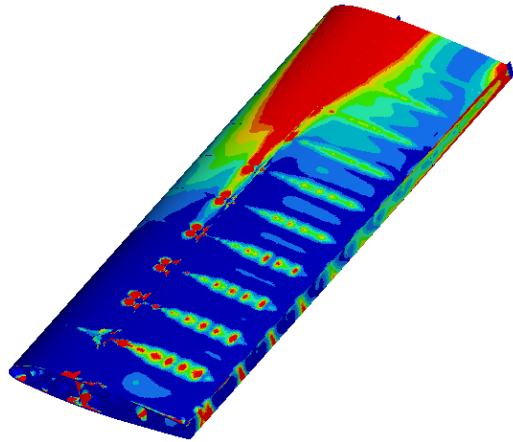
(a) Rib TO w/o Pattern Rep



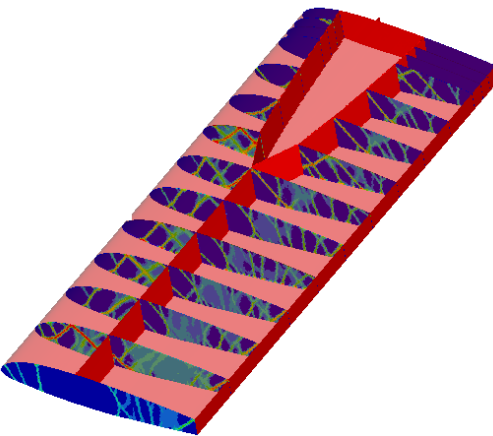
(b) Rib TO w/ Pattern Rep



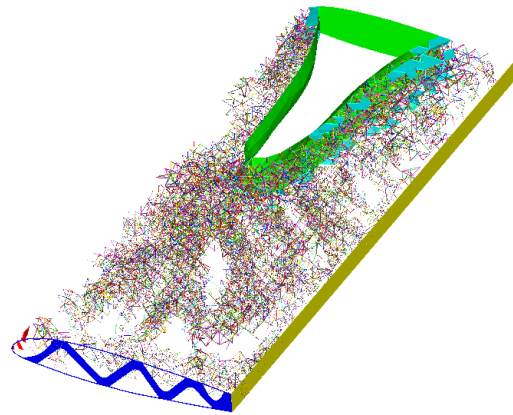
(c) Redesigned Rib



(d) Reint. Rib w/ Sizing Opt



(e) Local Tank w/ Sizing Opt



(f) Lattice Design

**Figure 81. Various TO Design Results**

## Bibliography

1. M. P. Bendsoe and O. Sigmund, *Topology optimization: theory, methods and applications*. Springer Science & Business Media, 2003.
2. O. Sigmund, “A 99 line topology optimization code written in matlab,” *Structural and Multidisciplinary Optimization*, vol. 21, pp. 120 – 127, October 2001.
3. L. Krog, A. Tucker, and G. Rollema, “Application of topology, sizing and shape optimization methods to optimal design of aircraft components,” in *Proc. 3rd Altair UK HyperWorks Users Conference*, 2002.
4. Locatelli, S. B. Mulani, and R. K. Kapania, “Wing-box weight optimization using curvilinear spars and ribs (sparibs),” *Journal of Aircraft*, vol. 48, pp. 1671–1684, September-October 2011.
5. Van’s Aircraft Inc., 14401 Keil Road NE, Aurora, OR 97002, *Van’s RV-4 Preview Plans*. Request to use all figures was approved.
6. B. Bourdin, “Filters in topology optimization,” *International Journal for Numerical Methods in Engineering*, no. 50, pp. 2143–2158, 2001.
7. O. Sigmund, “Design of multiphysics actuators using topology optimization—part i: One-material structures,” *Computer methods in applied mechanics and engineering*, vol. 190, no. 49, pp. 6577–6604, 2001.
8. M. P. Bendsøe and O. Sigmund, “Material interpolation schemes in topology optimization,” *Archive of applied mechanics*, vol. 69, no. 9-10, pp. 635–654, 1999.
9. Altair Engineering Inc., 1820 E. Big Beaver Rd, Troy, MI 48083, *Optistruct 12.0 User’s Guide*, 2013.

10. T. Megson and H. Gordon, *Aircraft structures for engineering students*. Elsevier, 2012.
11. J. Michalos and E. N. Wilson, *Structural mechanics and analysis*. Macmillan, 1965.
12. A. Chowdhry, “Altair’s software enhances the design of transportation,” *Forbes Online*, 2013.
13. Altair Engineering Inc., 1820 E. Big Beaver Rd, Troy, MI 48083, *Hypermesh 12.0 User’s Guide*, 2013.
14. Z. Luo, J. Yang, and L. Chen, “A new procedure for aerodynamic missile designs using topological optimization approach of continuum structures,” *Aerospace Science and Technology*, no. 10, pp. 364–373, 2006.
15. D. P. Raymer, *Aircraft Design: A Conceptual Approach*. 1801 Alexander Bell Drive, Reston, VA 20191: American Institute of Aeronautics and Astronautics, 2012.
16. J. D. Anderson, *Fundamentals of aerodynamics, 2005*. McGraw Hill International, Boston, MA, 2005.
17. T. R. Yechout, *Introduction to Aircraft Flight Mechanics*. 1801 Alexander Bell Drive, Reston, VA 20191: American Institute of Aeronautics and Astronautics, 2003.
18. Altair Engineering Inc., 1820 E. Big Beaver Rd, Troy, MI 48083, *Virtual Wind Tunnel 2.0 help*, 2013.
19. Altair Engineering Inc., 1820 E. Big Beaver Rd, Troy, MI 48083, *AcuSolve Programs Reference Manual*, 2013.

20. M. Ratzel and T. Ludescher, “Streamlining aerodynamic cfd analyses,” in *NAFEMS World Congress*, 2013.
21. S. Grihon, L. Krog, A. Tucker, and K. Hertel, “A380 weight savings using numerical structural optimization,” in *20th AAAF colloquium on material for aerospace applications, Paris, France*, pp. 763–66, 2004.
22. L. Krog, A. Tucker, M. Kemp, and R. Boyd, “Topology optimization of aircraft wing box ribs,” in *10th AIAA/ISSMO multidisciplinary analysis and optimization conference*, pp. 1–11, 2004.
23. G. Schuhmacher, M. Stettner, R. Zotemantel, O. OLeary, and M. Wagner, “Optimization assisted structural design of a new military transport aircraft,” *AIAA*, vol. 4641, no. 2004, p. E2, 2004.
24. Q. Liu, S. Mulani, and R. K. Kapania, “Global/local multidisciplinary design optimization of subsonic wing,” in *SciTech 2014*, 2014.
25. I. Gibson, D. W. Rosen, B. Stucker, *et al.*, *Additive manufacturing technologies*. Springer, 2010.
26. P. Kobryn, N. Ontko, L. Perkins, and J. Tiley, “Additive manufacturing of aerospace alloys for aircraft structures,” tech. rep., DTIC Document, 2006.
27. B. Lyons, “Additive manufacturing in aerospace: Examples and research outlook,” *The Bridge*, vol. 44, no. 3, 2014.
28. H. Lipson, “Frontiers in additive manufacturing: The shape of things to come,” *The Bridge*, vol. 44, no. 3, 2014.

29. D. Brackett, I. Ashcroft, and R. Hague, “Topology optimization for additive manufacturing,” in *22nd Annual international solid freeform fabrication symposium*, pp. 348–362, 2011.
30. H. Richards and D. Liu, “Topology optimization of additively-manufactured, lattice-reinforced penetrative warheads,” in *56th AIAA/ASCE/AHS/ASC Structures, Structural Dynamics, and Materials Conference*, 2015.
31. “Objet eden500v specification sheet,” tech. rep., Stratasys Ltd., 7665 Commerce Way, Eden Prairie, MN 55344, 2014.
32. Objet Geometries Ltd., *Objet Eden User Guide*, 2008.
33. K. Rekedal, “Investigation of the high-cycle fatigue life of selective laser melted and hot isostatically pressed ti-6al-4v,” Master’s thesis, Air Force Institute of Technology, 2950 Hobson Way, Wright-Patterson Air Force Base, OH 45433, March 2015.
34. E. O. S. GmbH, *EOSINT M280 Specifications Sheet*. The organization, Robert-Stirling-ring 1, 82152 Krailling/Munich, Germany.
35. Van’s Aircraft Inc., *RV-4 Performance Specifications*, accessed March 3, 2015.
36. Extra Aircraft Production and Sales, 46569 Hunxe, Federal Republic of Germany, *Extra-200 Information Manual*.
37. MatWeb, “Aluminum 2024-t4; 2024-t351,” 2015.
38. M. Drela, *Xfoil Subsonic Airfoil Development System*, 2007.
39. D. Walker, D. Liu, and A. Jennings, “Topology optimization of an aircraft wing,” in *56th AIAA/ASCE/AHS/ASC Structures, Structural Dynamics, and Materials Conference*, 2015.



40. E. N. Jacobs, I. H. Abbott, and M. Davidson, "Preliminary low-drag-airfoil and flap data from tests at large reynolds numbers and low turbulence, and supplement," *NACA ACR, March*, 1942.
41. *Practical Aspects of Finite Element Simulation: A Study Guide*. Troy, MI: Altair Engineering Inc., 2014. Altair University.

<b>REPORT DOCUMENTATION PAGE</b>					<i>Form Approved</i> <b>OMB No. 0704-0188</b>	
The public reporting burden for this collection of information is estimated to average 1 hour per response, including the time for reviewing instructions, searching existing data sources, gathering and maintaining the data needed, and completing and reviewing the collection of information. Send comments regarding this burden estimate or any other aspect of this collection of information, including suggestions for reducing this burden to Department of Defense, Washington Headquarters Services, Directorate for Information Operations and Reports (0704-0188), 1215 Jefferson Davis Highway, Suite 1204, Arlington, VA 22202-4302. Respondents should be aware that notwithstanding any other provision of law, no person shall be subject to any penalty for failing to comply with a collection of information if it does not display a currently valid OMB control number. <b>PLEASE DO NOT RETURN YOUR FORM TO THE ABOVE ADDRESS.</b>						
<b>1. REPORT DATE (DD-MM-YYYY)</b> 06-18-2015		<b>2. REPORT TYPE</b> Master's Thesis			<b>3. DATES COVERED (From — To)</b> October 2013 — June 2015	
<b>4. TITLE AND SUBTITLE</b>  Topology Optimization of an Aircraft Wing				<b>5a. CONTRACT NUMBER</b>		
				<b>5b. GRANT NUMBER</b>		
				<b>5c. PROGRAM ELEMENT NUMBER</b>		
<b>6. AUTHOR(S)</b>  Walker, David L., Captain, USAF				<b>5d. PROJECT NUMBER</b>		
				<b>5e. TASK NUMBER</b>		
				<b>5f. WORK UNIT NUMBER</b>		
<b>7. PERFORMING ORGANIZATION NAME(S) AND ADDRESS(ES)</b> Air Force Institute of Technology Graduate School of Engineering and Management (AFIT/EN) 2950 Hobson Way WPAFB OH 45433-7765					<b>8. PERFORMING ORGANIZATION REPORT NUMBER</b>  AFIT-ENY-MS-15-J-044	
<b>9. SPONSORING / MONITORING AGENCY NAME(S) AND ADDRESS(ES)</b> Joint Aircraft Survivability Program Office Mr. Dennis Lindell Civ 795 S Courthouse Road Suite 1100 Arlington, VA 22204-2489 dennis.lindell@navy.mil					<b>10. SPONSOR/MONITOR'S ACRONYM(S)</b>  JASP	
					<b>11. SPONSOR/MONITOR'S REPORT NUMBER(S)</b>	
<b>12. DISTRIBUTION / AVAILABILITY STATEMENT</b>  DISTRIBUTION STATEMENT A: APPROVED FOR PUBLIC RELEASE; DISTRIBUTION UNLIMITED.						
<b>13. SUPPLEMENTARY NOTES</b>  This material is declared a work of the U.S. Government and is not subject to copyright protection in the United States.						
<b>14. ABSTRACT</b>  A Topology Optimization (TO) was conducted on an aircraft wing in order to mathematically determine an ideal structural case for future aircraft. TO generally involves iteratively reducing individual elemental density until the desired mass or volume constraint is met. Two different TO styles were approached: a global three-dimensional concept and a more traditional two-dimensional rib and spar optimization which more closely mimics the baseline model. All optimizations were compared against a baseline wing for von-Mises stress, displacement, and buckling. The objective of this research was to develop a design procedure maintaining the baseline structural integrity of the wing while reducing weight. As with many TO designs, Additive Manufacturing (AM) was studied as a means to produce the wing concerning both the feasibility of manufacture and as a logistical advantage compared to traditional means. Additionally, a fuel tank was integrated into the wing structure as a proof-of-concept for the potential benefits of AM. Finally, a 3D lattice structure was utilized as a conceptual method for improving current design methodology.						
<b>15. SUBJECT TERMS</b>  topology optimization, finite element analysis, optimization, survivability						
<b>16. SECURITY CLASSIFICATION OF:</b>			<b>17. LIMITATION OF ABSTRACT</b>	<b>18. NUMBER OF PAGES</b>	<b>19a. NAME OF RESPONSIBLE PERSON</b>	
<b>a. REPORT</b>	<b>b. ABSTRACT</b>	<b>c. THIS PAGE</b>			Dr. David Liu, AFIT/ENY	
U	U	U	UU	148	<b>19b. TELEPHONE NUMBER (include area code)</b> (937) 255-3636, x4542; david.liu@afit.edu	